Royal Holloway, University of London
Department of Physics

Development of a Non-Invasive Transverse Beam Position Monitor using Incoherent Cherenkov Diffraction Radiation

---

Daniel M. Harryman

November, 2022

A thesis submitted in partial fulfilment for the degree of Doctor of Philosophy.

DECLARATION

I confirm that the work presented in this thesis is my own. Where information has been derived from others it has been clearly referenced.

Signed: ____

Date: ____

ACKNOWLEDGEMENTS

There are a large number of thanks and support I have to give for this thesis. Firstly I want to thank my academic supervisor Dr Pavel Karataev. Over the course of this PhD he has given support and advice that have undoubtedly contributed to the success of this project. Without his insightful analogies and descriptions I would still be trying to grasp some of the theoretical concepts explored in this thesis.

I owe my experimental supervisor Dr Lorraine Bobb a great deal of gratitude. Her guidance has given me the confidence and abilities to take responsibility and ownership of my own experiments. She has always offered astute advice and directed me to ask the right questions rather than giving me the answers. This project suffered setbacks due the failure of machine parts and a global pandemic. These setbacks were largely tempered by the fortitude and efforts of Dr Lorraine Bobb and for that I owe her my utmost thanks.

With regards to experimental operations I want to thank all of the staff at Diamond Light Source who have supported this project. This has comprised many staff members and teams ensuring that the beam was running and control systems were in place allowing me to perform my experiments.

I would also like to mention and thank the members of the Cherenkov Diffraction Radiation collaboration. The collaboration leader Dr Thibaut Lefevre, has an optimistic attitude towards research that is infectious. Other members of the collaboration include, but are not limited to: Dr Stefano Mazzoni, Dr Robert Kieffer, Dr Michele Bergamaschi, Dr Alexander Potylitsyn, Dr Kirill Fedorov, Kacper Lasocha, Andreas Schloegelhofer. I greatly enjoyed my trips to CERN to work with many of the collaboration members, I was always shown great hospitality and I hope I was able to contribute to the work carried out there. When mentioning collaboration members Dr Kirill Fedorov deserves a special mention for our in-depth discussions on equations, papers, and simulation codes.

For the staff and colleagues at Royal Holloway University of London, I would like the thank Dr Stephen Gibson for being my project advisor. I would also like to mention Siobhan Alden for being another John Adams Institute PhD student who was always ready to listen.

Importantly I want to acknowledge my colleagues from my previous employment at the ISIS Neutron Source. The role I had there was my first step into particle accelerators. The love for the subject that I picked up there is what led me to pursue a PhD in accelerator science. Undoubtedly the skills and experience I gained during that employment has contributed to the success of this project.

Recognising my parents, my mother has always been a pillar of support who has had confidence in my abilities even when I've doubted myself. My late father was the one who instilled in me a curiosity to learn and develop that I have been unable to fulfil outside of research. I hope the work I have done in this project has made them both proud.

Of course no acknowledgments would be remotely complete without mentioning my amazing wife Kayce, she has been through this PhD journey with me. She was able to lift up my spirits even during the lowest points of my PhD during a world pandemic. She has always helped me see the big picture and I love her for that.

OVERVIEW OF CONTRIBUTIONS

Over this thesis a large amount of work has been carried out where like any thesis there is a large amount of collaboration. This section is to highlight and explicitly state who has been responsible for each part of the project.

Chapter 1 is an introduction to the project. This is a literature review that describes the current state of the beam position monitor field and lists the motivation behind this project. As this chapter is a literature review there is minimal first hand research described in this chapter.

The next is Chap. 2, this is once again a literature review that details the Polarisation Currents Approach (PCA) model used for the theoretical simulations performed in this project. The understanding of this model that I have is largely due to Dr Pavel Karataev, but again as this chapter is a literature review there is minimal first hand research described in this chapter.

Chapter 3 details the experimental setup of the test stand at Diamond Light Source. With regards to experimental setup the Cherenkov Diffraction Radiation (ChDR) target was designed at CERN, when I started working on this project the accelerator components were installed, including the ChDR radiator, three Optical Transistion Radiation (OTR) screens, and the Inductive Beam Position Monitor (IBPM), but no optical or data acquisition systems were setup for these.

The optical system for the OTR monitors was designed by Dr Lorraine Bobb, though I assembled and characterised these optical systems myself. The ChDR optical systems described in Chap. 3 were designed by myself while checking the design and taking input from my supervisors and the ChDR collaboration.

Before each series of shifts there was often hardware that needed checking or changing. This included installing the data acquisition equipment for the IBPM, configuring and wiring in the triggers, or aligning the ChDR optical system. The majority of the work was done by myself, though support was provided from supervisors and Diamond infrastructure staff when needed. The software to communicate with the ProxiVision camera was provided by CERN, whereas the software later developed to acquire data from the PMT detector and the IBPM was developed by myself.

The commissioning of the experiment is described in Chap. 4. For the initial setup and commissioning shift Dr Lorraine Bobb supervised while I learnt how to run the experiment. After these first few shifts I took over as the primary experimentalist running the majority of the experiments by myself. Before each experimental shift an experimental plan was drawn up. This plan would then be shared with my supervisors and our collaboration before I would manage the experiment. Results from each shift would then be shared with the collaboration to best decide the direction for the next set of experiments.

Chapter 5 uses the model described in Chap. 2 to produce simulations. The simulation framework described in this chapter was developed and programmed by myself as were the results produced from this framework.

Chapter 6 describes the image processing techniques that were used in this thesis. This study was undertaken myself, as were the codes developed to perform the mathematical operations described.

Chapter 7 shows the results produced from the experiments performed for this thesis. These results are produced from data that I took with analysis codes I developed. The interpretation of the results has been conferred with my supervisors and the ChDR collaboration.

Finally Chap. 8 details the conclusion and next steps for this project. The thoughts and ideas described in this chapter are my own, though my supervisors and the ChDR collaboration have provided feedback.

ABSTRACT

This research project is to assess the feasibility of using incoherent Cherenkov Diffraction Radiation (ChDR) emission from dielectric radiators as a non-invasive optical method of detecting the transverse beam position of ultra-relativistic charged particle beams. Ultra-relativistic charged particle beams are found in many particle accelerator facilities such as: high energy colliders, free electron lasers, and synchrotron light sources. A non-invasive optical beam position monitor could be located inside fields of high magnetic flux allowing for a position measurement in accelerator locations that are unavailable with traditional beam position monitors.

Using the beam test stand at Diamond Light Source experiments for this thesis have been carried out. These experiments use the 3 GeV electron beam that is available for the testing of accelerator components and diagnostic instrumentation. Experimental work conducted during this thesis includes the commissioning of the modified beam test stand at Diamond Light Source, followed by a number of experiments examining the properties of ChDR, allowing for the comparison with theory and simulations. By developing simulations and comparing with experimental data, a feasibility study has been carried out providing the necessary requirements for building a non-invasive transverse ChDR beam position monitor in the near infrared and visible wavelength detection region.

CONTENTS

LIST OF FIGURES

LIST OF TABLES

LIST OF ACRONYMS

ATF2	Accelerator Test Facility 2
BPM	Beam Position Monitor
BTS	Beam Test Stand
BU	Bump Unit
CAD	Computer Aided Design
CCD	Charge-Coupled Device
CDR	Conceptual Design Review
CERN	European Organization for Nuclear Research
CESR	Cornell Electron Storage Ring
ChDR	Cherenkov Diffraction Radiation
CIA	Control Instrument Area
CLARA	Compact Linear Accelerator for Research and Applications
CLEAR	CERN Linear Electron Accelerator for Research
CR	Cherenkov Radiation
CVD	Chemical Vapor Deposition
DAQ	Data Acquisition
DR	Diffraction Radiation
EPICS	Experimental Physics and Industrial Control System
ESRF-EBS	European Synchrotron Radiation Facility Extremely Brilliant Source
European XFEL	European X-Ray Free-Electron Laser
FEA	Finite Element Analysis
FEL	Free Electron Laser
FFT	Fast Fourier Transform
FWHM	Full Width Half Max
IBPM	Inductive Beam Position Monitor
ICT	Integrating Current Transformer
ID	Insertion Device
IOC	Input/Output Controller
IR	Infrared
IW2D	ImpedanceWake2D
JAI	John Adams Institute
LHC	Large Hadron Collider
MBA	Multi Bend Achromat
MCP	Micro Channel Plate

MD	Machine Development
NIR	Near-Infrared
ODR	Optical Diffraction Radiation
OTR	Optical Transistion Radiation
PCA	Polarisation Currents Approach
PMT	Photomultiplier Tube
PR	Polarisation Radiation
QE	Quantum Efficency
RF	Radio Frequency
ROI	Region Of Interest
SNR	Signal-to-Noise Ratio
SPR	Smith-Purcell Radiation
SR	Synchrotron Radiation
TEM	Transverse Electro-Magnetic
TIR	Total Internal Reflection
TR	Transition Radiation
UML	Unified Modelling Language
YAG	Yttrium Aluminium Garnet

CHAPTER 1

INTRODUCTION

Accelerator facilities require precise control of the beam position: for a high energy collider this allows for maximum crossover between the two beams, and for a light source this allows for stability at the Synchrotron Radiation (SR) source. Accelerators are typically designed for a specified reference orbit, should the beam position drift too far from this reference orbit the accelerator optics cannot be guaranteed to keep the beam contained. This will reduce the performance of the experiments the beam is used for or potentially create unwanted beam loss.

In order to control the beam position it must first be measured using suitable beam position monitors. Research for this thesis has been conducted to examine feasibility of using incoherent Cherenkov Diffraction Radiation (ChDR) to measure the transverse position of a charged particle beam. As optical signals and fibres are unaffected by magnetic fields, a ChDR Beam Position Monitor (BPM) could be installed in accelerator locations with high magnetic flux. Installing a traditional BPM in such a location would introduce additional complications such as modifying the magnetic field configurations [1].

A ChDR BPM could be deployed at any facility with ultra-relativistic charged particle beams such as a high energy collider, Free Electron Laser (FEL), or synchrotron light source. Experiments for this project have been carried out at the Beam Test Stand (BTS) located on the booster to storage ring transfer line at Diamond Light Source. This research has examined where a non-invasive ChDR BPM could be used for a future upgrade to the Diamond accelerator facility.

Chapter 1 details the motivation for this project, e.g. why a non-invasive optical BPM diagnostic would be of value in accelerator facilities, specifically the 4th generation synchrotron light sources. Also listed in Chap. 1 is an overview of the most common BPM devices found in accelerator facilities. Chapter 2 explores the theory of Polarisation Radiation (PR) and the properties of ChDR, with a focus on how ChDR can be generated from different radiators and used to measure transverse beam position. The experimental setup installed on the Diamond BTS is detailed in Chap. 3; this examines the setup of the experimental station with the data acquisition equipment. The commissioning of the BTS test stand and diagnostic devices is stated in Chap. 4. For this research project a simulation framework has been produced to predict ChDR characteristics; Chap. 5 details the simulation framework and a full set of simulations produced for the Diamond BTS. As a large amount of the data taken for this research project has been in image format, different image processing techniques were examined with the results shown in Chap. 6. The experimental ChDR results taken for this project along with analysis and interpretation are detailed in Chap. 7. The conclusion and critical evaluation are then presented in Chap. 8.

1.1 4th Generation Synchrotron Light Sources

SR is the electromagnetic radiation emitted by a highly relativistic charged particle when it is radially accelerated [2]. For decades, purpose-built particle accelerator facilities have been constructed in order to generate this radiation [2]. The purpose of such facilities is to use the SR for studying samples with techniques such as, X-ray diffraction, spectroscopy, imaging, and more [2]. The SR power P_γ emitted by a charged particle in a magnetic field, is given by

$$P_\gamma = \frac{1}{6\pi\varepsilon_0}\frac{e^2c}{\rho^2}\gamma^4, \tag{1.1}$$

where e is the charge of the particle, ε_0 is the vacuum permittivity, c is the vacuum speed of light, ρ is the magnetic bending radius, and γ is the Lorentz factor [2]. The Lorentz factor is given by

$$\gamma = \frac{E}{m_0c^2}, \tag{1.2}$$

where E is the energy of the particle, and m_0 the rest mass [2]. Noting that Eq.1.1 has a γ^4 component, as the rest mass of the particle reduces the SR power greatly increases. Electrons and protons have a rest mass of $0.511\,\mathrm{MeV/c^2}$ and $938\,\mathrm{MeV/c^2}$ respectively. Equation 1.1

shows that for a proton and electron of the same energy the electron will produce SR that is orders of magnitude higher. This makes particles with a low rest mass such as electrons ideal candidates for SR facilities [2].

As a relativistic particle is required to accelerate radially to emit SR, radiation is emitted when the particle passes through a magnetic dipole field. Modern SR facilities have several sources that generate SR, each source will be either; a dipole bending magnet, a wiggler, or an undulator. Figure 1.1 shows the three different types of sources, their respective magnet arrangements, and SR spectral distributions [3]. A dipole magnet source is a single magnet, whereas a wiggler and undulator use an alternating series of magnets that increases the SR photon yield. Active sources like a wiggler or an undulator can be collectively referred to as an Insertion Device (ID) [3].

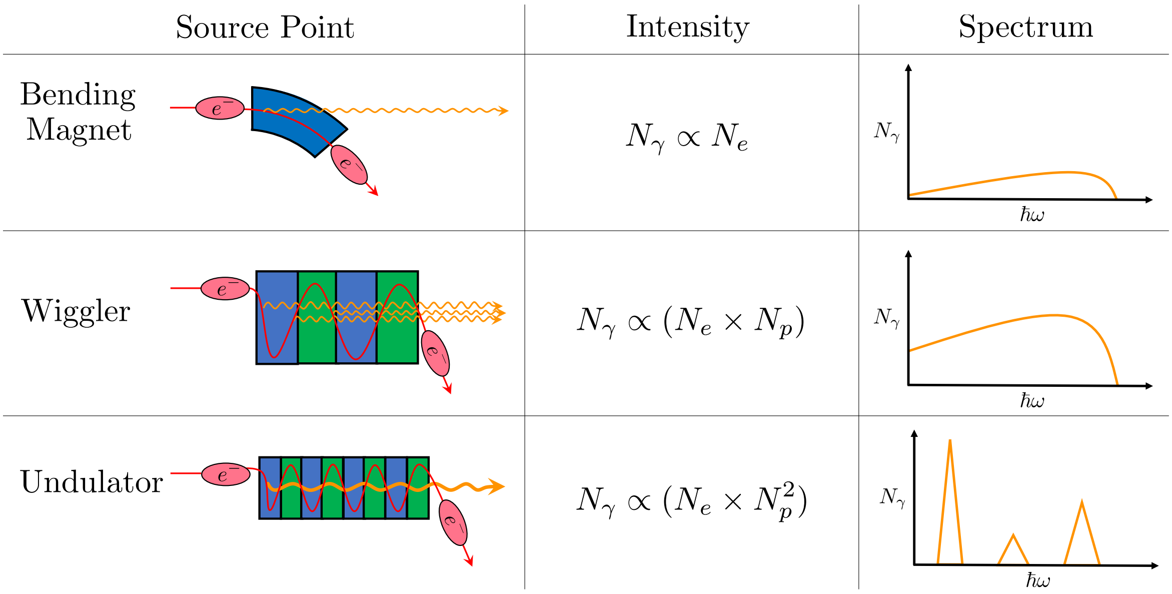

Figure 1.1: Synchrotron radiation sources, their relative photon intensities and spectral distributions [3]. Where N_γ is the photon yield, N_e is the number of electrons, N_p is the number of magnet periods, $\hbar$ is the reduced Planck constant, and ω is the the radial frequency of the emitted SR.

.

Dipoles and wigglers produce a broad spectrum of SR towards the beamline, whereas an undulator produces a narrow spectral distribution where the emission wavelengths are tuned to produce a coherent effect by altering the magnet setup [3]. Figure 1.1 shows the respective relative photon yield and spectral distribution for each source, it shows that ID sources produce a much higher photon yield and are thus more desirable in a SR facility.

The accelerator for a modern SR facility is either synchrotron or a FEL. A FEL features a Linac with a long undulator. As the electron beam passes through the long undulator intense coherent SR is produced [3]. At the end of the undulator the electron beam is diverted to a beam dump using a dipole magnet while the coherent SR is allowed to pass into the experimental areas. The advantage of a synchrotron light source is that the SR sources are tangential to the ring allowing for more experimental beamlines than a FEL. The repetition rate for a synchrotron source is dictated by the number of bunches in the ring and the revolution frequency, at Diamond Light Source this is approximately 500 MHz [4]. The European X-Ray Free-Electron Laser (European XFEL) facility extracts pulse trains at a rate of 10 Hz where each train contains up to 2700 X-ray pluses. The smallest spacing between these pulses is 220 ns giving a maximum frequency of 4.5 MHz for each train [5]. The key difference here is the duty cycle of each type of machine, Diamond will produce SR at approximately 500 MHz continuously during operations, whereas European XFEL will produce SR at 4.5 MHz for 600 µs at a rate of 10 Hz [5].

Figure 1.2 shows the schematic of Diamond Light Source. In order to generate SR, electrons are first emitted from an electron gun at the start of the Linac. The electron gun is comprised of a heating element and a system to provide a bias voltage. As the heating element warms up the bias voltage is used to pull these electrons away from the element and accelerate them into the rest of the Linac. The Linac accelerates the electrons up to 100 MeV before they are injected into the Booster synchrotron [6]. The Booster synchrotron accelerates injected electrons up to their top energy of 3 GeV, after which they are extracted into the storage ring that has a circumference of 561.6 m [4]. Beamlines are tangentially distributed around the storage ring from different sources where a variety of SR experiments take place.

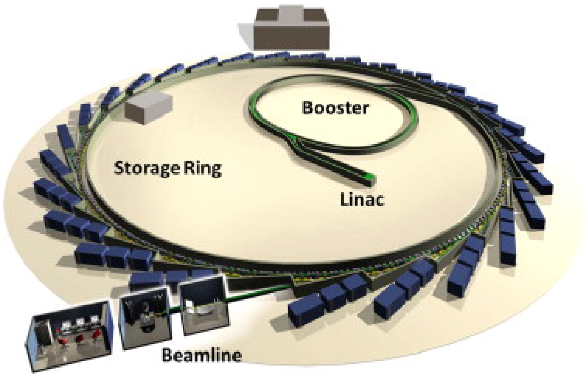

Figure 1.2: Diamond Light Source schematic [6].

The brilliance (or brightness) is the measure of a SR source point quality [7], where brilliance has the units of

$$\text{brilliance} = \frac{\text{photons}}{\text{second} \cdot \text{mrad}^2 \cdot \text{mm}^2 \cdot 0.1\%\ \text{BW}}, \tag{1.3}$$

where 0.1% BW is the wavelength range around a specific wavelength defined as

$$0.1\%\ \mathrm{BW} = \frac{\Delta\lambda}{\lambda} = 10^{-3}. \tag{1.4}$$

The brilliance of SR is inversely proportional to the emittance of the beam used to produce it. The emittance of a beam is a parameter of the beam size and parallelism with units of m rad. Given the relationship between emittance of a beam, and the brilliance of produced SR reducing the emittance increases the brilliance. [3]. A 4th generation synchrotron light source achieves ultra-low emittance and hence increased brilliance using an Multi Bend Achromat (MBA) lattice [4].

For the Diamond Light Source, a Conceptual Design Review (CDR) has been published that details an accelerator design upgrade to a 4th generation synchrotron light source, Diamond-II [4]. The current horizontal emittance in the storage ring is 2.7 nm rad, this will be upgraded to 160 pm rad [4], whereas the vertical emittance remains largely unchanged at 8 pm rad. The horizontal emittance is reduced in a MBA lattice by increasing the number of magnets as the horizontal emittance has been seen to scale with

$$\epsilon_x \propto \frac{1}{N_x^3}, \tag{1.5}$$

where ϵ_x is the horizontal emittance and N_x is the number of horizontal bending magnets [4]. Figure 1.3 shows the cell layout of the existing Diamond storage ring, and the proposed upgrade. By increasing the number of bending magnets in each arc, the horizontal emittance will be reduced and new straight sections will be created for additional ID beamlines.

1.2 Beam Dynamics

Beam position is a key parameter of any particle accelerator. When considering a collider such as the Large Hadron Collider (LHC), beam sizes are as small as 2.5 µm and must collide with each other [8]. In order to collide two beams of such size, accurate measurement and control over beam position is needed.

Synchrotron light sources also have a large number of BPMs, for example the European Synchrotron Radiation Facility Extremely Brilliant Source (ESRF-EBS) low emittance ring has 320 BPMs [9]. Many modern synchrotron light source facilities incorporate orbit correction feedback systems. Such systems use BPMs and corrector magnets to keep the beam fixed at key points. One reason feedback systems are necessary is because the beam position will be

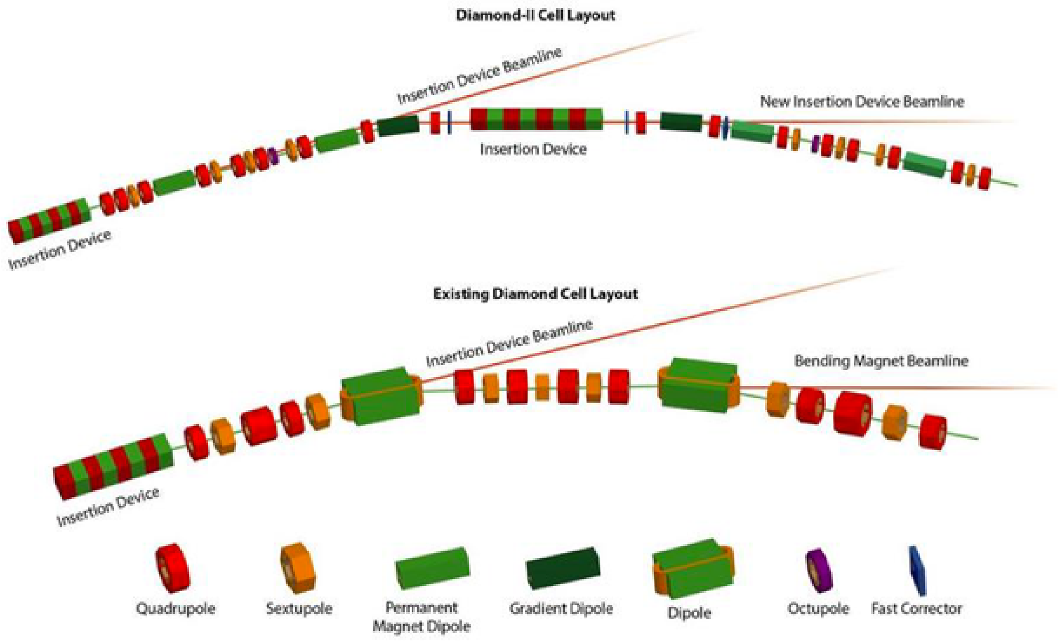

Figure 1.3: Diamond and Diamond-II storage ring cell layout [6].

subjected to disturbances, in order to control and measure the beam position knowledge of the relativistic charged particles and types of beam disturbances must be understood [10].

1.2.1 Relativistic Charged Particles

A transverse BPM pickup will intercept the transverse electric field of the particle beam. The magnitude of the electric field depends on the electrical field strength of the charged particle, where the transverse electric field potential, $\vec{\mathrm{E}}$, from a single stationary particle in a vacuum is given by

$$\vec{\mathrm{E}} = \frac{q}{4\pi\varepsilon_0 r^3}\hat{r}, \tag{1.6}$$

where q is the charge of the particle, ε_0 is vacuum permittivity, and r is the distance from the particle [11]. The electric field potential reduces further as the distance from the particle increases. This gives rise to a positional and charge dependence when measuring the field potential.

Figure 1.4 shows three particles. Figure 1.4a is stationary and has an electric field that extends equally in all directions such that

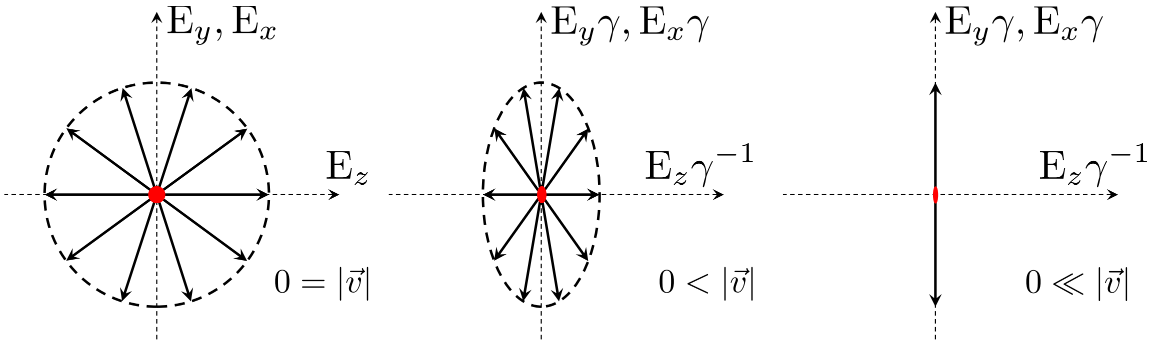

(a) Stationary. **(b)** Relativistic. **(c)** Ultra-relativistic.

Figure 1.4: Point charge electric field distributions [12].

$$E_x = E_y = E_z, \tag{1.7}$$

where $E_{x,y,z}$ is the electric field component on a single axis where x denotes the horizontal transverse axis, y the vertical transverse axis, and z the longitudinal axis. A moving point charge will undergo a length contraction in the direction of travel and an extension in the transverse direction [12]. Figure 1.4b shows a charge moving in the direction of the longitudinal axis [12]. The length contraction in Fig. 1.4b reduces the electric field in the longitudinal direction, and increases the electric field in the transverse plane. The scale of the length contraction and extension of a moving point charge is given by the Lorentz factor γ that is expressed by

$$\gamma = \frac{1}{\sqrt{1 - \left(\frac{v}{c}\right)^2}}, \tag{1.8}$$

where v is the velocity of the particle, and c is the speed of light in a vacuum [12]. The ultra-relativistic case ($\gamma \gg 1$) is seen in Fig. 1.4c. The scale of the length contraction and extension in Fig. 1.4c is so large that the electric field can be approximated as transverse only. Such particles are found in synchrotron light sources, FELs, and high energy colliders.

Rearranging Eq. 1.2 the relation between particle energy E and the Lorentz factor is

$$E = \gamma m_0 c^2. \tag{1.9}$$

When measuring the transverse electric field of the particle there will be a particle energy dependence that arises because the transverse electric field increases with the Lorentz factor. In additional to the transformed electric field a magnetic field $\vec{B}$ arises for a moving point charge. Figure 1.5 extends azimuthally around the direction of travel of the point charge. The magnetic field is then given by

$$\vec{B} = \frac{\vec{v} \times \vec{E}}{c^2}, \tag{1.10}$$

where $\vec{v}$ is the velocity of the particle, and $\vec{E}$ is the electric field of the point charge [12].

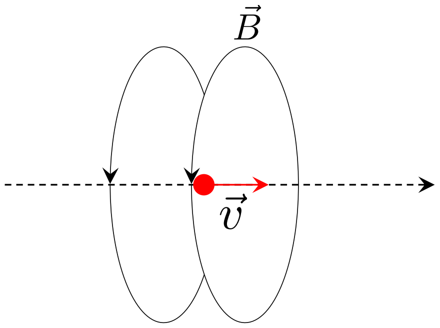

Figure 1.5: Transverse magnetic field generated by a relativistic moving charge [12].

1.2.2 Beam Position Disturbances

Beam disturbances will shift the transverse beam position from a known or desired beam orbit. A number of beam dynamic effects will cause the beam position to vary unintentionally this highlights why beam position monitors are a vital accelerator component.

A key source of beam position disturbance in an accelerator is due to noise from accelerator magnets. Dipole magnets bend particle beams in a single direction, quadrupole magnets are used for beam focusing, and sextupole magnets are used to correct for chromaticity [2]. All of these magnets influence the transverse beam position any fluctuations in their magnetic field will contribute to noise on the position, and generate poor beam stability. The majority of magnets in accelerators are electromagnets, the result is that their magnetic field is subjected to changes in their power supplies. Noise of magnet power supplies can be caused by a number of sources of electronic noise e.g. capacitive, inductive, thermal. All of these effects will in turn influence the beam position [13].

Another cause of beam position disturbance occurs from the betatron tune which is the number of transverse oscillations in one revolution of the accelerator ring [14]. If the betatron tune is an integer or integer multiple the amplitude of these oscillations increases with each revolution [2, 14]. If left unchecked this amplitude can increase to a point where the beam becomes unstable. To avoid this the tune is set to an irrational number of oscillations so the deviation does not build on successive revolutions. Successfully implementing an irrational tune means each bunch will arrive at a BPM with a different phase for each revolution.

Collective effects are the effects of having multiple particles and bunches inside an accelerator. These effects result in instabilities that cause beam disturbances. An example of collective effects are resistive wall impedances or wakes. An electromagnetic wake is generated when a charged particle or bunch passes through a vacuum vessel. If the wake functions generated are still present when the next bunch enters the vessel this will create a coupled bunch instability where the wake function will result in an altered beam position [15].

1.3 Transverse Beam Position Diagnostics

1.3.1 Electrostatic Beam Position Monitors

Electrostatic or capacitive BPM pickups are commonly used in accelerators [16]. Conceptually, each pickup is a metallic electrode set around or inside the vacuum chamber. As the charged particle beam passes the electrode currents are induced that can be read by an appropriate electronic measuring system [16]. The currents induced are dependent on the distance from the particle beam. By incorporating multiple pickups around the vacuum chamber, the beam position is deduced. There are two types of electrostatic BPM pickups that are commonly used in accelerators: split-plane and button.

A common type of split-plane pickup is the shoebox BPM (see Fig. 1.6). This is a cuboid design that has a cut along the diagonal giving two electrodes around the entire vacuum chamber. If the beam is offset to the right, then the right electrode will intercept more of the electric field, such that the measured voltage amplitude on the right side is higher, and vice versa for the left side [17].

As the shoebox BPM is cut along the diagonal it is only sensitive in either the horizontal or vertical plane depending on the orientation. For the BPM shown in Fig. 1.6 the horizontal beam position is measured by applying the relationship

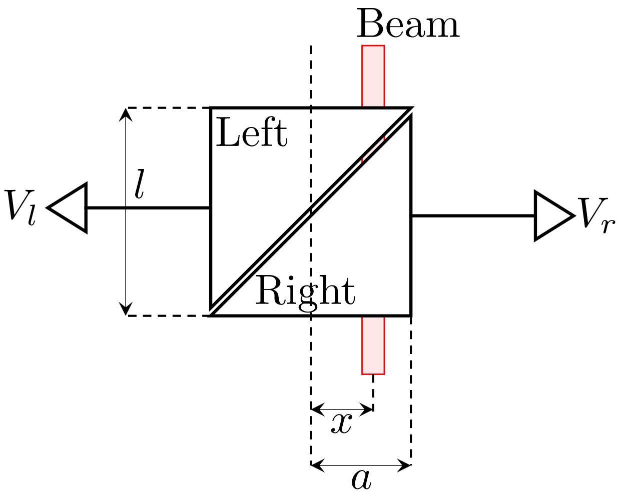

Figure 1.6: Shoebox BPM Schematic [17].

$$x = a\frac{V_r - V_l}{V_r + V_l}, \tag{1.11}$$

where V_l and V_r are the voltages measured from the left and right pickups respectively, x is the horizontal beam position, and a is a geometrical scaling factor equal to half of the width of the BPM [17]. Each electrostatic pickup is sensitive to the beam energy, intensity, and position. As the intensity and energy is the same for both pickups this dependence is cancelled out for each V term in Eq. 1.11 [17].

Shoebox BPMs have a linear response and a low cut-off frequency in the order of kHz. The cut-off frequency is defined by the low pass frequency response of the BPM. If the bunch repetition rate is above cut-off frequency the BPM will fail to adequately measure a signal. The low cut-off frequency of a shoebox BPM makes them ideal for accelerators that have a low revolution frequency, such as low energy hadron accelerators [17]. This design can only measure one plane. In order to use the shoebox design to measure the vertical position of the particle beam, the BPM is mounted at 90° to Fig. 1.6 and the relationship

$$y = a\frac{V_t - V_b}{V_t + V_b}, \tag{1.12}$$

is used instead of Eq. 1.11, where V_t and V_b are the voltages measured at the top and bottom pickups respectively, and y is the measured vertical beam position [17].

Button BPM pickups have a small circular design that resembles a button (see Fig. 1.7). Four of these pickups are inset into the vacuum wall to simultaneously obtain the horizontal and vertical beam position.

Figure 1.7: Button BPM pickup [16, 18].

The pickups in a four button BPM design are mounted so that they avoid the horizontal plane. This is done to reduce or remove SR interfering with the measurement [16, 18]. The four button design typically used at a synchrotron light source is shown in Fig. 1.8.

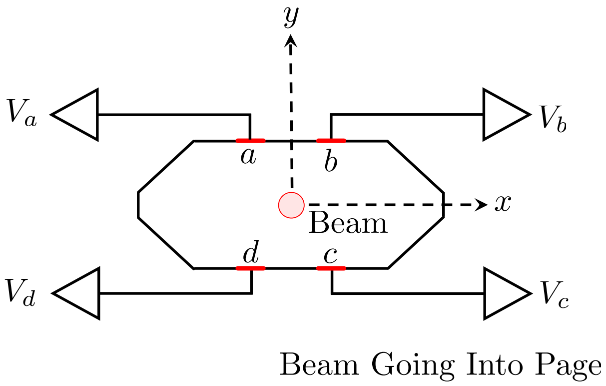

Figure 1.8: Button BPM Schematic [16, 18].

Unlike the shoebox BPM design, button BPMs exhibit a non-linear pin-cushion effect with increased non-linearity at large offsets from the electrical centre of the BPM [16, 18]. With small beam position deviations from the centre the equations

$$x = k_x \frac{(V_a + V_d) - (V_b + V_c)}{V_a + V_b + V_c + V_d}, \tag{1.13}$$

$$y = k_y \frac{(V_a + V_b) - (V_c + V_d)}{V_a + V_b + V_c + V_d}, \tag{1.14}$$

can be used, where k_x, and k_y are half the width of the and height of the BPM respectively.

The voltages at each corresponding button pickup are V_a, V_b, V_c and, V_d [16, 18]. Figure 1.9 shows a typical uncorrected BPM response, as the beam position moves further away from the centre the difference between the normalised beam position and the BPM response gets larger. To account for the non-linear response of a button BPM the entire response area is mapped to a polynomial [16, 18].

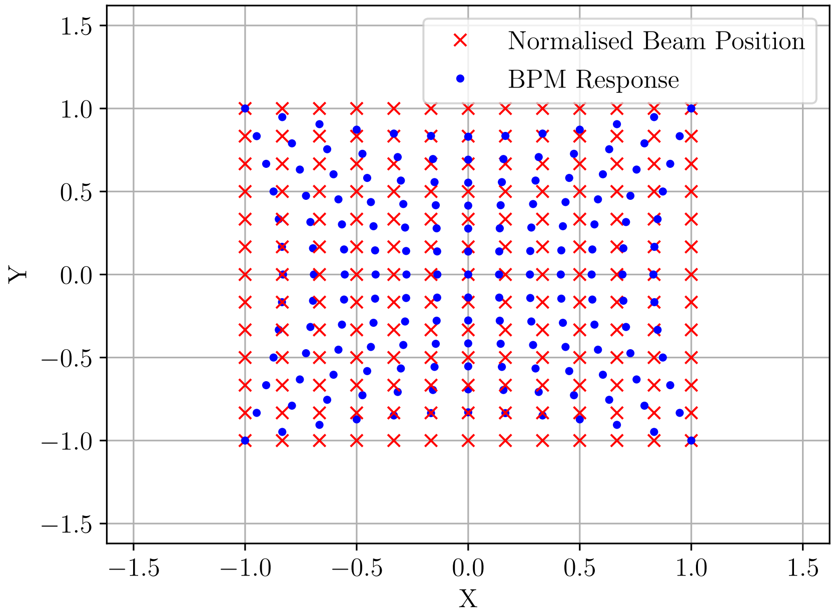

Figure 1.9: Example normalised button BPM pickup response [16, 18].

A button BPM has a cut-off frequency in the order of MHz making them suitable for machines that have high revolution frequencies such as synchrotron light sources or very high energy colliders [16, 18].

1.3.2 Electromagnetic Stripline Beam Position Monitor

An electromagnetic stripline BPM couples to the Transverse Electro-Magnetic (TEM) mode created by the electric field of the passing beam [18, 19]. Figure 1.10 shows the schematic of a two pickup stripline BPM, consisting of a matched transmission line with an upstream and downstream port for each pickup. When the beam passes an upstream port a signal is measured at that port and a reflection is created that moves along the stripline towards the downstream port. Once the beam reaches a downstream port another reflection is created and sent down the stripline towards the upstream port. The reflection from the upstream port, and the pulse generated at the downstream port then cancel at the downstream port [18]. The end result is two pulses of alternating sign measured on each upstream port only [18].

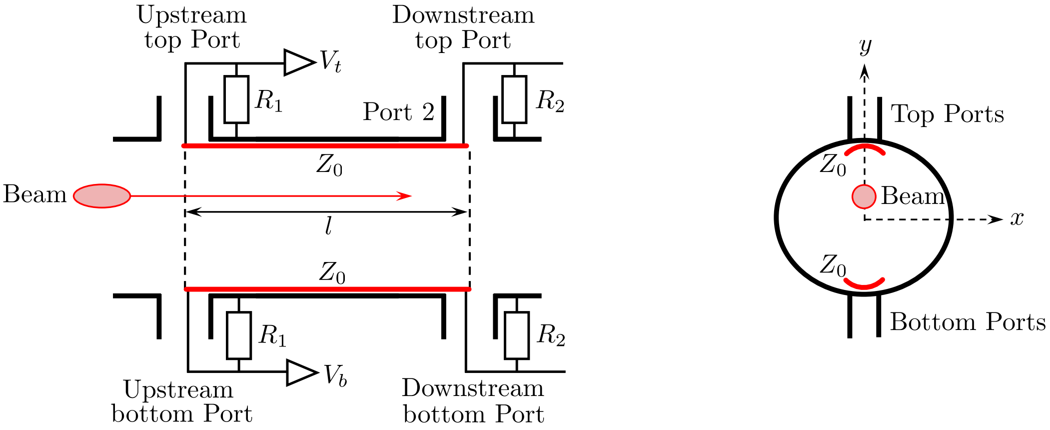

(a) Longitudinal View. **(b)** Transverse View.

Figure 1.10: Stripline BPM Schematic [17, 18].

As the signal is only present at the upstream ports, a stripline BPM can be used as a directional coupler to measure the position of counter circulating beams. The design shown in Fig. 1.10a shows a two pickup design that has a beam passing from left to right. For this example signals are only measured on the top and bottom upstream ports. The measured voltages from the stripline ports are designated as V_t and V_b for the top and bottom ports respectively. The magnitude of the measured pulses have a positional dependence that allows Eq. 1.12 to be used for this BPM design, provided the geometrical scaling factor is adjusted accordingly [18, 19].

The ports of a stripline BPM are terminated with loads, $R1$ and $R2$. In order for the signal and reflection to cancel, the loads must match the characteristic impedance, Z_0, of the stripline pickup, typically $50\,\Omega$ (see Fig. 1.10) [18, 19]. A constraint is that the length of the stripline pickup, l, must be longer than the bunch length of the beam, otherwise signals will be created at both ports simultaneously inhibiting the desired double pulse generation and reflection cancellation. The downstream ports of a stripline BPM can be terminated to ground if there is no desire to obtain the direction of the beam [18, 19]. Such a BPM design is not limited to a two pickup design, a design with four or more pickups can be used to simultaneously obtain the horizontal and vertical beam position [18, 19].

1.3.3 Cavity Beam Position Monitor

A cavity BPM is a passive resonator. When a charged particle beam moves through the cavity a wake potential is caused by the TEM modes of the beam [18, 20]. In a cylindrical pillbox design (see Fig. 1.11) the TEM_{110} dipole mode is used to measure the beam position. In order to do this, the TEM_{010} monopole mode must be discriminated out, potentially by adding high pass filter waveguides to the BPM [18, 20]. Additionally in order to normalise the charge dependence of the cavity BPM a monopole mode reference cavity is used [20].

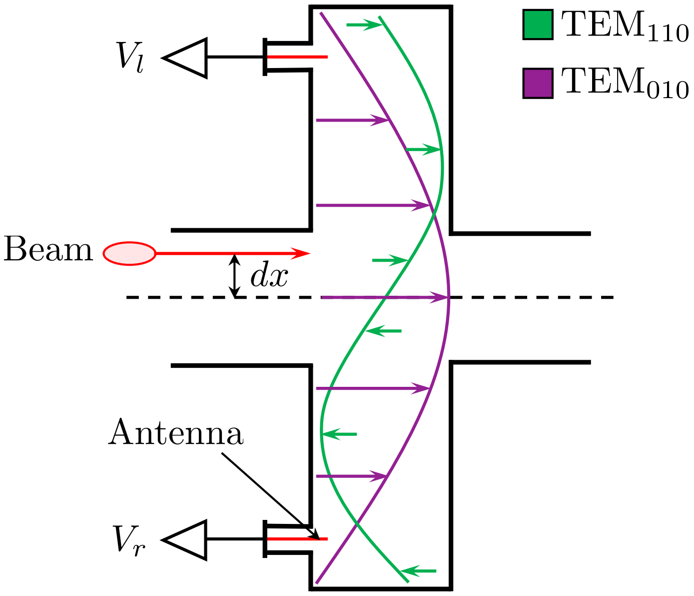

Figure 1.11: Cavity BPM Schematic [18, 20].

Figure 1.11 shows a cavity BPM with the TEM$_{110}$, and TEM$_{010}$ modes. This design could be expanded to four antennas in order to obtain the horizontal and vertical position from the TEM$_{110}$ mode. The benefit of using a cavity BPM is that the signal transfer is high giving a high resolution measurement that can be as precise as a few nm [18, 20]. The downside of a cavity BPM is that the coupling impedance of such a BPM is high causing instabilities that typically limits the use of such a BPM to a linear accelerator or transfer line [18, 20].

1.3.4 Inductive Beam Position Monitor

An Inductive Beam Position Monitor (IBPM) is less common than the other BPMs listed in this chapter, though one is installed on the modified Diamond BTS where experiments for this research project have been carried out. An IBPM schematic is shown in Fig. 1.12. By placing a ceramic break in the vacuum vessel the beam image current goes through the electrodes instead of the vacuum vessel [21]. Figure 1.12 shows four electrodes that are placed around the vacuum vessel orthogonally, acting as pickups. The total beam image current that goes through the IBPM will be dependent on the beam intensity and energy [21]. The proportion of the total beam image current going through each electrode of the IBPM will be dependent on the proximity of the beam to the electrode giving a beam position dependence [21].

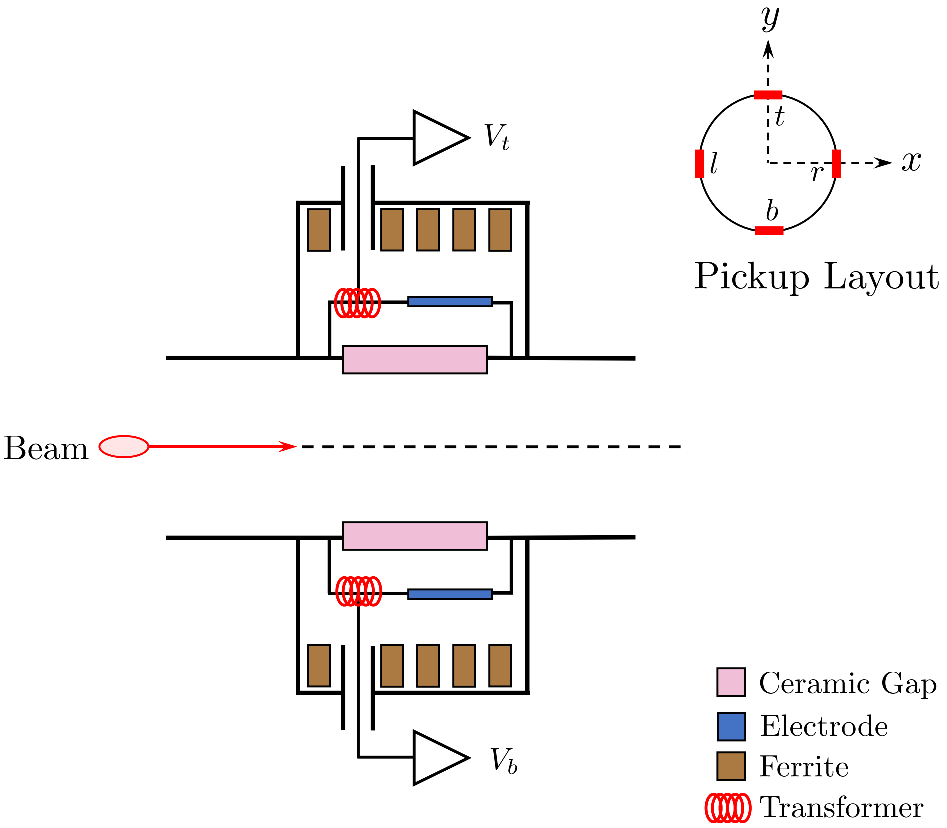

Figure 1.12: Inductive BPM Schematic [21].

A transformer circuit is used to convert the image current through each IBPM electrode path into a voltage that can be measured using a data acquisition system. Like other BPM systems the inductive BPM design would need at least four electrodes in order to obtain the vertical and horizontal beam positions simultaneously. Unlike button BPMs these can be placed orthogonally around the beam pipe, as SR will not interfere with the signals generated [21]. Similar to a button BPM an IBPM has a response like the one seen in Fig. 1.9. If the beam position deviation from the centre is small the IBPM response is linear. Inside the central region these signals are used in the difference over sum the relationship seen in Eq. 1.11 and 1.12, where the geometrical scaling factor is adjusted for the IBPM. Similar to a button BPM the entire region can be mapped to a polynomial when venturing outside of the central region.

As an inductive BPM works on the same principle as a wall current monitor, it can also be used to measure the beam charge, using the relationship

$$Q = k_Q(V_t + V_b + V_l + V_r), \tag{1.15}$$

where Q is the measured charge, k_Q is the charge scaling factor [21], and $V_{t,b,l,r}$ is the voltage measured at each pickup. In order to measure the bunch charge the signals are integrated over the bunch length. Knowledge of the bunch repetition rate can then be used in order to calculate the average beam current as

$$I = N_B Q_B, \tag{1.16}$$

where I is the average beam current, Q_B is the average bunch charge, and N_B is the number of bunches per second [21].

1.4 Motivation for a Cherenkov Diffraction Radiation Beam Position Monitor

All of the different beam diagnostic monitors listed in Sec. 1.3 measure the transverse position of a particle beam using Radio Frequency (RF) or inductive pickups. The signals created from such pickups are transported using metallic cables or waveguides. Installing a metallic cable or waveguide into a dipole magnet or ID would perturb the magnetic field affecting operation [1]. The operation of a pulsed magnet would impact the position measurement through the creation of eddy currents inside the metallic transport medium [1].

The method of using ChDR as a technique for measuring the beam position is a development towards the creation of a non-invasive optical BPM pickup. Electrical pickups require the use of cables or waveguides to couple the signal out of the BPM vacuum vessel. An optical system would use a viewport, or a fibre optic feed-through in order to couple the signals out of the BPM vacuum vessel. Optical fibres have the benefit of leaving magnetic fields unperturbed when they are installed inside them. Additionally the signals transported through the fibres are unaffected by the magnetic fields [22]. This leverages developments in the telecommunications and FEL communities where optical fibres are used to transfer large amounts of data and high speed timing signals [23].

Optical beam diagnostics such as: synchrotron light monitors, Optical Transistion Radiation (OTR) monitors, and Optical Diffraction Radiation (ODR) monitors, and scintillator screens are used extensively in synchrotron facilities [24, 25]. While ChDR is a novel technique for beam position monitoring the knowledge and skills required to use and develop such a system already exists in accelerator facilities. Additionally the optical diagnostics currently used on accelerators are primarily used for beam profile measurements and provide limited beam position measurements by fitting a centroid to the profile. These position measurements are typically relative rather than absolute and have limited resolution. This is where a novel ChDR BPM could fill a niche [26].

An OTR monitor is a screen placed into the beam at 45°, with an optical detection system facing the screen to measure the beam profile. As an OTR monitor is invasive it is not possible to use in a circulating beam as the energy deposition from the beam will cause the screen to become damaged under typical beam parameters [27]. A synchrotron light monitor measures the profile of the synchrotron light emitted from a dipole magnet or ID . While this is an accurate and non-invasive way to measure parameters of the particle beam, this requires space for an extraction line and detection system. It has already been shown in Fig. 1.3 that future synchrotron light source storage rings will feature more dipole magnets of shallower bends limiting the space available for synchrotron light monitors. This is particularly relevant for operations at visible wavelengths. To couple out visible wavelengths an in vacuum mirror and viewport arrangement is needed in order to extract the SR. Given that 4th generation synchrotron light sources typically have a reduced beam pipe diameter this becomes very difficult [4].

An ODR monitor is both an optical and non-invasive diagnostic that has been proven to work sufficiently well for linear machines [28]. ODR can also be used for diagnostics in circular machines but unless the beam energy is excessively high this will have an impact on the beam lifetime by scraping halo particles [25]. While the centroid from a beam profile can be used as a relative position measurement, the readout of a BPM is typically desired to be faster in order to acquire a bunch-by-bunch measurement. Such a measurement could feasibly be achieved with a ChDR system using a photodetector and fast digitiser.

The development of ChDR as a diagnostic technique aims to build up upon the research for OTR and ODR monitors, as they are all built on the theory of PR [26]. OTR and ODR monitors are both surface emitters and increasing the photon yield from each is non-trivial. ChDR is an extended emitter meaning higher photon yields may be possible by simply increasing the length of the pickup [29, 30]. ChDR also allows for radiator designs that are directional, enabling opportunities for facilities with counter rotating beams like high energy colliders [31].

Diamond-II plans consider the use of glass brazing on new BPM pickups [4]. As ChDR radiators can be made from fused silica there is potential to use glass brazing techniques to build a ChDR BPM embedded into the vacuum vessel. By leveraging optical fibre systems and ceramic manufacturing techniques already being used in accelerator facilities and combing this with new MBA lattice designs, a ChDR BPM could prove to be a novel beam diagnostic device capable of measuring the bunch-by-bunch beam position in locations that are not currently possible.

CHAPTER 2

THEORETICAL BACKGROUND AND RADIATOR DESIGN

2.1 Polarisation Radiation

When a charged particle moves near or through a dielectric medium, the electric field of the particle will polarise the medium generating dipoles [29]. The dipoles generated are unstable, displaced electrons oscillate around the nucleus emitting time variant currents. These currents are called polarisation currents and give rise to PR [29, 30]. Figure 2.1 depicts the PR emission process, showing how the electron shell is stable until it is disrupted by a passing electron, where PR is then generated.

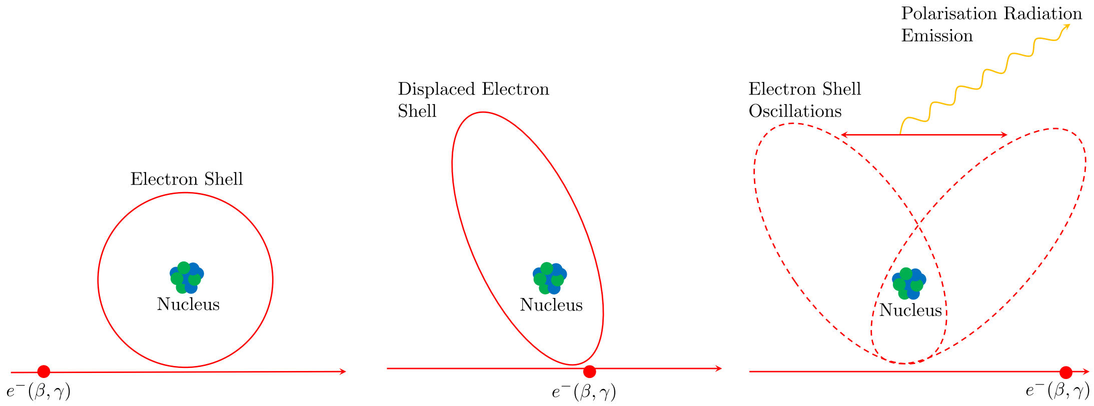

(a) Before the atom is affected by the electric field of an electron.

(b) Atomic dipole generated by the electric field of an electron passing by the atom.

(c) Atomic dipole moment oscillations causing polarisation radiation emission after an electron moves passed the atom.

Figure 2.1: Atomic process of PR emission from a relativistic electron [29].

The underlying emission process is the same for different types of PR but due to different radiator geometries there are different categories of PR. Transition Radiation (TR) occurs when a charged particle transitions through a boundary of two media that have different dielectric constants [32]. TR is typically generated by passing a charged particle or beam through a screen in vacuum [29]. Diffraction Radiation (DR) can be considered as a non-invasive form of TR, whereby the charged particle passes in close vicinity of a screen or medium, such as through an aperture [29]. Other types of PR include Cherenkov Radiation (CR) where a charged particle moves through a medium faster than the phase velocity of light in that medium [33], Smith-Purcell Radiation (SPR) when a relativistic charged particle passes over a diffraction grating [34], and ChDR where a charged particle travels parallel to, but not through, a medium at a velocity faster than the phase velocity of light in that medium [30]. For ChDR the distance between the medium and the charged particle is defined as the impact parameter. If a Gaussian beam passes the medium instead of a single particle the impact parameter is defined as the distance between the medium and the core centroid of the beam.

A theoretical model has been developed to describe all of the different types of PR, called the Polarisation Currents Approach (PCA) allowing them to be considered and simulated together [35–40]. This chapter seeks to detail the differences between CR and ChDR, as well as radiator geometries that are used to generate ChDR.

Several assumptions are made in the PCA model: The length of a radiator and impact parameters modelled are several times longer than the wavelengths of radiation. For visible and Infrared (IR) wavelengths this poses no problem, however to use this model for longer RF wavelengths, where the wavelengths are at least several mm long requires the radiators and impact parameters to be impractically long. Additional assumptions are made for the roughness of the radiator surfaces, and the interatomic distance inside the medium. The roughness of the surface of the medium must be far less than the wavelength of the emitted radiation, so that the medium surfaces are approximated as flat [30]. Additionally the interactomic distance must be far smaller than the radiation wavelength, for the radiator used for this project is made from Chemical Vapor Deposition (CVD) diamond that has an interatomic distance of approximately 0.35 nm [30]. All of these assumptions introduce restrictions and limitations into the PCA model.

2.2 Cherenkov Radiation

CR is the electromagnetic radiation emitted when a charged particle moves through a medium at a velocity faster than the phase velocity of light in that medium, giving rise to the Cherenkov condition,

$$v_p > \frac{c}{n}, \tag{2.1}$$

where v_p is the velocity of the particle, c is the speed of light in a vacuum, and n is the refractive index of the medium [33, 41]. If the Cherenkov condition (see Eq. 2.1) is met, the charged particle will polarise the dielectric generating polarisation currents giving rise to electromagnetic radiation [41]. The emission of CR occurs as a cone through the dielectric where the maximum of the polar angle is defined by the Cherenkov angle, θ_{Ch}, given by

$$\cos\left(\theta_{\mathrm{Ch}}\right) = \frac{1}{\beta n} = \frac{c}{v_p n}, \tag{2.2}$$

where β is the velocity of the particle relative to the velocity of light in a vacuum [33, 41]. Figure 2.2 shows a charged particle moving through a dielectric medium where the Cherenkov condition has been met, resulting in a CR wavefront created about the particle trajectory propagating at the Cherenkov angle [33, 41].

The behaviour of CR emitted inside a medium is defined by the Frank-Tamm equation, where the energy emitted, $\mathrm{d}E$, per unit of radial frequency, $\mathrm{d}\omega$, per unit length travelled by the particle, $\mathrm{d}x$, is

$$\frac{\mathrm{d}^2 E}{\mathrm{d}x \mathrm{d}\omega} = \frac{q^2}{4\pi}\varepsilon(\omega)\omega\left(1 - \frac{c^2}{v^2 n^2(\omega)}\right), \tag{2.3}$$

where q is the particle charge, ε and n are respectively the frequency dependent relative permittivity and index of refraction of the medium, and ω is the radial frequency of the radiation [41].

Many systems measuring Cherenkov radiation do so at visible wavelengths due to the availability of optical components and the sufficient photon yield. As such it is conventional to work with wavelength and photon yield. Transforming the Frank-Tamm equation this way

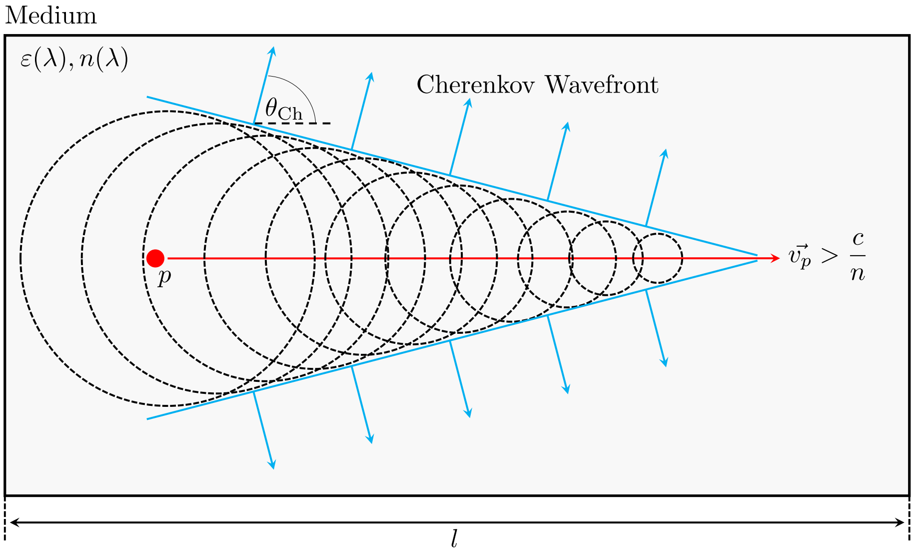

Figure 2.2: Cherenkov Radiation generated inside a medium, where $\varepsilon(\lambda)$ and $n(\lambda)$ are respectively the wavelength dependent permittivity and refractive index of the medium [42]. As the Cherenkov angle is constant in this diagram the refractive index and permittivity are constant, i.e. $n(\lambda) = n$, $\varepsilon(\lambda) = \varepsilon$.

gives

$$\frac{\mathrm{d}^2 N_\gamma}{\mathrm{d}\lambda \mathrm{d}x} = z^2 2\pi\alpha \left(1 - \frac{1}{\beta^2 n^2(\lambda)}\right)\left(\frac{1}{\lambda^2}\right), \tag{2.4}$$

where N_γ is the number of photons emitted, z is the relative atomic charge of the particle, α is the fine structure constant, and λ is the wavelength of the radiation [41]. Equation 2.4 shows that if the index of refraction is constant for the observed wavelengths as all other terms are constant the spectral response dependence is $1/\lambda^2$. Integrating the Frank-Tamm equation over the length of the radiator gives

$$\frac{\mathrm{d}N_\gamma}{\mathrm{d}\lambda} = z^2 2\pi\alpha l \left(1 - \frac{1}{\beta^2 n^2(\lambda)}\right)\left(\frac{1}{\lambda^2}\right), \tag{2.5}$$

where l is the length of the radiator [41, 43]. Figure 2.3 shows Eq. 2.5 computed for a highly relativistic electron ($\beta \approx 1$) travelling through a 10 mm fused silica radiator for the wavelength range 0.25 to 2 µm, where the refractive index of fused silica is set constant at 1.45, meaning that $n(\lambda) = n = 1.45$.

The photon yield at the visible wavelength 0.4 µm is much greater than that of 0.8 µm. To obtain the absolute CR photon yield between two wavelengths, Eq. 2.5 is integrated over an

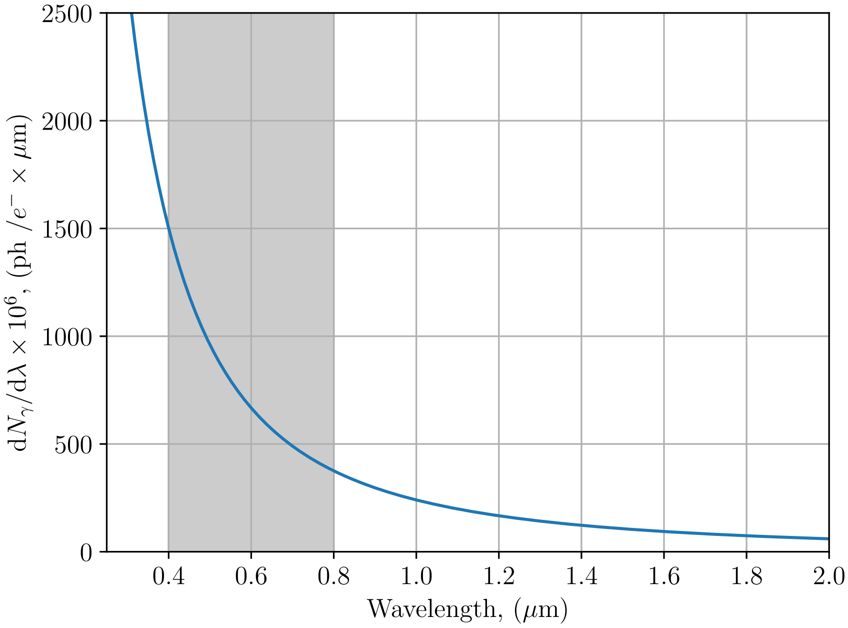

Figure 2.3: Cherenkov Radiation spectrum emitted by a highly relativistic ($\beta = 1$) electron moving through a 10 mm fused silica radiator, the shaded region highlights the visible wavelengths.

upper and lower limit. Provided that the index of refraction is constant over the integration range such that

$$n(\lambda) = n, \tag{2.6}$$

then the absolute photon yield is given by

$$N_\gamma = z^2 2\pi\alpha l \left(1 - \frac{1}{\beta^2 n^2}\right)\left(\frac{1}{\lambda_1} - \frac{1}{\lambda_2}\right), \tag{2.7}$$

where λ_1 is the upper limit, and λ_2 is the lower limit [41, 43].

2.3 Cherenkov Diffraction Radiation

ChDR is generated when a particle travels parallel to a medium at a velocity faster than the phase velocity of light in that medium. The field of the charged particle polarises that medium causing the emission of ChDR. As the particle is no longer inside the medium, effects

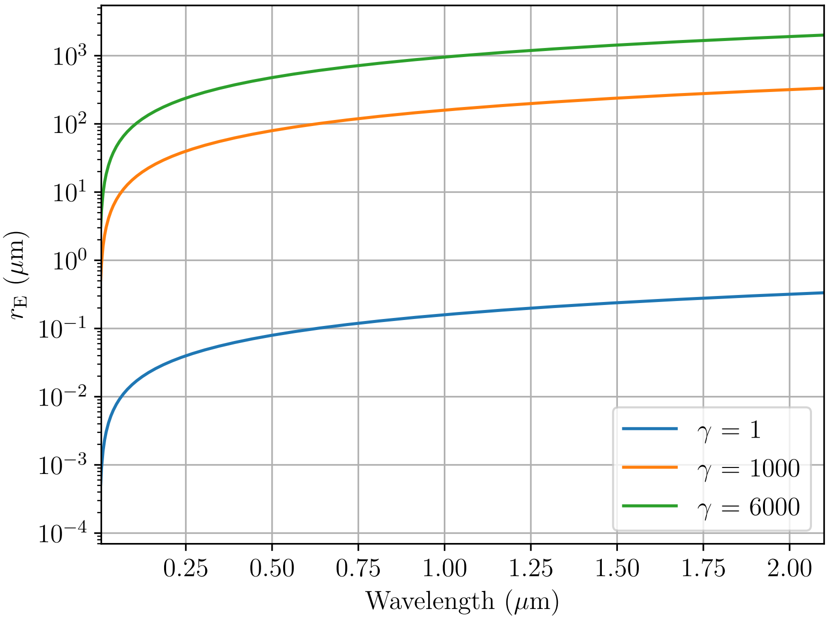

Figure 2.4: Effective electron field radius in the pre-wave zone for different Lorentz factors and wavelengths [44].

that happen at a distance must be accounted for.

For an electron the far-field approximation is typically used for its electric field source point size. For a relativistic electron as the transverse field strength increases (see Fig. 1.4) this size no longer becomes negligibly small, inside this area is called the pre-wave zone [44]. The effective electric field radius in the pre-wave zone of an electron r_E moving with a relativistic velocity is defined as

$$r_E = \frac{\gamma\lambda}{2\pi}, \tag{2.8}$$

where γ is the Lorentz factor of the electron, and λ is the wavelength of the radiation [44]. Outside of this region the electric field decays with a $1/r$ dependence.

Figure 2.4 shows the effective electric field radius size at different particle energies and wavelengths. It is shown that for high energy electrons similar to those found at Diamond, with a Lorentz factor of 6000 the field radius stretches up to approximately 1.5 mm for near-infrared wavelengths.

When a charged particle moves parallel to a medium, ChDR is emitted as long as the electric field of the particle interacts with the medium [30]. ChDR is generated inside the medium at the same distinct angle as CR (see Eq. 2.2), making it an interesting candidate for non-invasive beam instrumentation. The well defined angular nature of ChDR, allows it to be discriminated against other sources of optical noise such as SR [26, 45, 46].

The ChDR photon yield emitted by a radiator is dependent on the magnitude of the electric field that it intercepts. This makes ChDR radiators sensitive to beam position, beam energy and beam intensity (see Sec. 1.2.1). The simplest radiator geometry that is most analogous to CR is that of a dielectric pipe as the electric field is intercepted entirely in the transverse plane at a distance equal to the pipe radius. Figure 2.5 shows a dielectric pipe with a charged particle moving directly through the centre of the pipe, with the impact parameter b equal to the pipe radius.

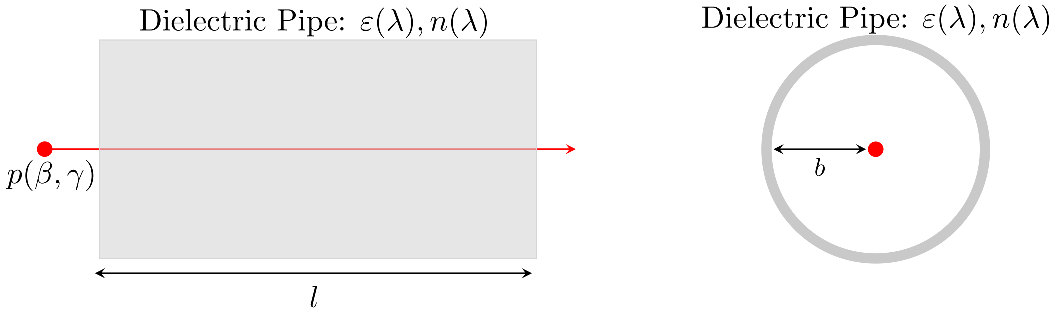

(a) Longitudinal View. **(b)** Transverse View.

Figure 2.5: Schematic of a dielectric pipe with a charged particle travelling through the centre.

The photon yield for a pipe radiator can be estimated using the same equations as CR (see Eq. 2.4) though an additional attenuation effect K must be taken into account where

$$K = \exp\left(-\frac{4\pi b}{\gamma\beta\lambda}\right), \tag{2.9}$$

b is the distance between the particle and the radiator, and λ is the wavelength of the radiation [47]. The attenuation factor is larger at shorter wavelengths, whereas the pure CR photon yield is larger at shorter wavelengths. Combining the CR photon yield (Eq. 2.4) with the dielectric pipe attenuation factor gives

$$\frac{\mathrm{d}^2 N_\gamma}{\mathrm{d}\lambda \mathrm{d}x} = z^2 2\pi\alpha \left(1 - \frac{1}{\beta^2 n^2(\lambda)}\right)\left(\frac{1}{\lambda^2}\right) \exp\left(-\frac{4\pi b}{\gamma\beta\lambda}\right), \tag{2.10}$$

furthermore integrating Eq. 2.10 over the radiator length yields

$$\frac{\mathrm{d}N_\gamma}{\mathrm{d}\lambda} = z^2 2\pi\alpha l\left(1 - \frac{1}{\beta^2 n^2(\lambda)}\right)\left(\frac{1}{\lambda^2}\right)\exp\left(-\frac{4\pi b}{\gamma\beta\lambda}\right), \tag{2.11}$$

using the same notation as before.

Figure 2.6 shows the ChDR spectrum for a 3 GeV electron travelling through the centre of a 10 mm long dielectric pipe with a fixed index of refraction of 1.45, chosen as this is an average refractive index of fused silica for the wavelength range [48]. Each plot shows the spectrum of ChDR emitted from a pipe of different radius, apart from the dashed blue line that shows CR emitted from a particle travelling through the medium.

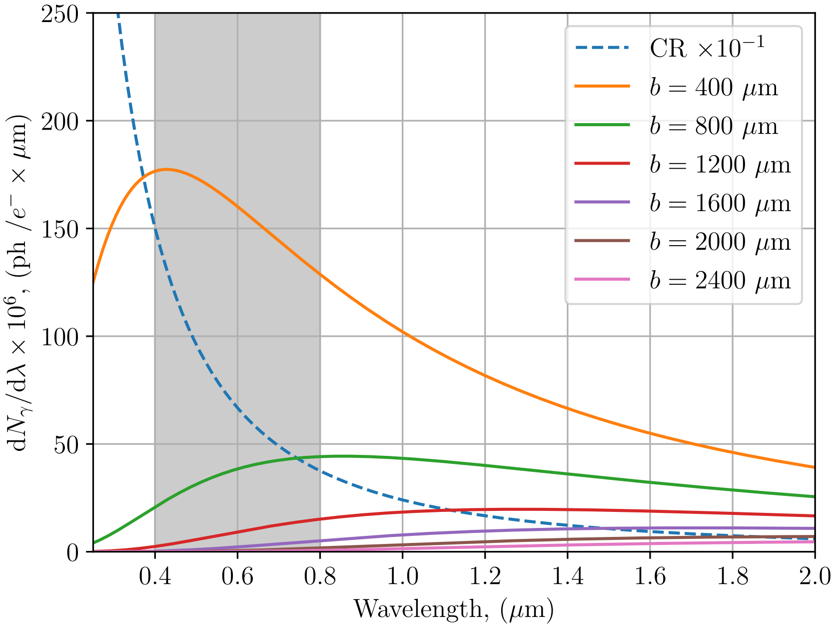

Figure 2.6: Cherenkov Diffraction Radiation Spectrum Generated by a 3 GeV electron moving through the centre of 10 mm long fused silica dielectric pipes with different radii, where the shaded area represents the visible wavelengths. The dashed blue line is the same one produced in Fig. 2.3 scaled down by a factor of 10 for better visual representation.

The graph in Fig. 2.6 show that increasing the impact parameter reduces the ChDR photon yield significantly and changes the spectral distribution. The peak of the ChDR spectrum shifts towards longer wavelengths with a larger impact parameter, whereas an increase in the beam energy has an opposite but scaled effect.

The beam pipe radius is commonly reduced in next generation synchrotron light sources; the typical size for these accelerators will be approximately 10 mm depending on location [4]. For Diamond-II the proposed beam energy is 3.5 GeV. This means a centralised beam would produce a ChDR energy yield at long wavelengths approaching 10 µm. Assuming a large

BPM working area of up to ±5 mm, the wavelengths of peak ChDR emission will likely shift into the IR region for impact parameters between 5 and 15 mm. For optimal ChDR detection, the optical system should be sensitive to the peak emission wavelengths for the operational impact parameter range, in the case of Diamond-II these are all expected to be in the IR region.

Modelling a dielectric pipe as a ChDR radiator makes the calculations simpler as the entire transverse field is radially symmetric. For a ChDR radiator with geometry similar to that of a beam pipe, coupling the ChDR out to a detector system could prove to be very complex.

2.4 Cherenkov Diffraction Radiation Radiator Geometries

A ChDR radiator or pickup can be manufactured into different shapes and geometries that will influence how much radiation will be generated and how that radiation is propagated into a detection system. Regardless of the geometry, a longer radiator will produce a higher photon yield as the charged particle will polarise more atoms of the radiator, leading to the relationship

$$N_\gamma \propto l, \tag{2.12}$$

where N_γ is the photon yield, and l is the length of the radiator side that runs parallel with the particle trajectory [26]. While the photon yield may increase linearly, there may be changes in the angular distribution and the ability to couple the light out of a longer radiator that will not scale in the same way.

2.4.1 Prismatic Cherenkov Diffraction Radiation Radiator

A prismatic radiator is used to direct the extraction of the radiation out of the radiator. Figure 2.7 shows the schematic of a prismatic radiator that is used to generate ChDR and DR [30].

CR is generated at an angle that is distinctively different to the beam trajectory (see Eq. 2.2). The extracted radiation can be directed using a prismatic radiator. Once the ChDR reaches the extraction surface of the prism it will be emitted at a refracted angle given by Snell's law [49]. Knowing the interfaces refractive indexes and the incident angle between the ChDR

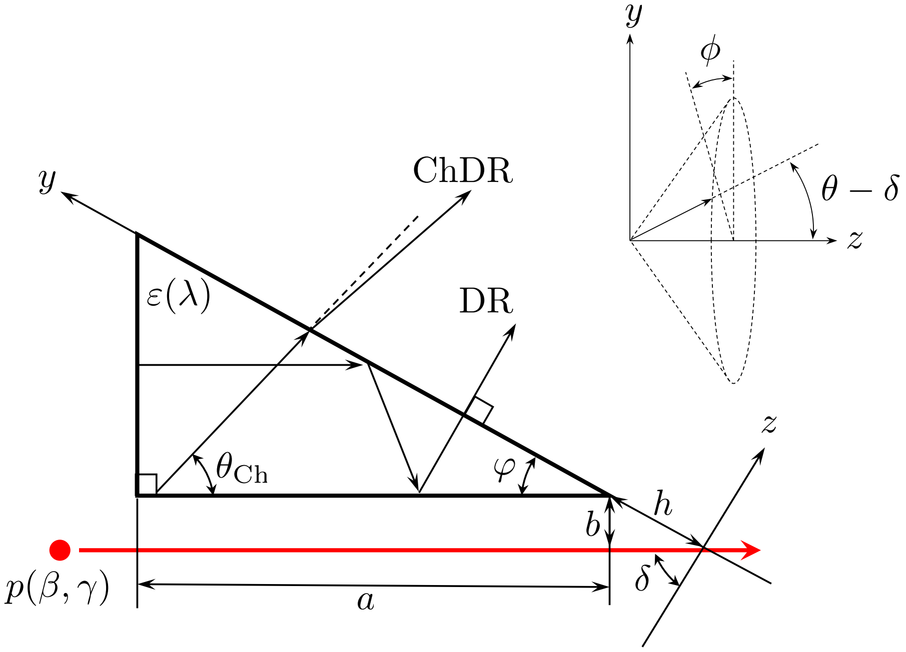

Figure 2.7: Prismatic ChDR Radiator where γ is the Lorentz factor, β is the velocity of the particle relative to the vacuum velocity of light, λ is the wavelength of the radiation, $\varepsilon(\lambda)$ is the wavelength dependent permittivity of the medium that the prism is constructed from, θ_{Ch} is the Cherenkov angle, a is the length of the surface in the direction parallel with the electron trajectory, φ is the vertex angle of the prism, δ is $(90° - \varphi)$, b is the impact parameter, h is the angled impact parameter (where $b = h\cos(\delta)$), and ϕ and θ are respectively the azimuthal and polar angles of the emitted radiation [30].

and extraction surface, the emission angle can be calculated. By placing a detection system at the ChDR extraction angle the radiation is detected and measured.

In order to detect all of the emitted ChDR for a prismatic radiator either a detector with the same length as the emission surface would need to be used, or an optical system with a wide angular acceptance that would focus the radiation into a detector.

When a charged particle passes the upstream side of the prismatic radiator (see Fig. 2.7) DR will be generated, as well as ChDR [29,30]. Extensive work has been done in [30] to give the equations for the far field angular distribution of the ChDR and DR generated from a prismatic radiator, given by

$$\frac{\mathrm{d}^2W}{\mathrm{d}\lambda\mathrm{d}\Omega} = \frac{\mathrm{d}^2W_1}{\mathrm{d}\lambda\mathrm{d}\Omega} + \frac{\mathrm{d}^2W_2}{\mathrm{d}\lambda\mathrm{d}\Omega}, \tag{2.13}$$

where $\mathrm{d}^2W_1/\mathrm{d}\lambda\mathrm{d}\Omega$ denotes the vertical polarisation component of the emitted angular distribution, and $\mathrm{d}^2W_2/\mathrm{d}\lambda\mathrm{d}\Omega$ the horizontal polarisation component. The polarisation components are given by Eq. 2.14, 2.15 and 2.16, where $\hbar$ denotes the reduced Planck constant, α is the fine structure constant, and the notation from Fig. 2.7 has been used [30]. Figure 2.8 shows an example angular distribution for the different polarisations.

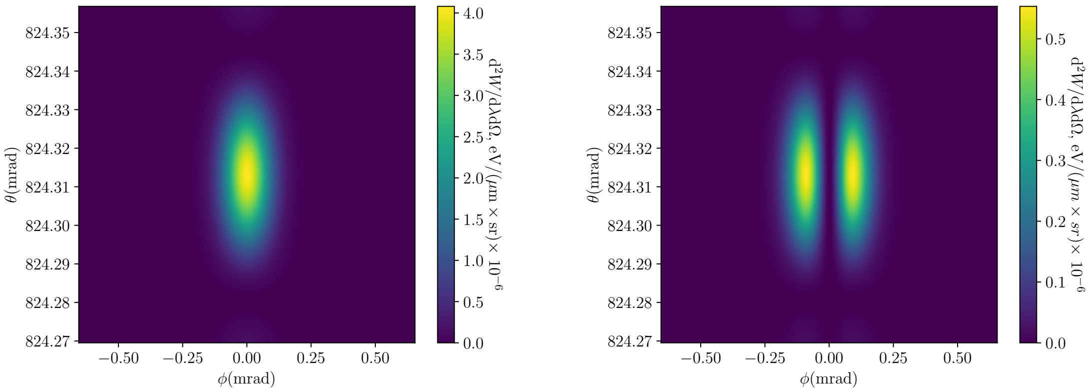

(a) Vertical polarisation.

(b) Horizontal polarisation.

Figure 2.8: Example single particle PCA angular distributions from a prismatic radiator a 0.4 µm wavelength, and a 5 mm impact parameter. Produced using coded simulations described in detail in Chap. 5.

$$\begin{aligned}
\frac{\mathrm{d}^2W_1}{\mathrm{d}\lambda\mathrm{d}\Omega} &= \frac{\alpha\hbar c\beta^2\cos^2(\theta-\delta)}{2\pi^2\lambda^2K^2|P|^2}\left|\frac{\varepsilon(\lambda)-1}{\varepsilon(\lambda)}\right|^2\times\Bigg|1-\exp\left[-ia\frac{2\pi}{\beta\lambda}(P+\Sigma\cdot\cot(\varphi))\sin(\varphi)\right]\\
&-\frac{P\exp\left[i\frac{2\pi}{\beta\lambda}\Sigma\cdot a\cdot\cos(\varphi)\right]}{P+\Sigma\cdot\cot(\varphi)}+\frac{P^2+\Sigma^2\cdot\cot^2(\varphi)}{P^2-\Sigma^2\cdot\cot^2(\varphi)}\exp\left[-ia\frac{2\pi}{\beta\lambda}P\cdot\sin(\varphi)\right]\\
&-\frac{\Sigma\cdot\cot(\varphi)\exp\left[-i\frac{2\pi}{\beta\lambda}\Sigma\cdot a\cdot\cos(\varphi)\right]}{P-\Sigma\cdot\cot(\varphi)}\Bigg|^2\times\\
&\frac{\exp\left[-\frac{4\pi}{\gamma\beta\lambda}(h+a\cdot\cos(\varphi))K\cos(\delta)\right]}{1-\beta^2\cos^2(\theta-\delta)+\beta^2\sin^2(\delta)(1-\sin^2(\theta-\delta)\sin^2(\phi))+2\beta\sin(\delta)\sin(\theta-\delta)\cos(\phi)}\\
&\times\left|\frac{\varepsilon(\lambda)}{\varepsilon(\lambda)\cos(\theta-\delta)+U}\right|^2|\cos(\delta)(\gamma^{-1}\sin(\theta-\delta)-iKU\cos(\phi))+\\
&\sin(\delta)(iK\sin(\theta-\delta)+\gamma^{-1}U\cos(\phi))-\gamma\beta U\sin(\theta-\delta)\sin^2(\phi)|^2,
\end{aligned}\tag{2.14}$$

$$
\begin{aligned}
&\frac{\mathrm{d}^2W_2}{\mathrm{d}\lambda \mathrm{d}\Omega} = \frac{\alpha\hbar c\beta^2\cos^2(\theta-\delta)}{2\pi^2\lambda^2K^2|P|^2}\left|\frac{\varepsilon(\lambda)-1}{\varepsilon(\lambda)}\right|^2\gamma^2\sin^2(\phi)\left|\frac{\sqrt{\varepsilon(\lambda)}}{\cos(\theta-\delta)+U}\right|^2(\sin^2(\theta-\delta)+|U|^2) \\
&\times\left|1-\exp\left[-ia\frac{2\pi}{\beta\lambda}(P+\Sigma\cdot\cot(\varphi))\sin(\varphi)\right]-\frac{P\exp\left[i\frac{2\pi}{\beta\lambda}\Sigma\cdot a\cdot\cos(\varphi)\right]}{P+\Sigma\cdot\cot(\varphi)}+\right. \\
&\left.\frac{P^2+\Sigma^2\cdot\cot^2(\varphi)}{P^2-\Sigma^2\cdot\cot^2(\varphi)}\exp\left[-ia\frac{2\pi}{\beta\lambda}P\cdot\sin(\varphi)\right]-\frac{\Sigma\cdot\cot(\varphi)\exp\left[-i\frac{2\pi}{\beta\lambda}\Sigma\cdot a\cdot\cos(\varphi)\right]}{P-\Sigma\cdot\cot(\varphi)}\right|^2\times \\
&\frac{\exp\left[-\frac{4\pi}{\gamma\beta\lambda}(h+a\cdot\cos(\varphi))K\cos(\delta)\right]}{1-\beta^2\cos^2(\theta-\delta)+\beta^2\sin^2(\delta)(1-\sin^2(\theta-\delta)\sin^2(\phi))+2\beta\sin(\delta)\sin(\theta-\delta)\cos(\phi)} \\
&\times\left[1-\beta^2\cos^2(\theta-\delta)+2\beta\gamma^{-2}\sin(\theta-\delta)\cos(\phi)-\gamma^{-2}\sin^2(\delta)(K^2-\gamma^{-2})\right],
\end{aligned}
\tag{2.15}
$$

$$
\begin{aligned}
U &= \sqrt{\varepsilon(\lambda)-\sin^2(\theta-\delta)}, \\
P &= \cos(\delta)-\beta U+i\gamma^{-1}K\sin(\delta), \\
\Sigma &= \sin(\delta)+\beta\sin(\theta-\delta)\cos(\phi)-i\gamma^{-1}K\cos(\delta), \\
K &= \sqrt{1+(\gamma\beta\sin(\theta-\delta)\sin(\phi))^2}.
\end{aligned}
\tag{2.16}
$$

The same PR assumptions detailed in Sec. 2.1 have been made for this model. In order to simplify Eq. 2.14 and 2.15 the radiator is assumed to be of infinite length in the horizontal transverse plane. This assumption is of critical importance when the radiator height is smaller than or comparable to the effective electron radius (see Eq. 2.8) as the radiator will not intercept the portion of the field that this model assumes. Another assumption made in this model is that the length of the radiator in the longitudinal plane l is much larger than the emitted radiation wavelength in the order of $l > 10\lambda$.

For the purpose of using a radiator as a pickup for a BPM a single intensity measurement is expected. Multiple radiators can then be used in classical BPM configurations discussed in Sec. 1.3. In order to obtain an intensity measurement from each pick-up the emitted radiation is propagated to a photodetector. The intensity read by the detector is proportional to the energy of the emitted radiation. This can be simulated by integrating Eq. 2.14 and 2.15 with the solid angle and wavelength intervals $\Delta\Omega$, and $\Delta\lambda$ respectively. This yields the energy of emitted radiation ΔW as

$$
\Delta W = \int_{\Delta\lambda}\mathrm{d}\Omega, \int_{\Delta\Omega}\frac{\mathrm{d}^2W}{\mathrm{d}\lambda\mathrm{d}\Omega}\mathrm{d}\lambda, \tag{2.17}
$$

where dW is the energy emitted per unit of wavelength, dλ, per unit of solid angle, dΩ. The solid angle component is given by

$$\mathrm{d}\Omega = \sin(\theta)\mathrm{d}\theta\mathrm{d}\phi, \tag{2.18}$$

where θ is the polar angle of the angular distribution, and ϕ the azimuthal angle. By producing a series of angular distributions and integrating each one, parameter dependencies can be calculated. Parameter dependency scans produced with this method will produce impact parameter scans where the impact parameter is varied, or spectral scans where the wavelength is varied. Simulations using this technique have been produced in Chap. 5.

2.4.2 Accumulating Cherenkov Diffraction Radiation Radiator

For a prismatic radiator the extraction angle can be well defined and a detection system easily setup. A potential downside of this radiator design is that the ChDR photons will be spread out along the prism exit face meaning to capture the full emission a large detector or optical system must be used.

Figure 2.9 shows the schematic of a ChDR accumulation radiator. When a charged particle passes the accumulation radiator if the Cherenkov condition (see Eq. 2.1) is met, ChDR will be generated inside the radiator at the Cherenkov angle. The accumulation radiator is designed such that the ChDR generated inside will undergo Total Internal Reflection (TIR) until the ChDR reaches the reflective surface for the desired extraction wavelengths. The radiator is designed this way by using a material with an acceptable refractive index and calculating the vertex angle φ for a specific extraction angle. Using an accumulation radiator the photon yield should scale with the length of the radiator, allowing for a more sensitive detector by simply increasing the length (see Eq. 2.12). The exact vertex angle is selected such that the accumulated ChDR will exit the target orthogonal to the particle trajectory, simplifying the detection system and removing background SR.

The initial ChDR emission angle inside the radiator is still defined as the Cherenkov angle Eq. 2.2. The final emission angle is then dictated by the Cherenkov angle and radiator vertex angle. The assumption is made that as Eq. 2.14, 2.15 and 2.16 are working in the angular domain, the angular distributions calculated from these equations will be different than the prismatic target, however the energy loss due to ChDR can still be calculated and compared with experimental results.

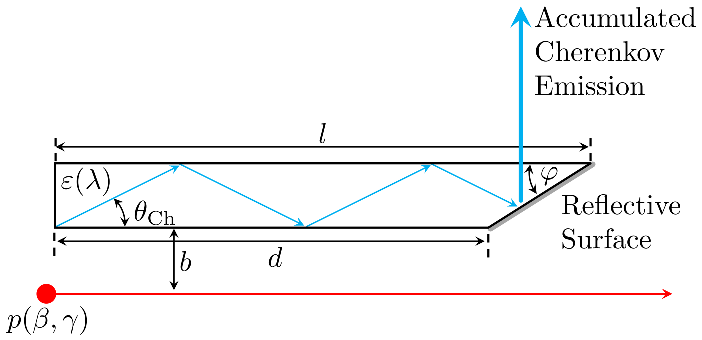

Figure 2.9: Accumulating ChDR Radiator.

CHAPTER 3

EXPERIMENTAL SETUP

Experiments for ChDR beam diagnostics have been carried out as part of a collaboration involving several institutes including the John Adams Institute (JAI), European Organization for Nuclear Research (CERN), and Tomsk Polytechnic University. Experiments have been carried out at accelerator facilities including the Cornell Electron Storage Ring (CESR), Accelerator Test Facility 2 (ATF2), Compact Linear Accelerator for Research and Applications (CLARA), CERN Linear Electron Accelerator for Research (CLEAR) and Diamond Light Source [26]. Each facility is able to use the specific parameters of their accelerator to test different properties of ChDR radiators. The tests performed at ATF2 are examining the use of ChDR radiators as a beam size monitor. ATF2 lends itself to this as the σ_x and σ_y beam sizes can be reduced down to microns [50]. The beam sizes in the Diamond BTS are large in comparison with horizontal beam size σ_x of approximately 1.5 mm, and vertical beam size σ_y of approximately 0.5 mm. Nevertheless, the Diamond BTS lends itself to testing the beam position dependence of ChDR radiators. Other accelerators such as CLARA and CLEAR have short bunch lengths in comparison to Diamond, lending themselves to experiments that examine the coherent ChDR emission used for longitudinal bunch length and transverse beam position measurements [50].

3.1 Diamond Beam Test Stand Setup

The BTS at Diamond is located in the transfer line between the Booster synchrotron and the storage ring of the accelerator chain, giving the use of a 3 GeV electron beam for accelerator research. In order to test accelerator components with the BTS the beam conditions must be well defined for accurate cross referencing. The vacuum vessel string has been modified with the installation of the ChDR monitor. The instruments installed on the BTS have been recommissioned as part of this project.

Figure 3.1 shows the monitors installed onto the modified BTS, including three OTR monitors, an IBPM, and the ChDR experiment. The OTR monitors are used to obtain a transverse beam profile, and to measure relative transverse beam position movements. The IBPM is used to measure absolute transverse beam position and intensity.

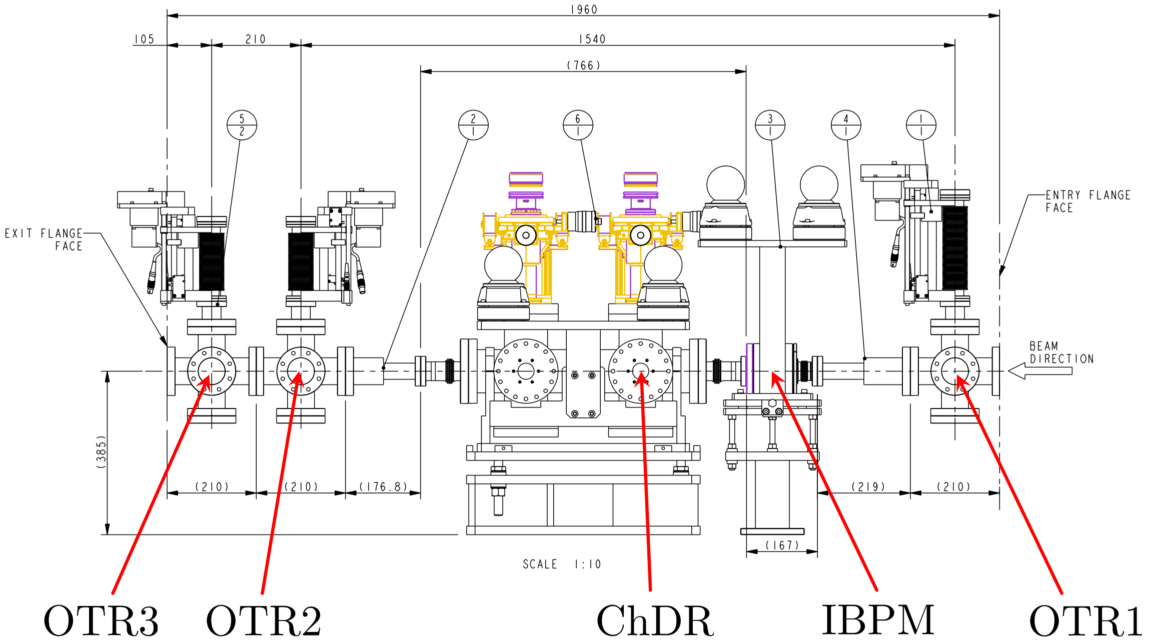

Figure 3.1: Schematic of the BTS.

Figure 3.2 shows the BTS with the upstream end on the right of the photo. Under the BTS is an optical table where the OTR and ChDR optical systems are installed. Cables have been laid from the BTS to a Control Instrument Area (CIA) where electronic devices can be accessed during accelerator operations. Inside the CIA is an Input/Output Controller (IOC) device that provides triggers to the BTS. These triggers can be configured using Experimental Physics and Industrial Control System (EPICS) [51]. Also installed on the BTS is a GEOBRICK motor controller that connects directly to stages on each of the OTR and ChDR monitors to insert and remove them from the beam path.

The Diamond electron gun and Linac has two extraction modes: single bunch and multibunch train. Under either mode the extracted electrons are injected into the Booster synchrotron where the bunch structure is preserved for Booster extractions. Under multibunch train mode the Booster synchrotron will extract a train of up to 120 bunches to the storage ring through the BTS. For single bunch mode a single bunch is extracted. Under a normal Diamond user

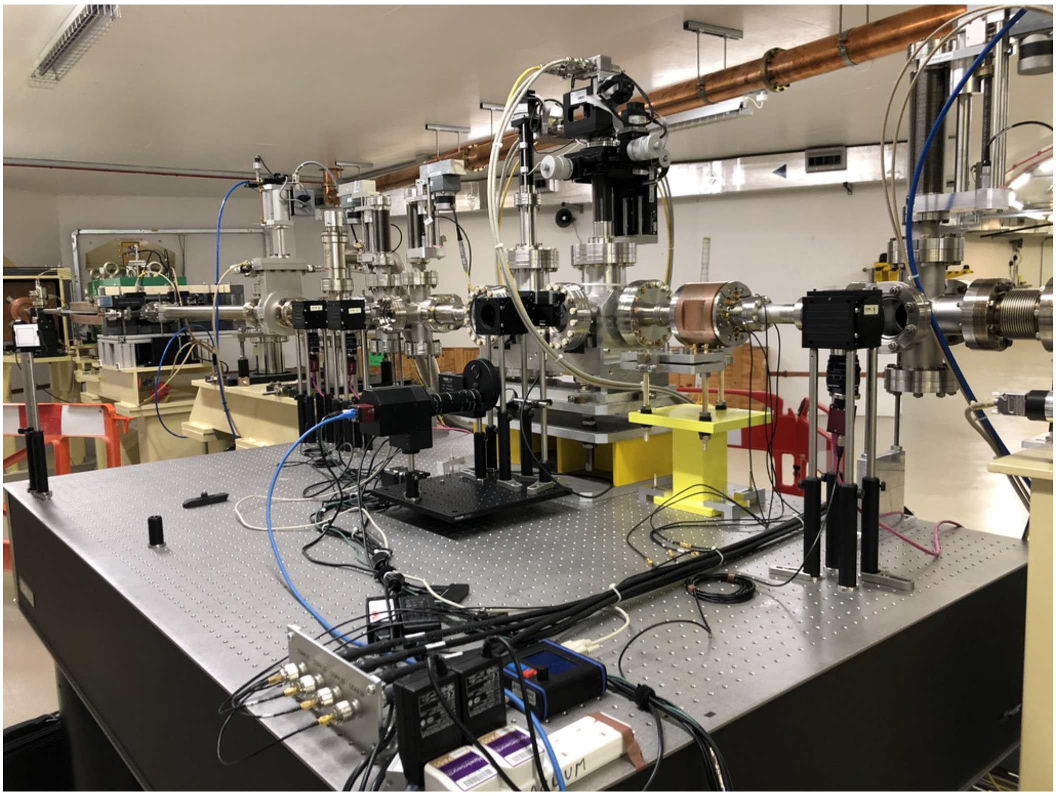

Figure 3.2: Photo of the BTS.

run, multibunch train mode is used when initially filling up the storage ring. Single bunch mode is then used to top-up selected bunches due to the Touschek lifetime of the particles in the accelerator [4].

Table 3.1 shows the range of BTS beam parameters that are used during standard Diamond operations. There is scope to adjust the BTS parameters outside of these values if required. The BTS beam sizes are altered by adjusting an upstream quadrupole magnet, and the beam position is altered by changing configuration of upstream corrector magnets. Diamond staff have provided a number of codes in order to simplify the process of altering the beam position or size through the BTS. These codes have also been commissioned as part of this research project.

3.1.1 Inductive Beam Position Monitor

The single IBPM on the BTS is there to acquire absolute beam position and intensity. Details of an IBPM can be found in Sec. 1.3.4. The four pickups of the IBPM are oriented orthogonally to the beam meaning Eq. 1.11 and 1.12 are used to deduce the beam position. Initial values provided give the geometrical scaling factor a the value of $-15.397\,\text{mm}$.

Standard BTS Parameter	Value
Beam Energy	3 GeV
Horizontal Beam Size σ_x	$\approx$ 1.5 mm
Vertical Beam Size σ_y	$\approx$ 0.5 mm
Extraction Rate	Up to 5 Hz
Max Bunch Charge (single bunch extraction)	0.2 nC
Min Bunch Charge (single bunch extraction)	0.02 nC
Max Charge per 120 Bunch Train (train extraction)	1.3 nC
Bunch Spacing (train extraction)	2 ns
Bunch Length	$\approx$ 29.8 mm

Table 3.1: Standard working parameters on the Diamond BTS [4, 52, 53].

As the beam movement is outside of the centralised linear region of the IBPM, a third order polynomial is used to correct for the non-linearities. Simulations performed at CERN have shown that the IBPM on the BTS is corrected using

$$x_{\text{mod}} = -(5.026x_{\text{raw}}^3 - 1.601x_{\text{raw}}y_{\text{raw}}^2 + 15.352x_{\text{raw}})[\text{mm}], \tag{3.1}$$

$$y_{\text{mod}} = -(5.026y_{\text{raw}}^3 - 1.601y_{\text{raw}}x_{\text{raw}}^2 + 15.352y_{\text{raw}})[\text{mm}], \tag{3.2}$$

where x_{mod}, y_{mod}, are the corrected horizontal and vertical beam position, and x_{raw}, y_{raw}, are given from the relationships

$$x_{\text{raw}} = \frac{V_r - V_l}{V_r + V_l}, \tag{3.3}$$

$$y_{\text{raw}} = \frac{V_t - V_b}{V_t + V_b}, \tag{3.4}$$

where V denotes the signal measured from the pickup and the subscripts l, r, t, b denote the left, right, top, and bottom pickups respectively. Note that the middle component of Eq. 3.1 and 3.2 features both x_{raw} and y_{raw} parts, this is to account for the x dependence on the y pickups and vice versa.

Figure 3.3 is created by taking equally spaced values of x_{raw} and y_{raw} and processing them through the two correction methods. The red crosses are produced by using the linear scaling factor of −15.397 mm, whereas the blue dots use Eq. 3.1 and 3.2. Both the scalar and polynomial methods are closely matched over the range of ±5 mm from the $(0, 0)$ centre in both planes. Outside of this there is a divergence between the two methods where the polynomial is closer to the real position as it corrects for non-linearities in the x_{raw} and y_{raw} measurements.

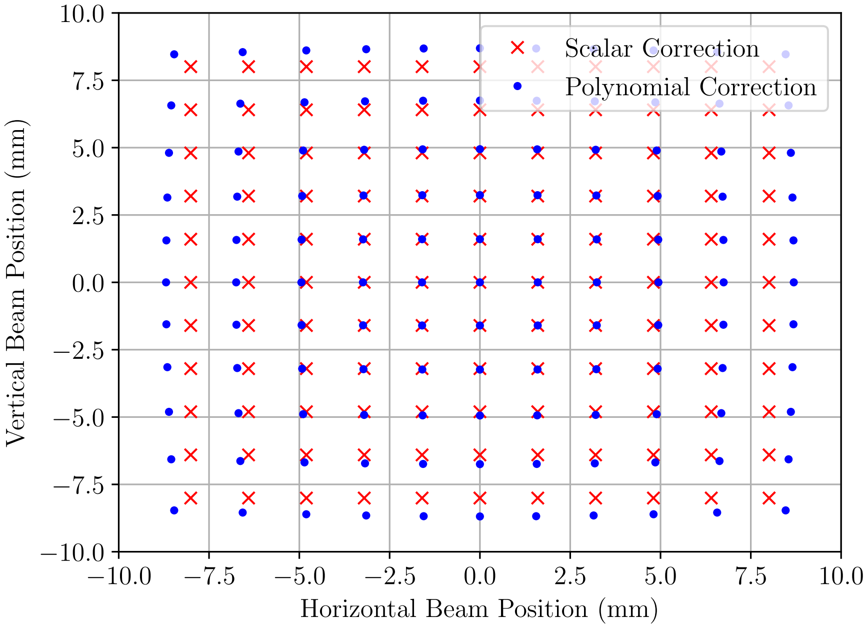

Figure 3.3: Comparison between IBPM scalar and polynomial correction methods.

When calculating the bunch charge Eq. 1.15 is used, where the scaling factor, k_Q, has a value of -0.404 C/Vs. As given in Table. 3.1 the bunch length is approximately 29.8 mm. In order to accurately capture the bunch information, the data acquisition system needs to be able to take multiple samples across the bunch. The IBPM pickup produces a response that is much longer the bunch length. Experimental testing shows that the transient signal induced on the IBPM pickup by the bunch lasts for approximately 2 ns. The Agilent DSA91304A used to acquire the IBPM signals has a maximum sample rate of 40 GS/s giving a sampling time of 0.025 ns [54]. Given the bunch length and Agilent DSA91304A sampling time an adequate number of approximately 80 samples are taken across each induced signal.

The DSA91304A is set to save every waveform from all four pickups each time it receives a trigger. The EPICS IOC provides a trigger synchronised with the bunch extraction. The waveforms are then post processed after the experiments in order to obtain the transverse beam position and beam intensity. During operations the beam current injected into the BTS is monitored using an upstream Integrating Current Transformer (ICT).

3.1.2 Optical Transition Radiation Monitors

There are three OTR monitors installed onto the BTS. Each OTR monitor setup features a screen holder fitted with two screens: an aluminium OTR screen and a Yttrium Aluminium

Garnet (YAG) scintillating screen. A motor system is attached to the screen holder in order to move either of the screens vertically in and out of the beam path. Two screens are fitted as a YAG screen produces a large photon yield at a wide angle but has low resolution defined by the thickness of the screen, whereas the emission from an OTR screen is more directional with a lower photon yield and has higher resolution [24].

Figure 3.4 shows the schematic of the OTR system. As the beam passes through the screen the beam profile can then be acquired by the optical system that is imaging the screen through the vacuum view port. The screen is oriented at 45° because the backwards OTR propagates in the direction of specular reflection.

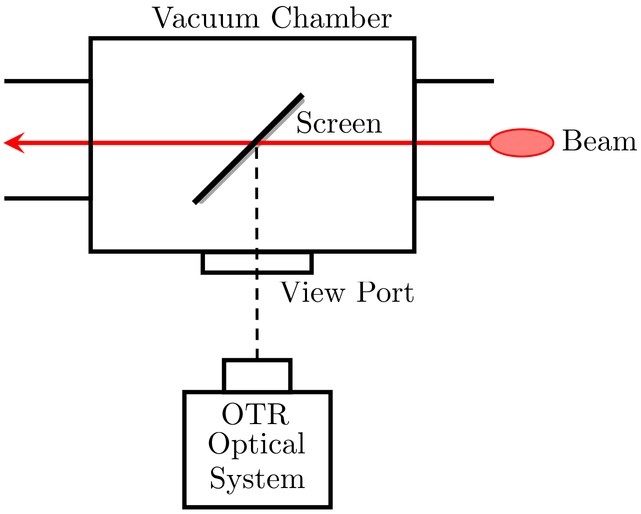

Figure 3.4: Top-down schematic of OTR beam profile monitoring system.

To image the beam profile from the OTR or YAG screens, an optical system is used (see Fig. 3.5). The optical system uses an Allied Vision Mako-319B camera, that is attached to a Scheimpflug adaptor in order to maintain the focus across the entire OTR screen as it has a limited depth of field [55]. A Schneider 2,8/50 Makro compound lens is used to give the system a magnification of 0.19, with a pixel size of 3.45 µm × 3.45 µm. The camera, adaptors and lens system is mounted to mirror box (see Fig. 3.5) and positioned in front of the vacuum port window allowing for a line of sight between the camera and screen.

Figure 3.6 shows a reference image of the OTR screen taken with the optical system. When the beam passes through the OTR screen, the TR will be emitted both forwards with the beam trajectory, and backwards where it is reflected off the OTR screen towards the optical system [24]. The TR captured by the optical system can then be analysed in order to obtain the transverse beam profile. The same optical system and analysis is used for the YAG and OTR screens, so the optical system remains stationary, and only the screen holder will move.

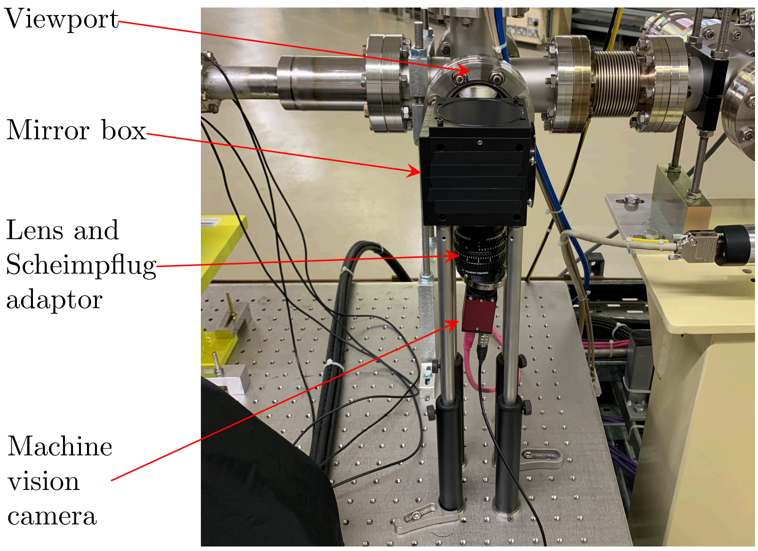

Figure 3.5: OTR optical system.

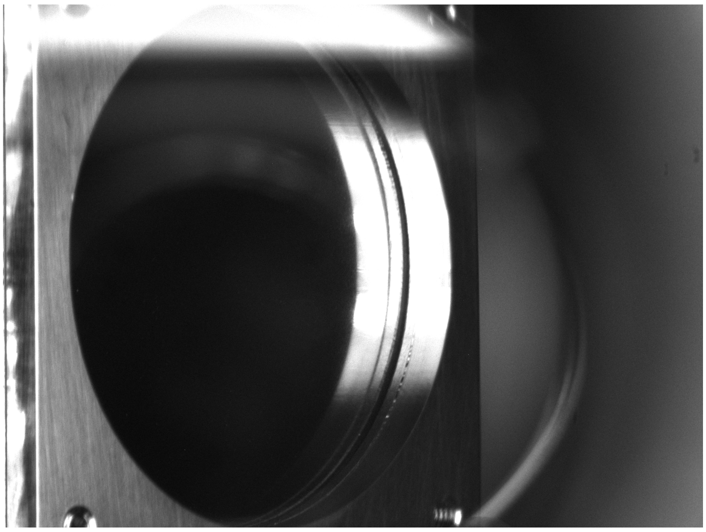

Figure 3.6: OTR reference image.

In order to analyse the beam profile, a 2D Guassian distribution G is fit to the image taken by the OTR optical system. A 2D Gaussian distribution is represented as a multiplication of two 1D Gaussian distributions resulting in

$$G(x,y) = A\exp\left[-\left(\frac{(x-x_0)^2}{2\sigma_x^2}+\frac{(y-y_0)^2}{2\sigma_y^2}\right)\right]+C, \tag{3.5}$$

where x and y are the horizontal and vertical co-ordinates on the image, A is the linear scaling coefficient, C is the constant offset, σ_x, σ_y are the horizontal and vertical standard deviations of the distribution, and x_0, and y_0, are respectively, the centre horizontal and vertical coordinates of the distribution. As the distributions measured on the OTR monitors may be tilted this creates a blending of the x and y components that needs to be accounted for. A more general 2D Gaussian distribution is given by

$$G(x,y) = A\exp\left[-(a(x-x_0)^2 + 2b(x-x_0)(y-y_0) + c(y-y_0)^2)\right] + C, \tag{3.6}$$

where the coefficients, a, b, c are given by

$$\begin{aligned} a &= \frac{\cos^2(\theta)}{2\sigma_x^2} + \frac{\sin^2(\theta)}{2\sigma_y^2}, \\ b &= \frac{\sin(2\theta)}{4\sigma_y^2} - \frac{\sin(2\theta)}{4\sigma_x^2}, \\ c &= \frac{\sin^2(\theta)}{2\sigma_x^2} + \frac{\cos^2(\theta)}{2\sigma_y^2}, \end{aligned} \tag{3.7}$$

where θ is the tilt of the distribution [56]. Note that if the tilt is zero the coefficients simplify and Eq. 3.6 becomes Eq. 3.5.

By fitting this distribution to each beam image, the beam size, centroid, and tilt are obtained.

3.1.3 Triggering and Synchronisation

Different monitors send and save their data to different locations, such as, on a computer, over EPICS, or on the monitor itself. Data from all of the monitors are compared on a shot-by-shot basis or a number of data shots for a specific setup are averaged then compared.

Tying all of the monitors together is the IOC triggers. The IOC waits for a Booster extraction event before sending a separate 5 V TTL trigger to each monitor. A delay, from when the IOC reads the event and when the trigger is sent, can then be set for each trigger, as well as the trigger pulse width, so that all triggers can be configured independently. Configuring each trigger independently ensures each monitor will capture data for the same bunch so the response time of the monitor can be accounted for. As all of the monitors are triggered together, the extraction rate, or trigger gating can be modified ensuring that data can be compared on a shot-by-shot basis.

3.2 Cherenkov Diffraction Radiation Experimental Setup

As stated in Chap. 2, ChDR is emitted when a charged particle moves close to but not through a radiator at a velocity faster than the phase velocity of light in that medium. An experimental setup has been built on the Diamond BTS in order to examine incoherent ChDR emission. This experimental setup features a ChDR radiator, an optical detection system, and motor systems needed to manipulate and control the setup. Multiple optical systems are discussed in this chapter as the optical system has gone under several revisions over the course of the project. The original optical system was used to image the ChDR radiator with an off the shelf compound lens. Updated optical systems were used to image the radiator and measure the ChDR angular distribution. Finally a Photomultiplier Tube (PMT) detection system was installed to increase the photon sensitivity.

3.2.1 Radiator and Target Holder

The radiator used for the initial ChDR experiments is a CVD diamond accumulation radiator. The mechanical schematic for the radiator can be seen in Fig. 3.7.

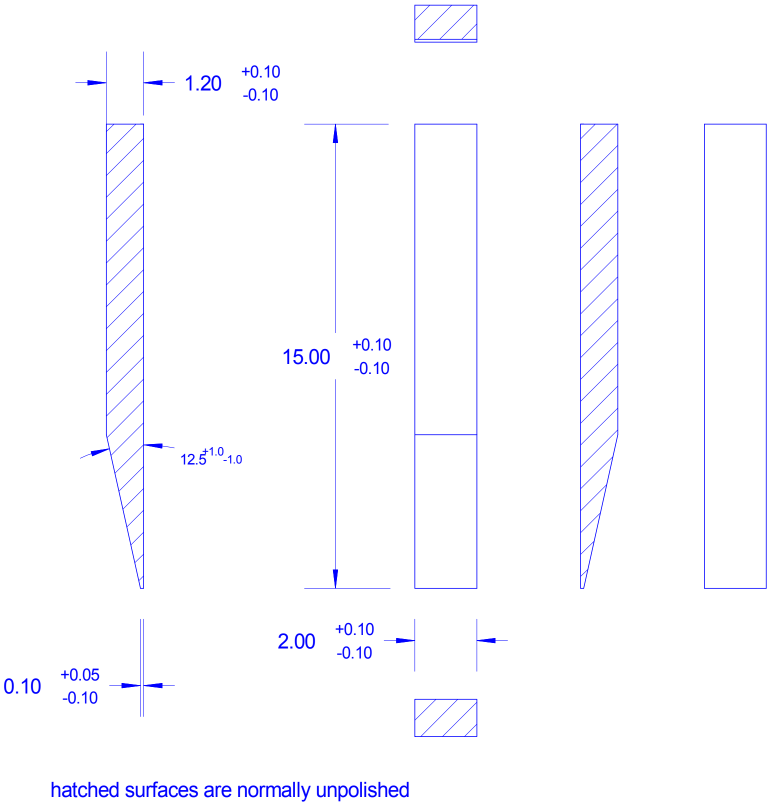

Figure 3.7: Mechanical drawing of CVD diamond ChDR radiator installed on the BTS [57].

The radiator installed was originally specified for experiments at ATF2 and as such the radiator is not optimised for experiments at the Diamond BTS. An ideal radiator would have a vertical height that is much larger than both; the effective electric field radius (see Eq. 2.8), and the vertical beam height. For a 3 GeV electron and a wavelength range between 400 and 600 nm the effective electric field radius is approximately between 0.4 and 0.6 mm. Ideally the radiator height would be at least ten times the effective electric field radius. Additionally the σ_y vertical beam size is approximately 0.5 mm, in order to maximise the beam coverage the radiator vertical height should be approximately ten times larger than this. Taking these effects into account the radiator height should ideally be 10 mm or longer. Given that the radiator height is 2 mm this will likely have an effect on the experimental results.

The target holder is capable of holding two ChDR radiators on opposite sides of the beam in the horizontal plane and an OTR screen. In order to move the targets in and out of the beam path the holder is connected to a vertical vacuum actuator. The OTR screen and ChDR radiators are at different vertical positions so only one can be inserted at a time. The OTR screen is used to ensure that the beam is passing through the monitor at the transverse location where ChDR should be emitted. The height of the monitor can then be altered to move the OTR screen out of the beam path and move in the ChDR radiator.

Figure 3.8 shows a Computer Aided Design (CAD) drawing of the holder fitted with the nearside and farside ChDR targets, and the OTR screen. The target holder is mounted to a rotary stage enabling the alignment of the different targets with the optical system. For the experiment on the BTS the nearside ChDR radiator is not installed. In addition to this the farside ChDR radiator installed on the BTS has the opposite orientation to Fig. 3.8, where Fig. 3.9 shows the correct orientation.

The centre of rotation for the holder is set for the centre of the black vertical shaft seen in Fig. 3.8. This does not align with the centre of rotation for either of the ChDR radiators or the OTR screen. As the centre of rotation is not the same for all radiators and screens the optimal rotation angle used for ChDR measurements will not be the same as the angle used for OTR measurements.

Figure 3.9 shows a top-down view schematic of the ChDR system where the Farside ChDR radiator and OTR screen can be seen. A sapphire viewport is used to couple the radiation out of the accelerator vacuum vessel into the optical system.

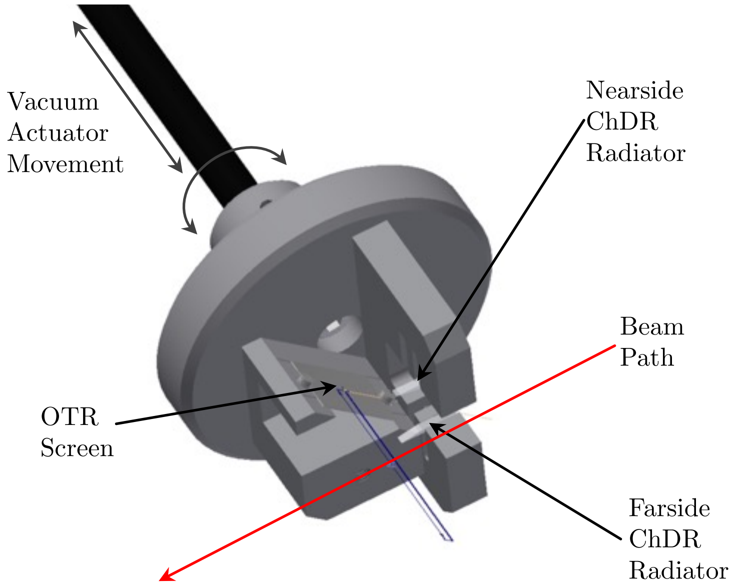

Figure 3.8: CAD drawing of the ChDR target holder.

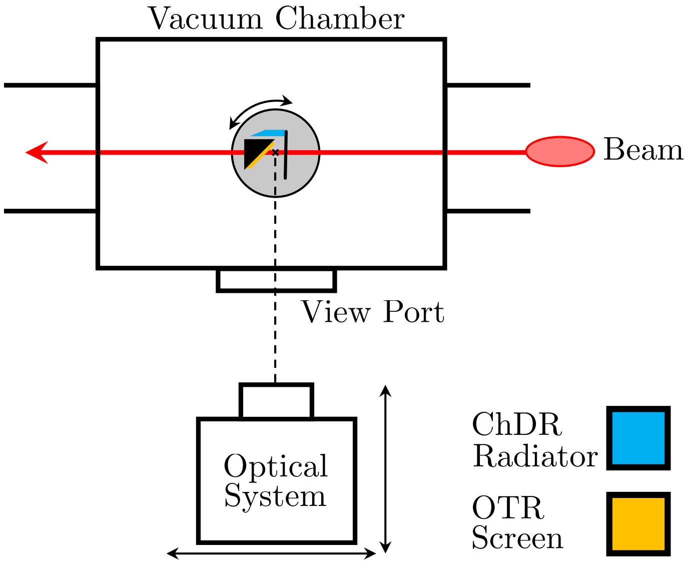

Figure 3.9: Top-down schematic of ChDR experimental system.

3.2.2 Preliminary Cherenkov Diffraction Radiation Optical system

Initial experiments were performed by imaging the ChDR target and analysing images taken. These experiments were performed before detailed simulations relating to the angular distribution of the ChDR emission had been performed. The optical system used for the imaging setup is shown in Fig. 3.10. A pair of mirrors is used as a periscope to vertically lower the ChDR emission. This is done to reduce the ionising radiation the electronic components in the optical system will be subjected to by setting their height different than that of the electron beam. The other components in the optical system are a filter wheel, loaded with a pair of band pass filters to filter the ChDR emission, a Schneider 5.6/100 lens with a 60 mm extension tube, and a ProxiKit Package camera from ProxiVision [58].

The ProxiVision camera used for these experiments was chosen as it is a left over component from experiments performed in [25]. As it was a left over component it was not chosen as an optimal camera to use for this thesis. The bandpass filters installed in the filter wheel are Thorlabs FB400-40 and FB550-40 bandpass filters [59] that have a central pass band of 400 and 550 nm each with a Full Width Half Max (FWHM) of 40±8 nm. These wavelengths are selected as they are within the sensitivity range of the ProxiVision camera (see Fig. 3.14 and 3.15). The entire optical system is mounted on an optical breadboard on top of a linear stage so that all components can move perpendicular to the optical axis.

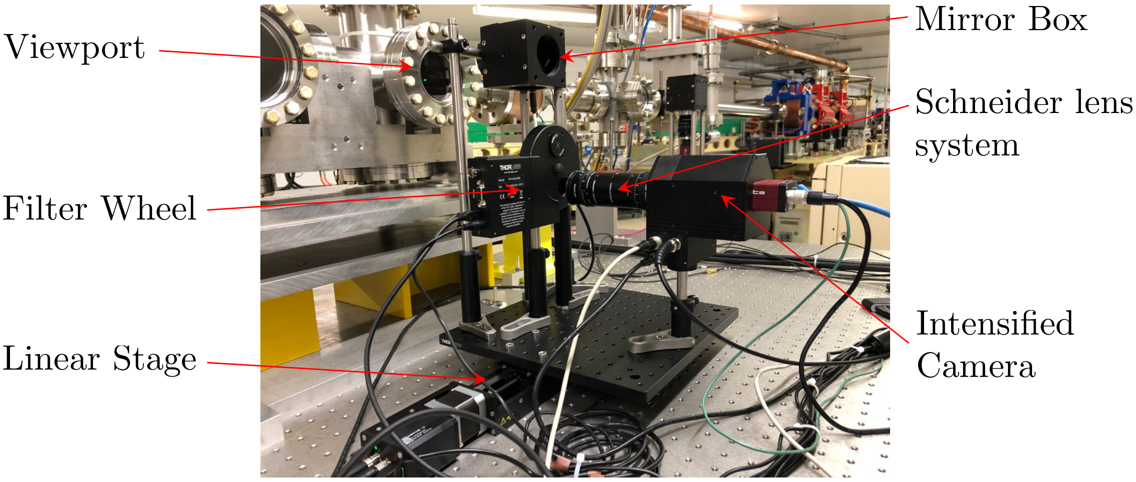

Figure 3.10: Optical System used for initial imaging experiments.

Figure 3.11 shows a simplified block diagram of the ProxiKit Package camera [58]. A phosphor screen and high voltage Micro Channel Plate (MCP) is used to create a photon cascade for any photons that enter the ProxiVision camera system increasing the sensitivity [58]. The cascade photons are coupled into a fibre taper where they are fed into the image sensor of an off-the-shelf Manta G145-B GigE camera. As the fibre taper is larger than the camera sensor the effective pixel size of the GigE camera is increased from 6.45 µm × 6.45 µm to 10.55 µm × 10.55 µm [58, 60].

The intensifier has two input signals: a trigger pulse to control the acquisition timing and a voltage between 0 and 5 V to set the MCP gain. A control unit is used to configure the intensifier gain and trigger settings by connecting to the camera system via a HIROSE cable. The trigger pulse is used to gate the image acquisition around a specific event, such as the bunch as it passes the ChDR radiator. As the camera system also incorporates a GigE camera, all of the standard GigE camera settings (gain, exposure, etc) need to be configured.

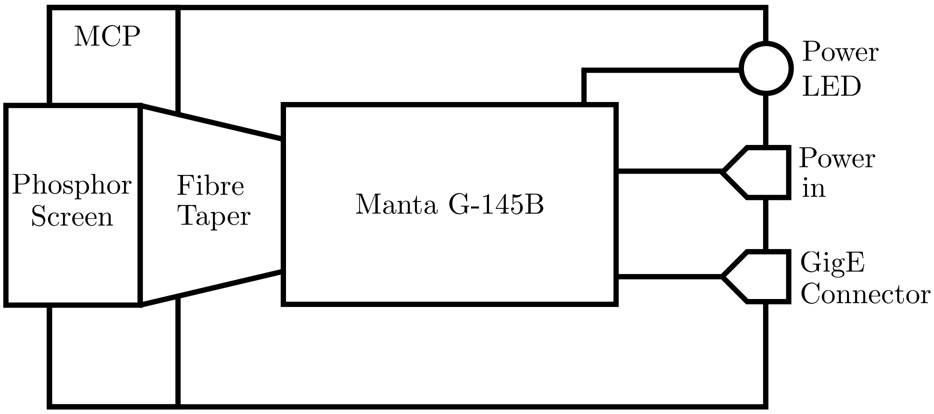

Figure 3.11: Block diagram of Proxi Kit Package imaging system [58].

To obtain the magnification of the optical system the lens to sensor length is adjusted until it focuses onto the ChDR target. The optical path is then redirected using a mirror onto a piece of grid paper. Figure 3.12 shows the reference image taken of the in-focus grid paper, the red lines each show a length of 25 mm and a pixel count of 510 ± 5. The magnification, m, is then calculated by using

$$m = \frac{O[\text{pixels}] \times p[\mu\text{m/pixels}]}{O[\mu\text{m}]}, \tag{3.8}$$

where O signifies the object size in either pixels or µm, and p is the effective pixel size of the camera. Using the object sizes of 510 ± 5 pixels, 25 mm, and a pixel size of 10.55 µm yields a magnification of 0.215 ± 0.002.

Figure 3.13 shows a reference image of the ChDR target holder, where annotations have been added showing the location of the OTR screen and ChDR radiator in the image. The stage positions used in Fig. 3.13 are used as a starting point when performing ChDR experiments. Slight adjustments are then made to optimise the measurements.

Measuring the ChDR spectral response is of great importance in order to compare the measurements with theory. Measurements are made at two wavelengths using the bandpass filters inside the filter wheel. The transmission of the central wavelength for the bandpass filters is not equal. The relative transmission for the central filter wavelength of the 400 nm filter is 0.45 whereas for the 550 nm filter it is 0.7, for this reason the measurements need to be scaled in order to compare them [59].

Additional to the bandpass filters the sensitivity of the intensifier and off-the-shelf camera must be taken into account when analysing the spectral response of any measurements using

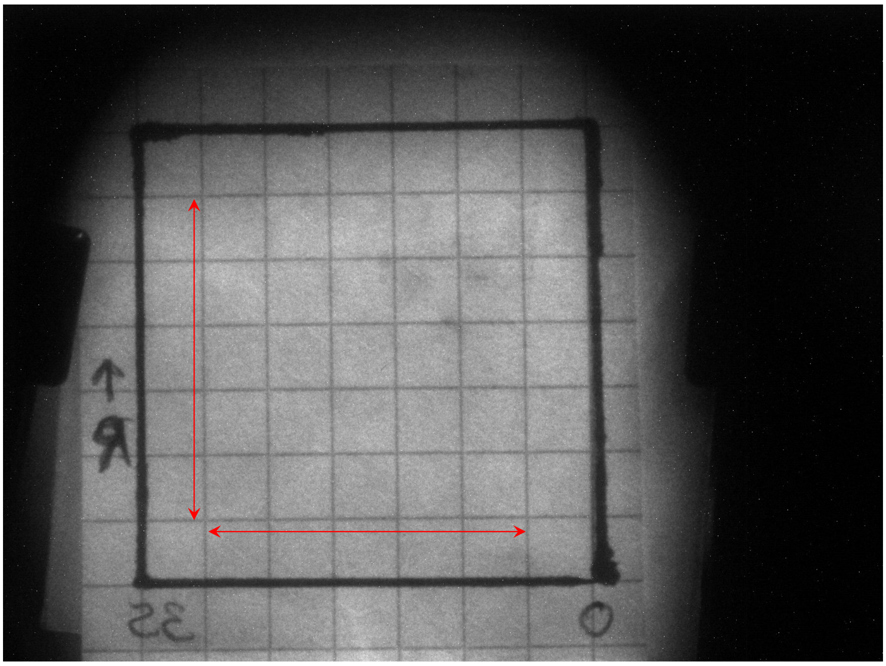

Figure 3.12: Initial ChDR optical system grid paper image used for magnification measurement. Each red line represents a length of approximately 510 pixels and 25 mm.

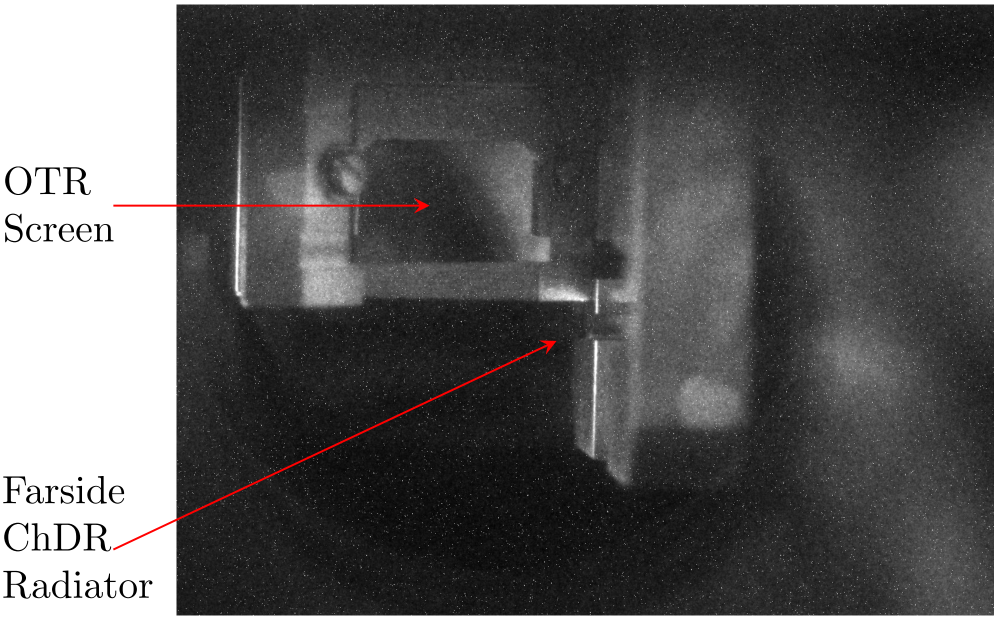

Figure 3.13: Annotated reference image of ChDR target holder.

the ProxiKit package camera. ProxiVision has provided sensitivity measurements for specific wavelengths in the optical range between 200 and 800 nm. Fig. 3.14 shows the intensifier sensitivity measurements provided.

Figure 3.15 shows the Quantum Efficency (QE) for the Manta G145-B camera incorporated into the camera system. Combining the sensitivities from Fig. 3.14, 3.15, and the bandpass

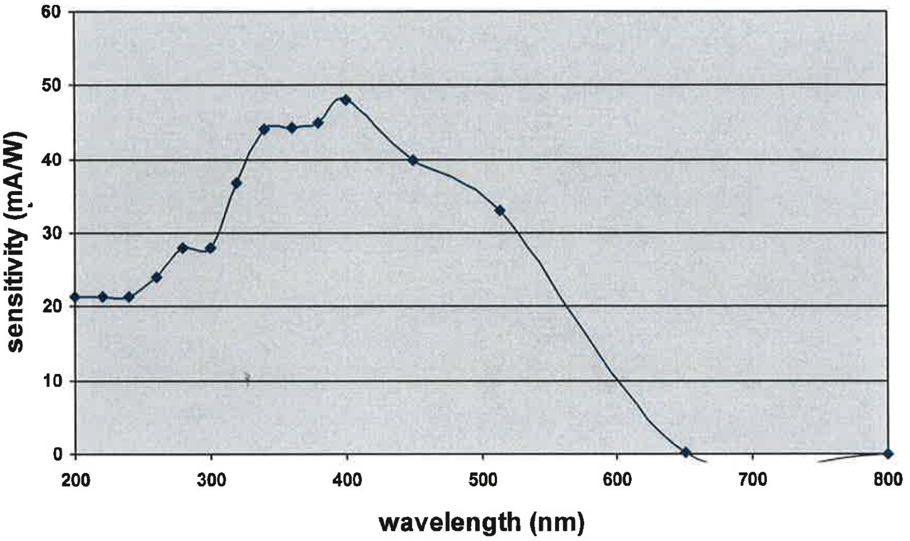

Figure 3.14: ProxiKit Package intensifier spectral sensitivity [58].

filters at 400 nm and 550 nm yields a sensitivity of approximately 7.1 mA/W and 8.2 mA/W respectively [58]. As the resulting sensitivity is not the same for each filter results taken from each setup should be normalised in order to perform a fair comparison.

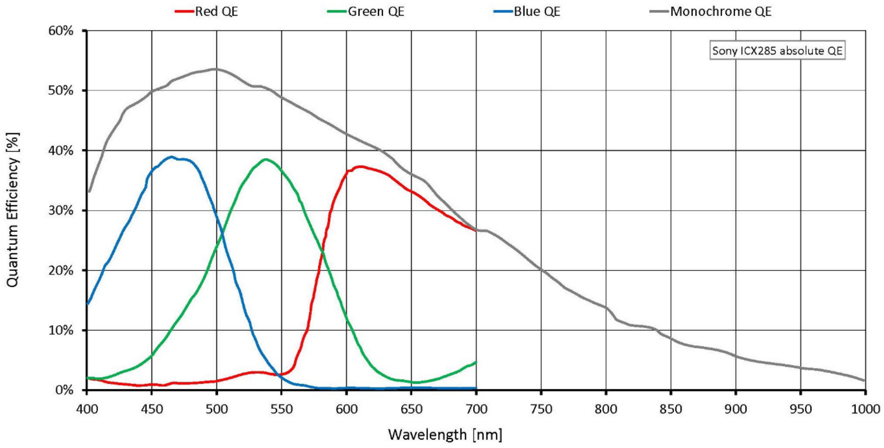

Figure 3.15: Manta G-145B spectral sensitivity [60].

3.2.3 Updated Cherenkov Diffraction Radiation Optical System: Revision 1

Figure 3.16 shows the optical system that was designed to image the ChDR emission and measure the angular distribution. All of the optical components are mounted on an optical breadboard apart from the 500 mm focal length lens that is mounted directly outside of the ChDR viewport. The 500 mm lens is used to measure the ChDR angular distribution and the 100 mm lens is used to image the ChDR emission. Both lenses are mounted on lens flippers so that they can be inserted and removed from the optical path as needed.

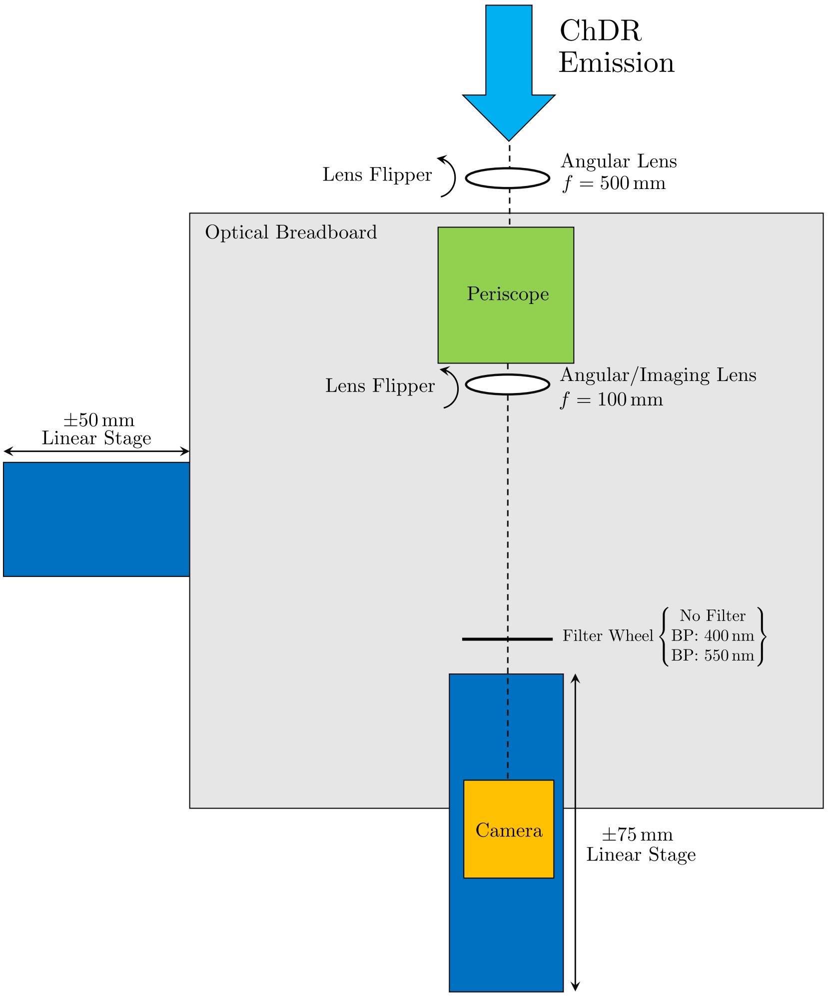

Figure 3.16: Top-Down schematic of ChDR optical system.

A single particle angular distribution simulation was produced for the Diamond BTS beam parameters at an impact parameter of 1 mm and a wavelength of 600 nm using the PCA model and simulation framework from Chapter. 5. Simulations have shown that the angular distribution size is larger at longer wavelengths and shorter impact parameters. The values used for this simulation provide an approximation for an angular distribution with extents of approximately 1.05 mrad in the polar plane and approximately 0.05 mrad in the azimuthal.

In order to ensure that the distribution can be measured, the angular resolution of the detector is considered. The angular resolution of an optical system is given by

$$\Delta\theta = \tan\left(\frac{p}{d}\right), \tag{3.9}$$

where p is the detector pixel size and d is the back focal length. The largest focal length lens that will fit into the spatial constraints of the optical table is 500 mm. Using the lens focal length and the ProxiVison camera, the pixel size in Eq. 3.9 yields an angular resolution of approximately 0.021 mrad/pixel. Using the simulated maximum angular distribution size and the angular resolution, the measured distribution is expected to cover a maximum of approximately 2.5 pixels in the polar plane and 50 pixels in the azimuthal. The system is designed to use the 500 mm lens for angular measurements, but the 100 mm lens can also be used if the 500 mm lens is moved off the optical axis and the motor stages are adjusted accordingly. Working in the angular plane for the 100 mm lens yields an angular resolution of approximately 0.042 mrad/pixel.

3.2.4 Updated Cherenkov Diffraction Radiation Optical System: Revision 2

The optical system had to be redesigned as the ChDR angular distribution proved to be larger than the initial simulations predicted. The redesigned optical system is shown in Fig. 3.17. The 100 mm lens is replaced with a 80 mm focal length lens that has a diameter of 5.08 cm. To further compress the ChDR distribution a relay lens, that has a focal length of 30 mm, is used. Using Eq. 3.9 to obtain the angular resolution with the ProxiVision camera pixel size and the 80 mm, lens yields a resolution of approximately 0.132 mrad/pixel. The relay lens used increases the angular resolution by a factor of approximately 2 giving a final effective angular resolution of approximately 0.264 mrad/pixel.

The optical system is still able to measure angular distributions and images, both lenses are used for each setup but the camera position changes. When imaging the ChDR target the system has a magnification of approximately 0.2. The lens flippers have been removed from the optical system, as both lenses are required for angular or imaging measurements.

In addition to the changes in the lens used in the optical system, the top mirror of the periscope system is replaced with a mirror that is fitted to a motorised system allowing it to vertically tilt. Combining the vertical movable mirror with the lateral stage allows the entire system to scan the ChDR emission viewport vertically and horizontally. The linear stage on the optical axis is used in order to move the camera sensor between the angular and imaging planes.

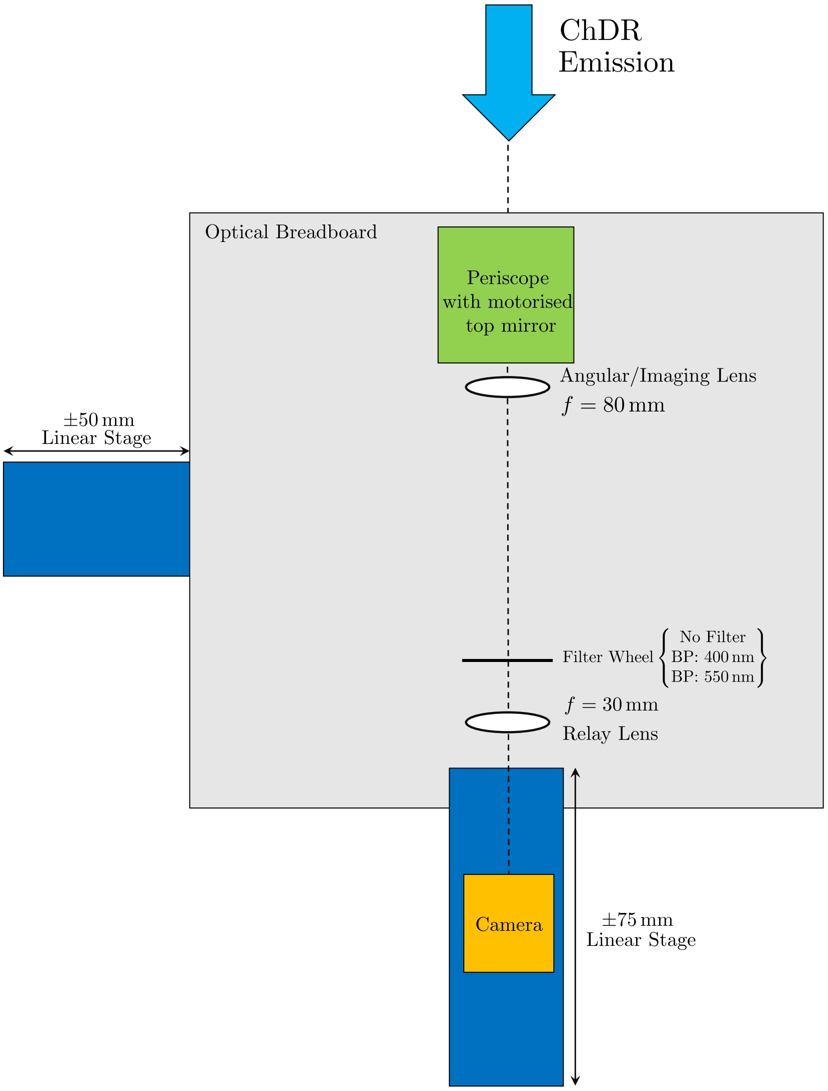

Figure 3.17: Top-down schematic of revised ChDR optical system.

3.2.5 Photomultiplier Tube Detector and Data Acquisition System

After performing experiments with the ProxiVision camera and producing simulations described in Chap. 5, a decision was made to take experimental results at longer wavelengths with a high sensitivity detector. This was due to the lack of signal measured with the ProxiVision camera at large impact parameters. As a PMT is a single pixel detector it is more sensitive than a comparable camera. Additionally simulations showed that longer wavelengths are favoured at larger impact parameters so a PMT could be selected that is sensitive to longer wavelengths than the ProxiVision camera.

A Hamamatsu H10722-20 [61] PMT was installed in place of the ProxiVision camera. This PMT was used with the second revision of the optical system described in Sec. 3.2.2, using the same initial stage positions as those used for angular distribution measurements.

Figure 3.18 shows the PMT mounted on the optical system. A wall of lead bricks has been built around the upstream portion of the setup to reduce background noise created on the PMT from beam loss. This was not included for the ProxiVision camera, the lead bricks were added as the signal from the PMT was found to be more sensitive to the beam loss. For both the ProxiVision camera and the PMT setup also has a metal frame with a dark curtain draped over it to reduce any ambient light that will be in the tunnel during beam operations.

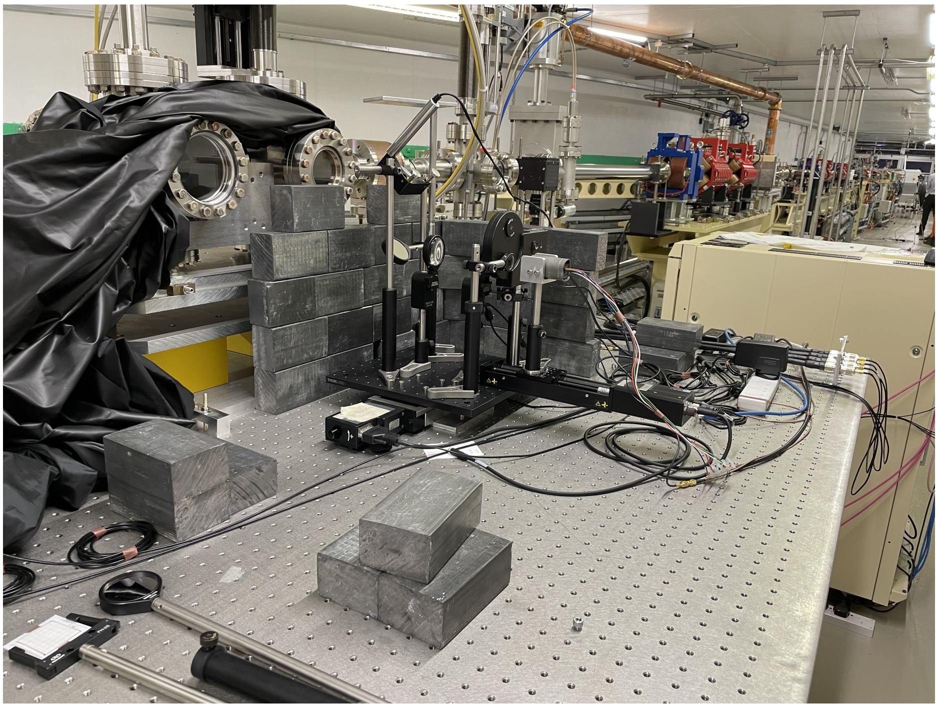

Figure 3.18: Image of the Diamond BTS optical table with the PMT, optical system, and lead shielding installed.

Figure 3.19 shows the schematic of the PMT. The PMT is externally powered with a ±5 V power supply where the gain of is set by applying a voltage between 0.5 and 1.1 V.

Figure 3.20 shows the spectral and gain response of the PMT. This PMT was chosen as it is sensitive to wavelengths longer than the ProxiVision camera, but the wavelengths are not so long that the lenses in optical system would need to be replaced.

In order to acquire the data from the PMT and also set the gain, a RedPitaya Data Acquisition (DAQ) board is used [62]. Figure 3.21 shows a RedPitaya and labels the major parts on the board. One of the 14-bit RF inputs is used to acquire data from the PMT at a rate of 125 MS/s [62]. A single RF output channel can provide a voltage up to 1 V, one of these is used to externally and remotely control the gain of the PMT [61, 62].

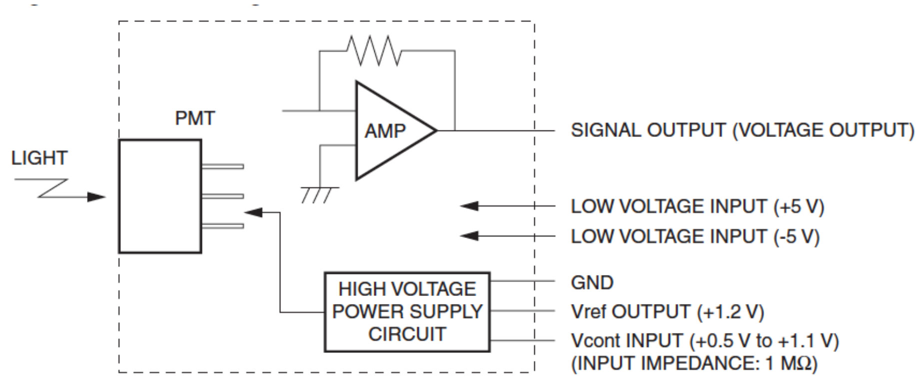

Figure 3.19: PMT block diagram schematic [61].

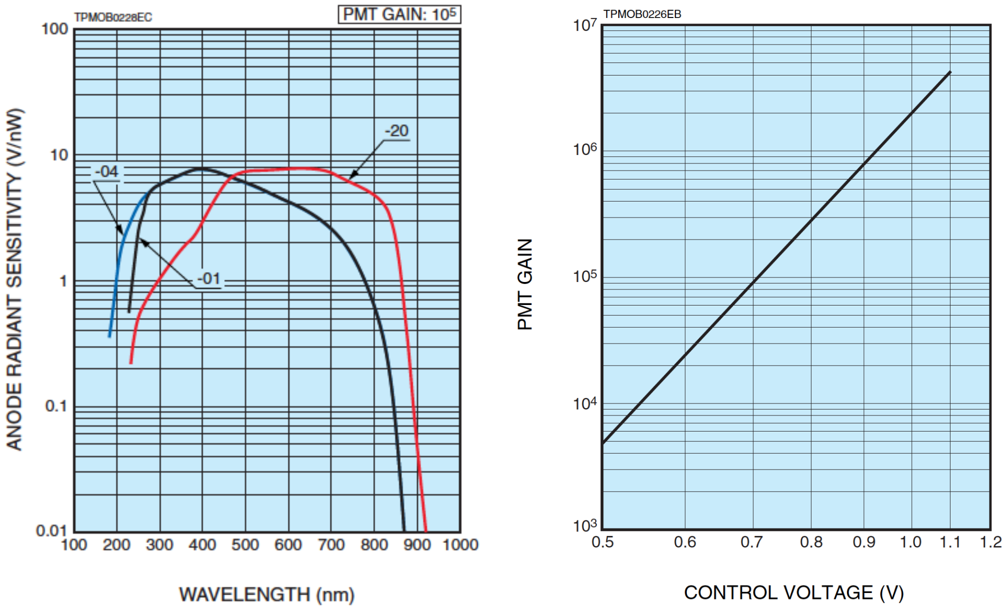

(a) Spectral Response.

(b) Gain Response.

Figure 3.20: PMT Characteristics [61].

A LabVIEW application was developed to remotely connect to and control the RedPitaya. An external trigger is connected to the RedPitaya so that the acquisition is synchronised with the other BTS diagnostics (see Sec. 3.1.3).

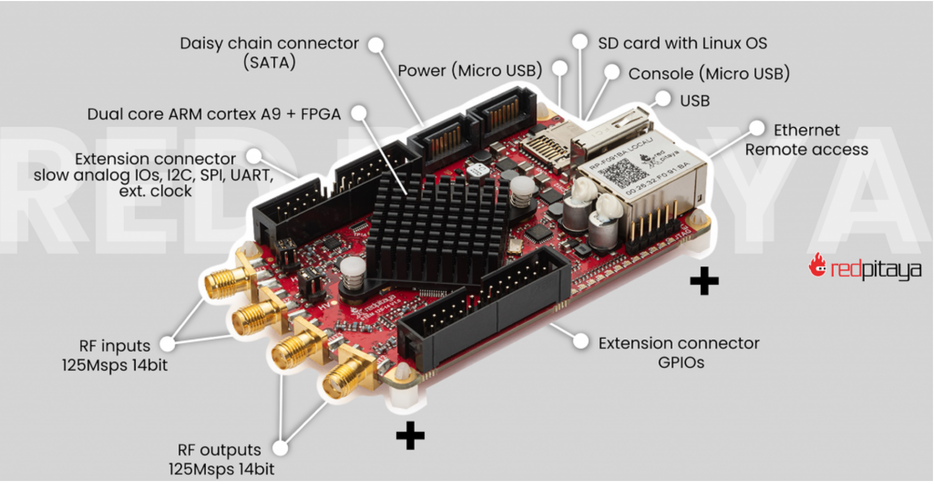

Figure 3.21: Labelled RedPitaya DAQ unit [62].

CHAPTER 4

DIAMOND BEAM TEST STAND COMMISSIONING

Initial experiments on the Diamond BTS were performed to commission the diagnostics and accelerator control systems. For this work the OTR monitors, the IBPM, the triggering, and data acquisition systems were all commissioned. During this process the codes provided to adjust the beam position and profile were characterised.

4.1 Optical Transition Radiation Monitors

The three OTR systems setup on the BTS are denoted: OTR1, OTR2, and OTR3, where the most upstream monitor is OTR1, and the most downstream, OTR3 (see Fig. 3.1). Figure 4.1a shows an image taken from the monitor OTR1 when a single bunch is passed through the OTR screen. The bright spot in the centre of the image is the TR emitted by the screen when the electron beam passes through it. Fitting the two dimensional Gaussian distribution from Eq. 3.6 to Fig. 4.1a yields Fig. 4.1b and the beam profile parameters in pixels.

In order to convert from pixels to the beam measurements, the fit must be converted using Eq. 3.8 where m_h and m_v respectively denote the horizontal and vertical magnification. As the horizontal and vertical pixel sizes are 3.45 µm on all OTR monitors with a magnification of approximately 0.19, the absolute scaling factor

$$\sigma[\mu\mathrm{m}] = \sigma[\mathrm{pixels}] \times 18.16[\mu\mathrm{m/pixel}], \tag{4.1}$$

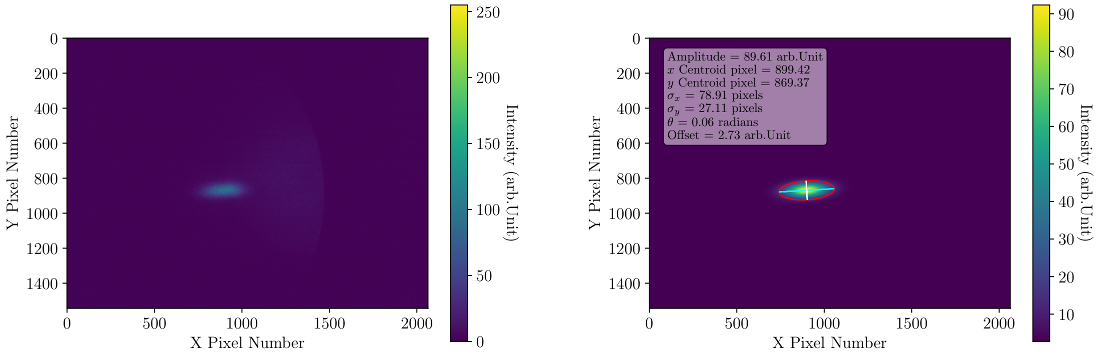

(a) Raw image.

(b) 2D Gaussian fit.

Figure 4.1: OTR1 nominal beam image.

is used for beam measurements on all OTR monitors. The fit in Fig. 4.1b yields a beam size of approximately 1.47 mm horizontally and 0.48 mm vertically. Both of these are in agreement with the general BTS parameters listed in Table. 3.1.

Obtaining the absolute beam position with the centroid measured from the OTR monitor setup on the BTS is not possible, instead relative movements from the nominal beam centroids, Δx and Δy, are used. Relative movements are calculated using the relationships

$$\begin{aligned} \Delta x &= x_0 - x_n, \\ \Delta y &= y_0 - y_n, \end{aligned} \tag{4.2}$$

where x_n and y_n are the nominal horizontal and vertical beam centroid positions, and x_0 and y_0 are the centroid positions measured in subsequent images. The nominal beam positions are reset at each experimental shift as the starting beam position. This is done in order to compare relative differences between the OTR monitors and IBPM, when calculating the absolute impact parameter (see Sec. 4.4) these nominal positions are not used. The relative horizontal and vertical movements are also scaled using Eq. 4.1 to convert from pixels to µm.

The OTR monitors have been commissioned using both the YAG and OTR screens, in both single bunch and multi bunch extraction. Regardless of extraction setting or screen used the analysis process is the same for the monitor. The only consideration is that the photon yield will vary and the settings of the camera system should be adjusted in order to compensate ensuring that the images are not saturated.

4.2 Inductive Beam Position Monitor

The IBPM has been tested using both single bunch and train extraction. Figure 4.2 shows the captured IBPM waveforms for both a train and single bunch extraction. Both waveforms have a total extracted charge of approximately 0.2 nC, where the charge is distributed across the 120 bunches extracted for the train. As the charge is distributed for the multi bunch train extraction, the measured voltage signal is of a lower amplitude that cannot be distinguished above the noise. The single bunch extraction in Fig. 4.2 can clearly be seen at approximately 200 ns with an approximate peak amplitude of −40 mV.

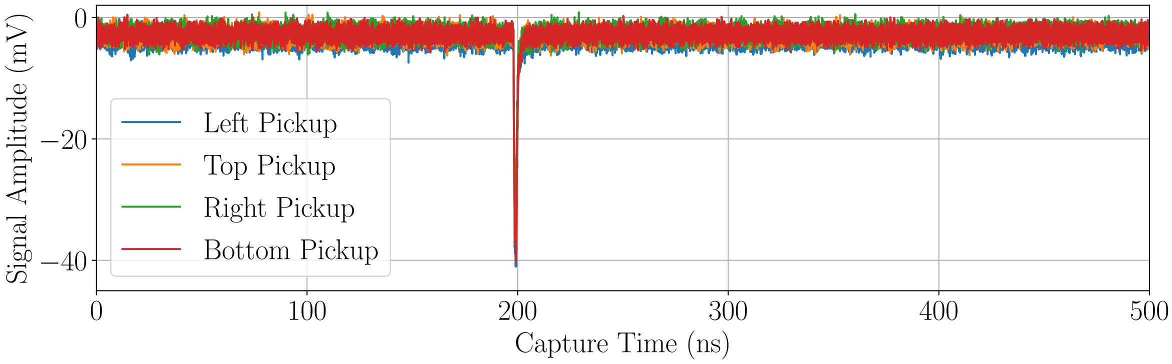

(a) Single bunch extraction.

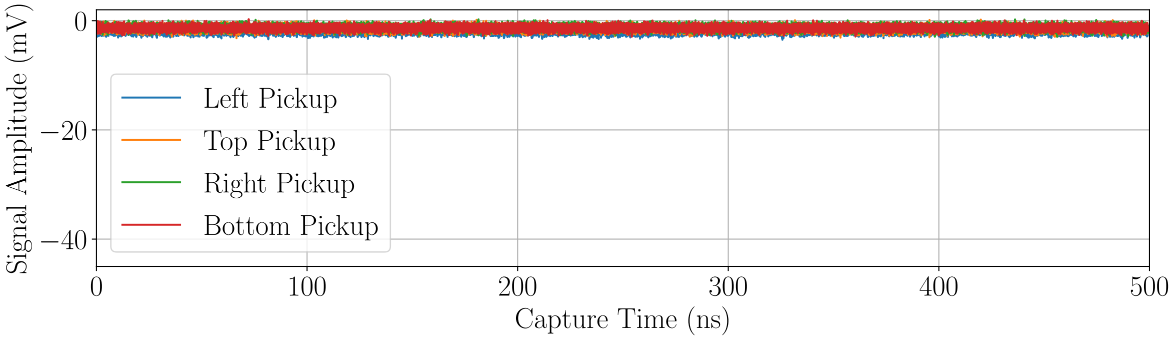

(b) Multibunch train extraction.

Figure 4.2: Full IBPM waveforms showing both single bunch and train extraction.

The noise on each IBPM channel is removed by taking a mean for each channel in the time before the signal is present. The mean values for each channel is offset so the noise is centred around 0 mV. Figure 4.3 shows the single bunch displayed from Fig. 4.2 with the axis extents set around the bunch signal and the noise offset removed.

To obtain the beam position or intensity a scalar value must be obtained from each channel. The shaded area in Fig. 4.3 (between 198 and 200 ns) represents an integration region for this waveform to produce a scalar value from each channel. The integration window in Fig. 4.3 lasts for 2 ns. Table 3.1 shows that the bunch length is much shorter than the pulse length, meaning the response of the IBPM has elongated the signal. Processing the integrated

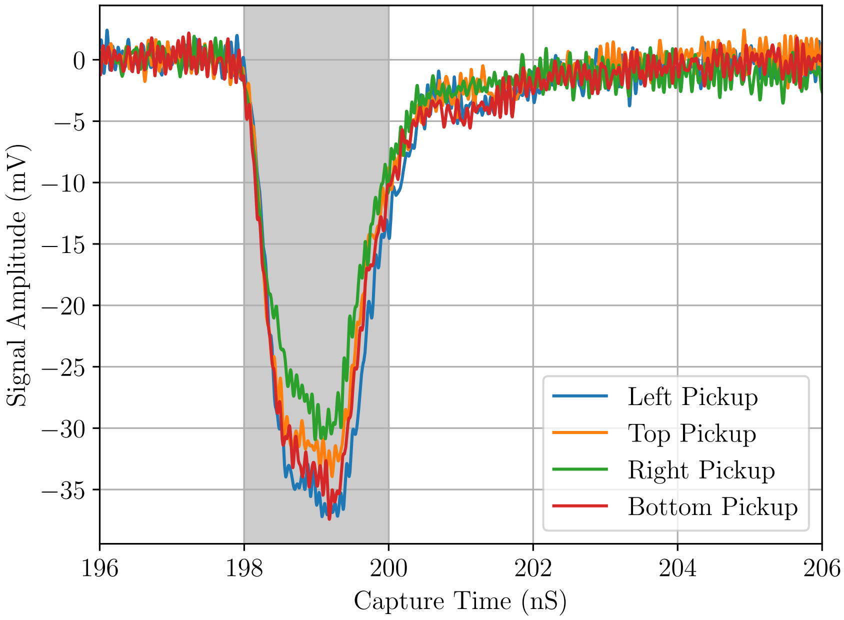

Figure 4.3: Single bunch IBPM bunch waveform, shaded region shows bunch integration window.

values from Fig. 4.3 using Eq. 3.1 and 3.2 gives an absolute horizontal beam position of approximately −1.86 mm, and a vertical of approximately −0.51 mm.

To calculate bunch charge measurements using the IBPM, Eq. 1.15 is used. In order to commission the IBPM for charge measurements, data has been recorded from an upstream ICT for comparison [17]. By varying the RF gun bias voltage V_{Bias} the bunch charge will be altered with the relationship

$$Q \propto \frac{1}{V_{\text{Bias}}}, \tag{4.3}$$

where Q is the bunch charge. As the ICT is not connected to the same IOC as the other diagnostics on the BTS, the data cannot be compared on a shot-by-shot basis. To compare the two monitors, the RF gun voltage is fixed and a number of samples is recorded from both the ICT and the IBPM. The mean and standard deviation is then calculated for each bias setting.

Figure 4.4 shows the data sets for the bunch charge measured from the IBPM and ICT plotted against the RF gun bias. Both monitors show strong correlation between each other with relative change. Each data point in Fig. 4.4 is the mean of a dataset from each diagnostic, the error bars display the standard deviation of the dataset used for each point. In absolute terms the IBPM reads lower. Increasing the magnitude of the IBPM charge measurements by a factor of approximately 1.11, all of the IBPM charge measurements fall within the error bars of the ICT01 displayed in Fig. 4.4 showing that the difference appears to be systematic. The exact cause of this difference is not known but it could be due to real beam losses as the beam passes into the BTS or signal losses in the IBPM cables. Another discrepancy between the ICT and IBPM may be due to limitations of the triggering setup when this data was taken. For the IBPM only three samples were taken at each bias setting, whereas over 100 were taken for each with the ICT potentially accounting for the difference between the two readings.

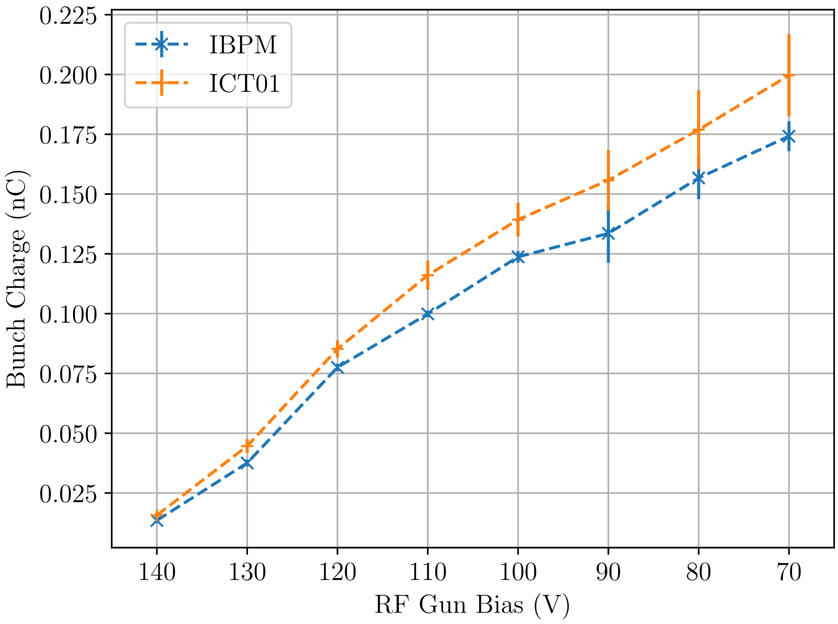

Figure 4.4: IBPM and ICT bunch charge measurements correlated against RF gun bias voltage. Each point shows the mean of the dataset calculated, similarly the error bars show the standard deviation of the dataset used for each point.

4.3 Beam Adjustment Codes

Diamond staff have provided beam adjustment codes to alter the transverse beam position and profile through the Diamond BTS. The position adjustment codes were fully characterised during the commissioning, whereas the work with the profile codes was less thorough.

4.3.1 Beam Position Adjustment Codes

Altering the beam trajectory through the BTS is done by adjusting the corrector magnets on the extraction line. The beam position adjustment codes take the inputs, C_x and C_y, that respectively provide a horizontal or vertical bump to the beam position. As the beam adjustment codes exhibit non-linear beam position movements when performing large position shifts, the unit used to control the beam bumps is referred to as a Bump Unit (BU). To commission these codes a series of horizontal or vertical bumps were set, and then data taken with OTR1, OTR2 and the IBPM.

In order to commission the beam adjustment codes, a C_x and C_y scan was performed from -2500 to 2500 BU in steps of 500 BU. Ideally a changing the C_x bump value will only change the horizontal beam position, similarly changing the C_y bump should only change the vertical beam position. Any movement of the beam position on the undesired axis is considered as a coupling between the two in the beam adjustment codes.

Figure 4.5 shows the change from the nominal horizontal and vertical beam position as Δx and Δy respectively for the three monitors during the C_x scan.

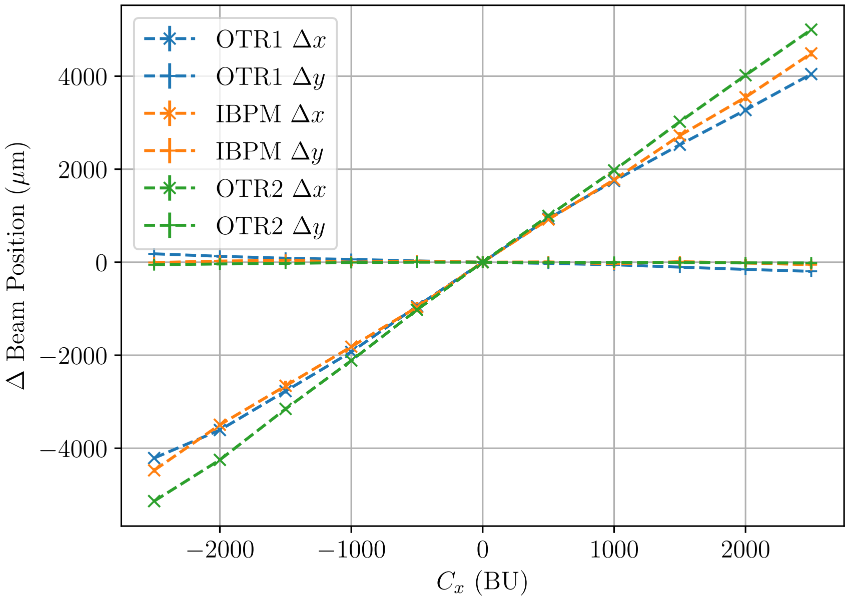

Figure 4.5: Relative transverse beam position movements measured from nominal when changing the beam position adjustment code horizontal input C_x.

All three monitors have a good agreement that a positive C_x value provides a positive change in the horizontal transverse beam position. At the far extents the change in horizontal position is largest on OTR2, then the IBPM. This is expected as the bumps are expected to produce a tilt into the beam trajectory that will be more exaggerated on the monitors that are more downstream of the BTS (see Fig. 3.1). Figure 4.5 shows a small degree of coupling is measured on the OTR monitors but not the IBPM. As the IBPM measures the absolute beam position, this is assumed to be partially an error in the OTR measurement system, and not entirely a beam effect. This coupling can be explained by a tilt in the optical system or because the beam becomes very close to the edge of the screen creating reflections that interfere with the 2D Gaussian fit.

Figure 4.6 shows the change in horizontal and vertical beam position when performing a C_y scan with the beam position adjustment codes. Similar to Fig. 4.5, Fig. 4.6 shows that the bumps prove a beam position shift in the desired direction with good agreement on all monitors when considering their respective places on the BTS. A degree of coupling is measured in Fig. 4.5 where this of a similar magnitude as the coupling displayed in Fig. 4.6.

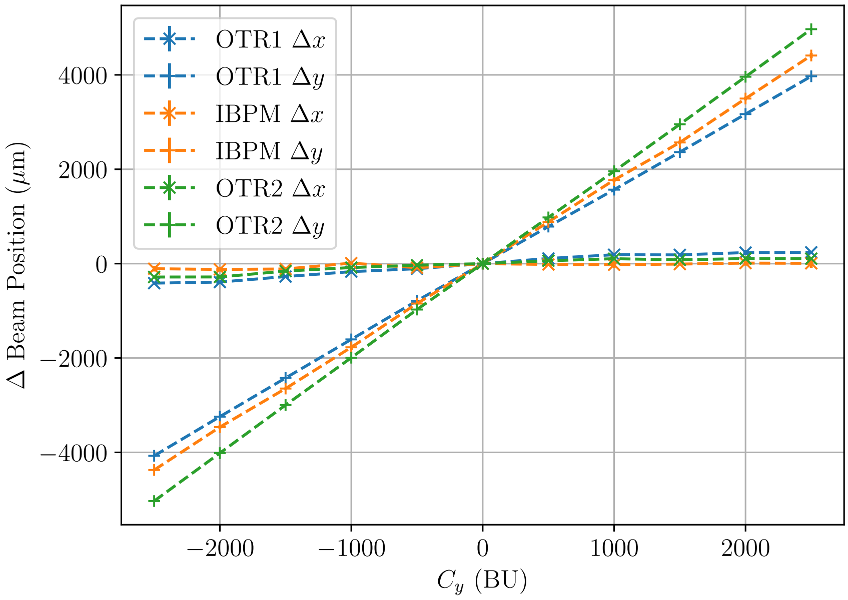

Figure 4.6: Relative transverse beam position movements measured from nominal when changing the beam position adjustment code vertical input C_y.

The commissioning of the beam position adjustment codes show that there is good cross referencing between the three monitors used and minimal coupling between the vertical and horizontal bumps.

4.3.2 Beam Profile Adjustment Codes

The Diamond Accelerator Physics group have provided codes that manipulate the beam profile on the BTS. The codes change the settings on an upstream quadruple magnet to produce a horizontal or vertical waist onto the beam. There are five different settings for the horizontal and vertical waists, these are referred to as fit-points. In addition to the fit-points, there are 30 fit-point cases that move the beam waist location on the BTS. Figure 4.7a shows the beam profile measured using an OTR screen from OTR1 when fit-point 1 case 14 was applied to the beam.

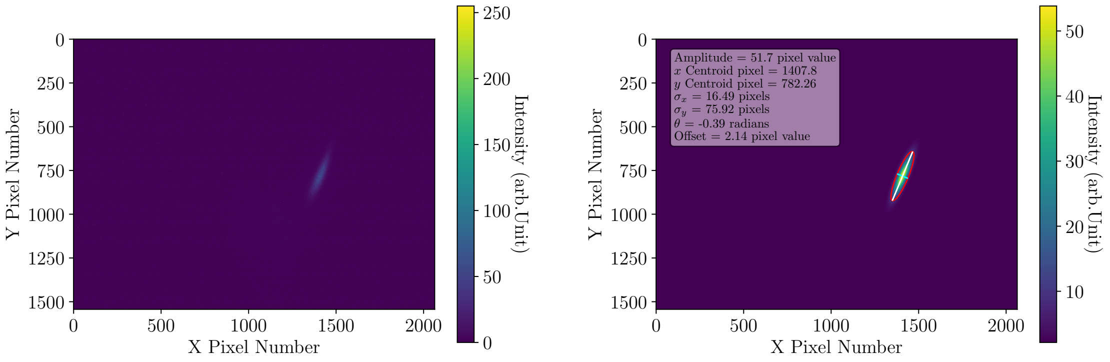

(a) Raw image. **(b)** 2D Gaussian fit.

Figure 4.7: Beam profile taken from the OTR screen on OTR1 with horizontal fit-point 1 case 14 applied.

Figure 4.7b shows the Gaussian fit from Eq. 3.6 applied to Fig. 4.7a. Using the parameters of the OTR optical system described in Sec. 3.1.2 the fit yields σ_x of approximately $300 \pm 90\,\mu\text{m}$, and σ_y of approximately $1400 \pm 90\,\mu\text{m}$ where the error is obtained from the magnification error. The testing of these codes proves that the beam profile can be changed into sizes that are different than the nominal beam. Testing showed that the beam profile would evolve throughout the BTS when applying a fit-point so a profile measurement from OTR1 would be different from OTR3. The coupling between the different diagnostic instruments on the BTS was not characterised for this thesis due to experimental time considerations.

4.4 Beam Trajectory

To characterise the ChDR pickup response the impact parameter between the beam and ChDR radiator must be known. A complication when calculating the impact parameter is due to the tilt introduced from beam bump codes. Accounting for the tilt the impact parameter is calculated by bumping the beam horizontally towards the ChDR target holder until the target holder shadow is seen on the downstream OTR2 image. For this analysis ten shots were fired from the accelerator with the first shot used as a warm up, for the remaining nine shots data was taken from OTR1, OTR2 and the IBPM. Figure 4.8a shows one of the images taken from OTR2 where the shadow from the ChDR target holder is present. Figure 4.8b shows Fig. 4.8a cropped around the beam shadow with a more sensitive colour map. Of particular importance is the horizontal shadow position that is found at 1820 ± 5 pixel.

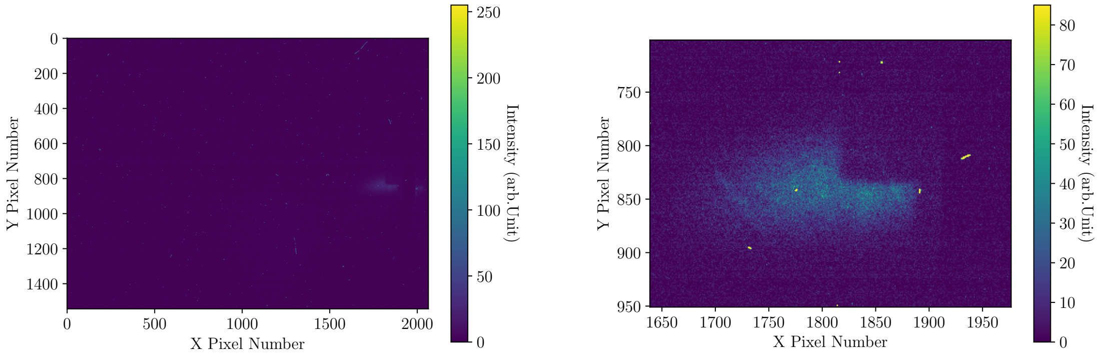

(a) Raw image. **(b)** Cropped image with sensitive colour map.

Figure 4.8: Image taken from OTR2 where the shadow of the ChDR target holder is present.

Care was taken so that the target holder would only intersect half of the horizontal beam. The centroid or position measurement from OTR1 or IBPM can be used to calculate the intercepting trajectory with the ChDR target holder.

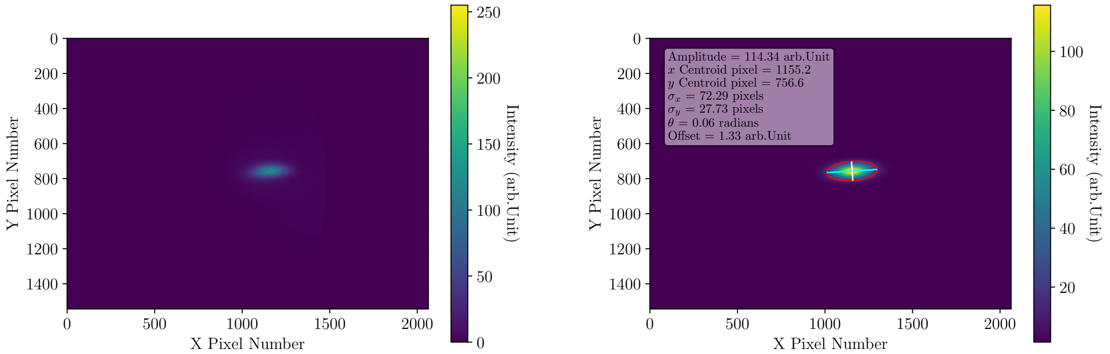

(a) Raw image. **(b)** 2D Gaussian fit.

Figure 4.9: Corresponding image from OTR1 when the image from Fig. 4.8 was taken.

Data from the IBPM was also obtained for trajectory analysis. Table 4.1 shows the raw and processed values for OTR1, OTR2 and the IBPM. The uncertainty in the values shown in

Table. 4.1 is the measurement uncertainty summed with the standard deviation from the nine measurements.

Instrument	Raw Position	Processed Position
OTR1	$1155 \pm 10\,\text{pixels}$	$20975 \pm 185\,\mu\text{m}$
OTR2	$1820 \pm 10\,\text{pixels}$	$33051 \pm 185\,\mu\text{m}$
IBPM	$x_{raw} = -0.31 \pm 0.008$, $y_{raw} = -0.028 \pm 0.014$	$x_{mod} = 4908 \pm 135\,\mu\text{m}$

Table 4.1: Raw and processed position values from the BTS diagnostics for the beam position that intersects the ChDR monitor.

Figure 4.10 shows how the impact parameter between the ChDR radiator and a beam passing through the BTS is calculated using the intersecting beam trajectory. To obtain the impact parameter the intersecting trajectory on OTR2 is needed with either OTR1 or the IBPM as an upstream diagnostic. The notation in Fig. 4.10 shows that D is the longitudinal distance between an upstream diagnostic and OTR2, L is the longitudinal distance between the upstream diagnostic used and the ChDR monitor, $X1_0$ is the horizontal beam centroid taken from the upstream diagnostic when the beam collides with the ChDR holder, $X2_0$ is the horizontal position of the ChDR holder shadow measured on OTR2, and $X1_1$, $X2_1$ are respectively the positions on the upstream diagnostic and OTR2 of the bumped beam passing through the BTS.

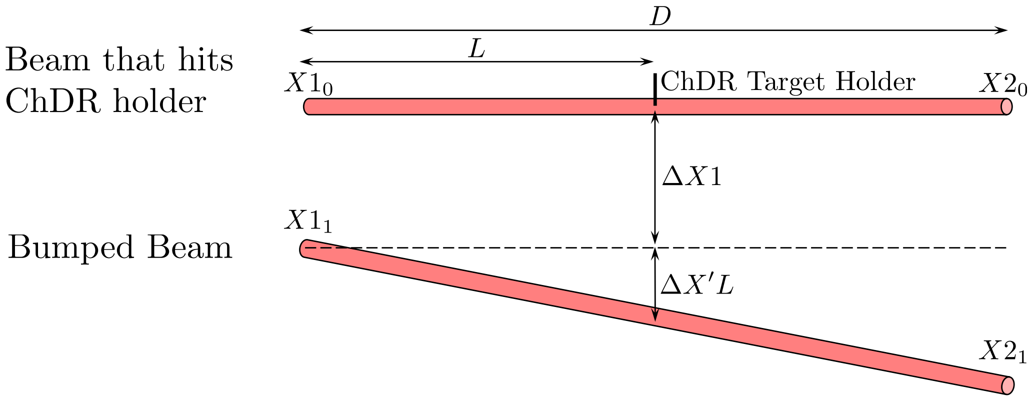

Figure 4.10: Geometrical method of impact parameter calculation from beam trajectory.

The change in position on the upstream diagnostic, $\Delta X1$, is then calculated by taking the difference between the current measurement and intersecting measurement for that diagnostic, such that

$$\Delta X1 = X1_1 - X1_0. \tag{4.4}$$

Should there be no tilt added to the beam position when bumping the beams this would be the same as the shift on OTR2 and the impact parameter. The longitudinal tilt contribution is given by $\Delta X'L$ where

$$\Delta X' = \frac{(X2_1 - X2_0) - (X1_1 - X1_0)}{D}. \tag{4.5}$$

Combining these the impact parameter is then calculated as

$$b = \Delta X1 + \Delta X' L, \tag{4.6}$$

that can be expanded as

$$b = (X1_1 - X1_0) + \frac{L((X2_1 - X2_0) - (X1_1 - X1_0))}{D}. \tag{4.7}$$

Using the mechanical dimensions from Fig. 3.1 the distances between the different monitors are taken to the nearest mm with a cautious uncertainty of 5 mm added for potential deviation from the design drawing. These values along with the monitor positions for intersecting trajectories are shown in Table. 4.2.

Parameter	Values for OTR1	Values for IBPM
D	1540 ± 5 mm	1110 ± 5 mm
L	735 ± 5 mm	307 ± 5 mm
$X1_0$	20975 ± 185 µm	4908 ± 135 µm
$X2_0$	33051 ± 185 µm	33051 ± 185 µm

Table 4.2: Variable values for calculating the impact parameter when using Eq. 4.7 with either OTR1 or the IBPM in conjunction with OTR2.

An impact parameter value is obtained by measuring a beam position or centroid from either OTR1 or the IBPM, along with OTR2. The processed measurement positions are then used in conjunction with Eq. 4.7 and the values from Table. 4.2 to give the impact parameter.

4.5 Cherenkov Diffraction Radiation Optical System

4.5.1 Optical System Alignment

The optical system from Fig. 3.17 was designed and installed to increase the angular acceptance and magnification of the ChDR detection system. The OTR screen fit to the ChDR target holder was used to verify the alignment of the optical system. By inserting the target holder fully, the beam intersects the OTR screen instead of passing by the ChDR radiator where the OTR images can be taken (see Fig. 4.11a).

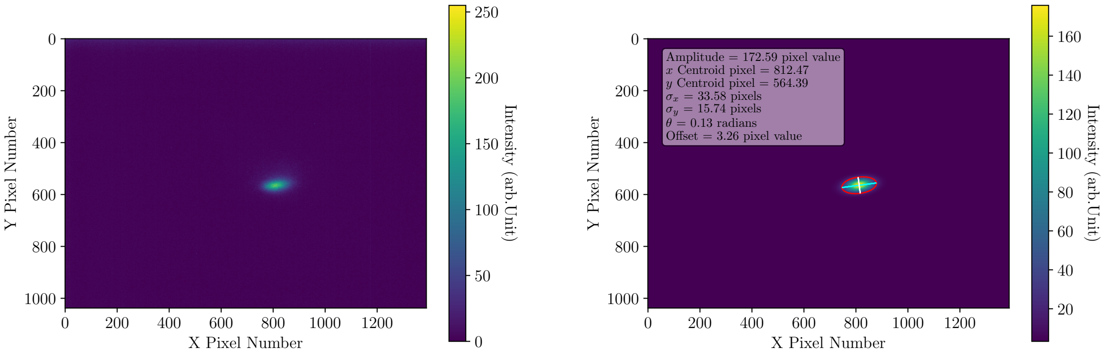

(a) Raw image. **(b)** 2D Gaussian fit.

Figure 4.11: Imaging plane for the OTR screen on the ChDR target holder.

The proportions of the OTR fit in Fig. 4.11b do not match those taken from the OTR commissioning data. The ratio between fit of the major and minor axes on the OTR monitors for a nominal beam from OTR1 is approximately 2.6. This is calculated by taking a beam fit such as that seen in Fig. 4.9b and dividing the σ_x fit parameter by the σ_y parameter. For the OTR screen on the ChDR monitor the fit in Fig. 4.11b is approximately 2.25. This is not a concern as some discrepancy is expected as the optical system used here does not use a Scheimpflug adaptor and the alignment is not optimised for the OTR screen.

As well as imaging the OTR screen, the angular distribution is measured by the optical system. To find the angular focal plane a mirror is placed in front of the ChDR viewport so that the optical axis of the system is facing down the Diamond accelerator tunnel. The position of the linear stage on the optical axis is adjusted until the optical system is focused on a distant object, such as the back wall of the accelerator tunnel. This position is then recorded as it will be the angular focal plane.

Figure 4.12 shows the OTR angular distribution image measured from the optical system. The OTR angular distribution is obtained by setting the optical axis linear stage to the recorded angular focal plane position.

The measured OTR angular distribution is compared with the theoretical OTR angular distribution that is expressed by

$$\frac{\mathrm{d}W_{\mathrm{TR}}}{\mathrm{d}\omega \mathrm{d}\Omega} = \frac{\alpha}{\pi^2} \frac{\theta_x^2 + \theta_y^2}{\left(\gamma^{-2} + \theta_x^2 + \theta_y^2\right)}, \tag{4.8}$$

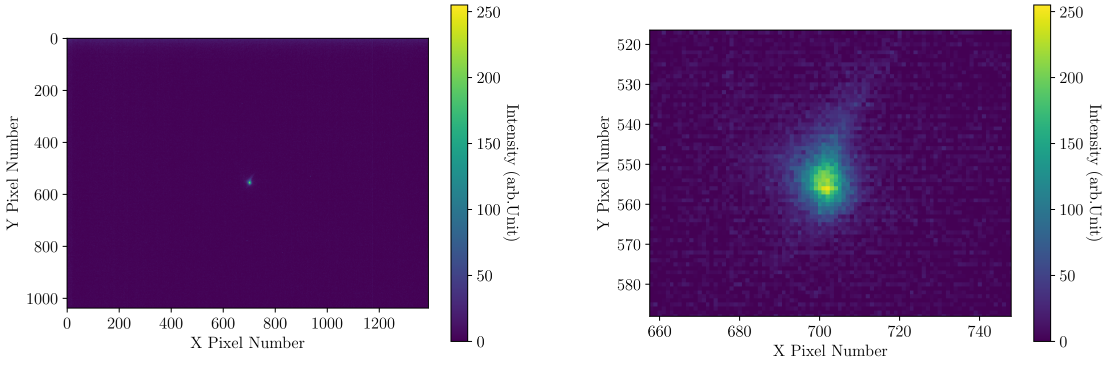

(a) Full image.

(b) Cropped image.

Figure 4.12: Angular plane for the OTR screen on the ChDR target holder.

for a normal incidence screen, where W_{TR} is the photon yield, ω is the photon frequency, Ω is the solid angle, α fine structure constant, and θ_x, θ_y are the horizontal and vertical observation angles respectively [63]. The OTR angular distribution has a distinctive two peak shape where the peaks are separated by the angle, θ_{TR}, expressed by,

$$\theta_{\mathrm{TR}} = \frac{2\,[\mathrm{rad}]}{\gamma}, \tag{4.9}$$

where γ is charged particle Lorentz factor [63]. Figure 4.13 shows the expected OTR angular distribution shape. It is created using Eq. 4.8 and a beam with energy of 3 GeV.

The distance between the OTR angular distribution peaks is calculated as approximately 0.34 mrad using Eq. 4.9. The system is unable to resolve the finer details of the distribution given the large angular magnification of approximately 0.2637 mrad/pixel. The theoretical OTR angular distribution is then passed through a uniform filter with a bin size equal to the angular magnification. Figure 4.14 shows the original distribution from Fig. 4.13 and the resampled filtered distribution.

Horizontal and vertical projections are taken from the measured OTR angular distribution in Fig. 4.12, and displayed in Fig. 4.15. Both of the projections should match the envelope of the filtered distribution in Fig. 4.14 however the width of the projections appears about double what is expected. Given the low magnification of the system this is only an absolute error of approximately 4 pixels. The top right section of image in Fig. 4.12b shows a tail like image created from a slight misalignment. Given this misalignment and the low magnification of the system this is deemed to be acceptable.

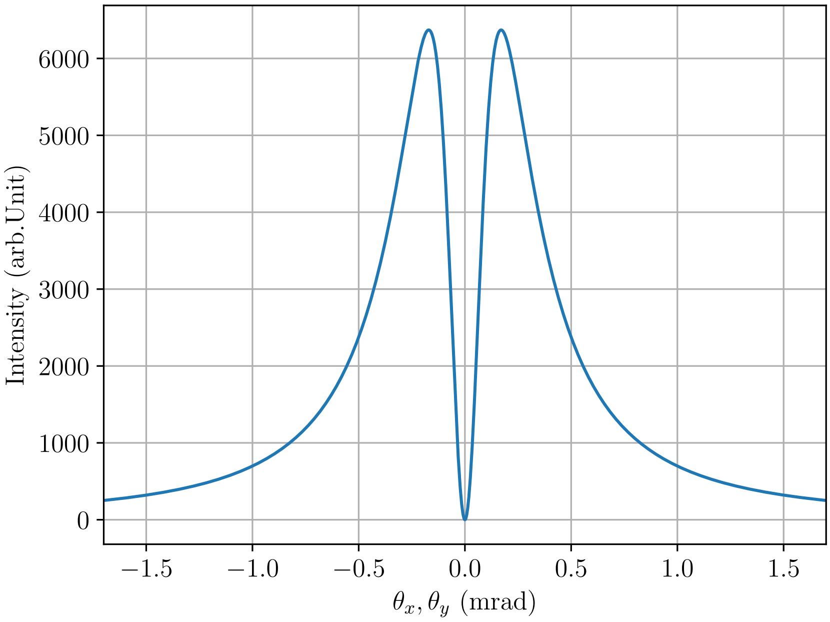

Figure 4.13: Expected OTR angular distribution emitted from a 45° screen and a 3 GeV electron beam, calculated from Eq. 4.8 [63].

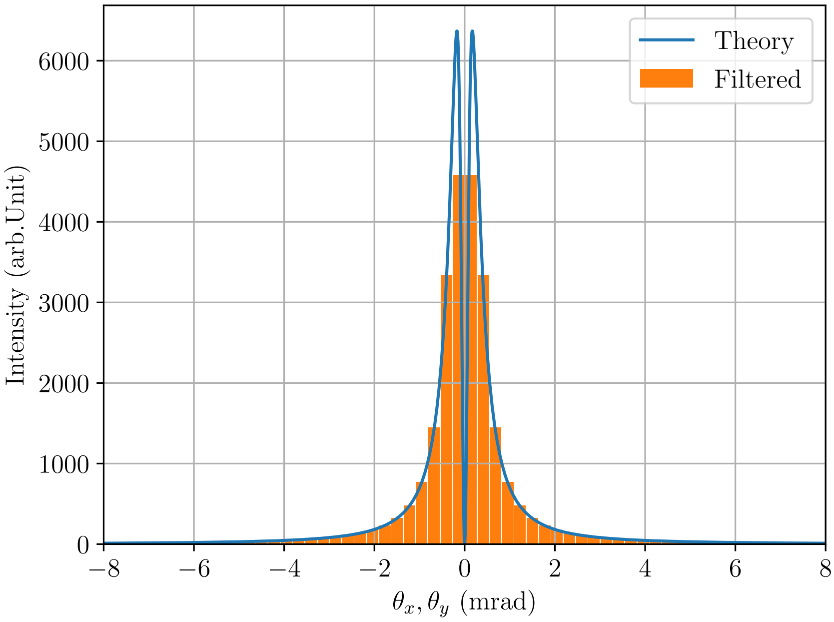

Figure 4.14: Original OTR angular distribution from Fig. 4.13 uniformly filtered and resampled into bins that match the optical angular magnification of approximately 0.2637 mrad/pixel.

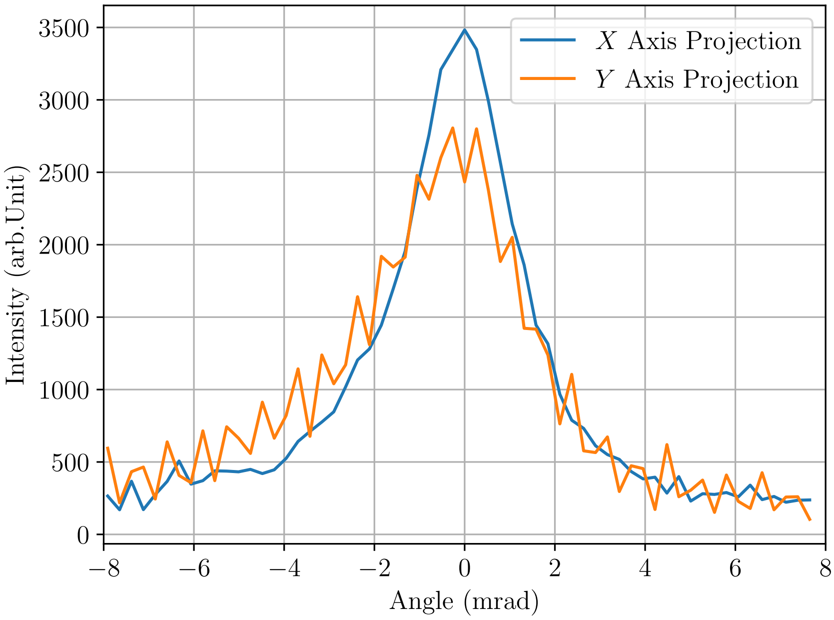

Figure 4.15: Vertical and horizontal projections of the OTR angular distribution from Fig. 4.12.

4.5.2 Cherenkov Diffraction Radiation System Setup

The focal plane for the imaging and angular stages were found by focusing the optical system on the ChDR target holder and by using the back focal plane location used for the OTR screen. To align the rotation of the ChDR emission, raster scans were performed by adjusting the vertical tilt of the optical system's top mirror and the lateral stage. By mapping out the space by adjusting the lateral stage and then sweeping up and down with the tilted mirror the optimal set of stage positions where the entire distribution could be seen are shown in Table. 4.3.

Stage	Measurement Position
Linear Stage: Optical Axis (Imaging)	74 mm
Linear Stage: Optical Axis (Angular)	96 mm
Mirror Tilt Stage: Periscope	6 mm
Linear Stage: Lateral Axis	−30 mm
Rotation Stage: ChDR Target Rotation	76.85°
Translation Stage: ChDR Target Insertion	−70.5 mm

Table 4.3: ChDR experiment optimal stage positions.

Figure 4.16 shows the ChDR radiator emission imaged using the optical system from Fig. 3.17 and the imaging parameters from Table. 4.3. In the centre of the image the distinct rectangular shape of ChDR target can clearly be seen.

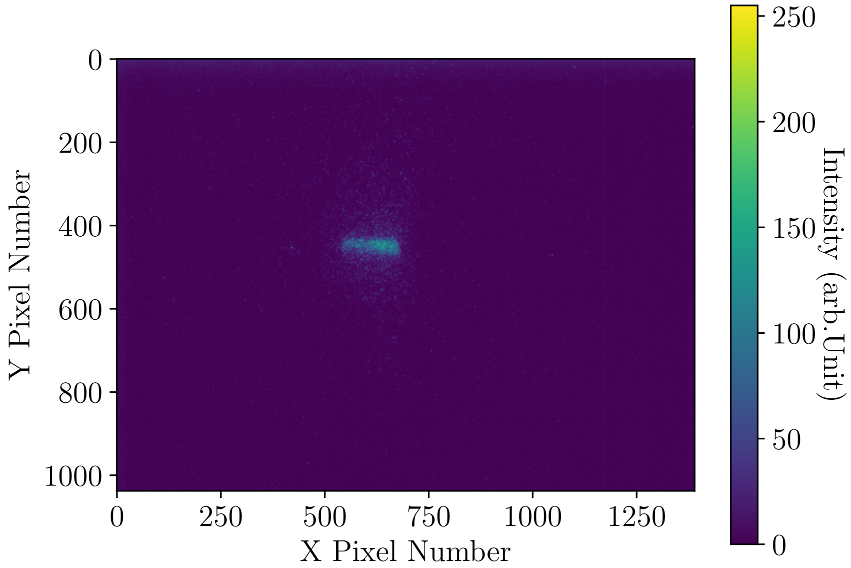

Figure 4.16: Example ChDR emission image, taken using the imaging parameters from Table. 4.3 and an impact parameter of approximately 2.5 mm.

Figure 4.17 shows the ChDR angular distribution measured from the optical system in Fig. 3.17 using the angular parameters from Table. 4.3. With this optical system the angular distribution has been compressed down allowing for the measurement of the entire angular distribution, where this has been confirmed by using the lateral and tilt stages.

4.6 Photomultipler Tube Commissioning

As described in Sec. 3.2.5 the PMT system has been characterised using the same optical system as the ProxiVision camera, however the DAQ system for the PMT is different and must be commissioned. The PMT DAQ system has different sample rates available. The system acquires data at 125 MHz with a buffer size of 16384 samples [62]. The acquired signal can be automatically decimated reducing the effective sampling rate but increasing the buffer length. Table 4.4 shows the different decimating settings and the corresponding sample rates and buffer lengths.

When commissioning the PMT the beam was setup to extract single bunches at a rate of 1 Hz. Figure 4.18 shows the measured signal when using a decimation of 65536, giving a buffer length of 8.590 s. There are nine clear signal spikes corresponding to the bunches that are extracted with the beam, given the extraction rate this is expected showing there is beam

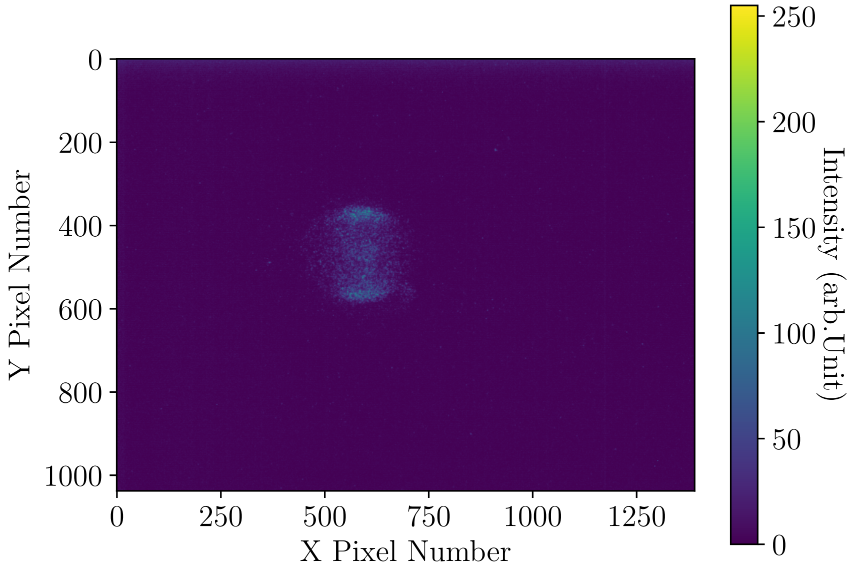

Figure 4.17: Example ChDR angular distribution, taken using the angular parameters from Table. 4.3 and an impact parameter of approximately 2.5 mm.

Decimation	Sampling rate	Buffer Length
1	125 MS/s	131.072 µs
8	15.6 MS/s	1.049 ms
64	1.953 MS/s	8.389 ms
1024	122.07 kS/s	134.218 ms
8192	15.258 kS/s	1.074 s
65536	1.907 kS/s	8.590 s

Table 4.4: Red Pitaya decimation settings with corresponding sample rates and buffer lengths [62].

induced signal.

A higher sampling rate is preferable to accurately measure the shape of the beam induced signal on the PMT. Figure 4.19 shows the acquired PMT data using the same setup as in Fig. 4.18 with decimation factor of 1. The peak signal is much higher as the improved sampling rate is fast enough to measure the signal before it decays. When the Red Pitaya is triggered with the beam extraction in the longer trace there is one peak per extraction. This adds confidence to say that the signal measured in Fig. 4.19 is the beam induced PMT response.

In order to extract a signal from the PMT trace in Fig. 4.19 the signal noise needs to be normalised. Using the same method as the IBPM a mean of the samples before the peak is

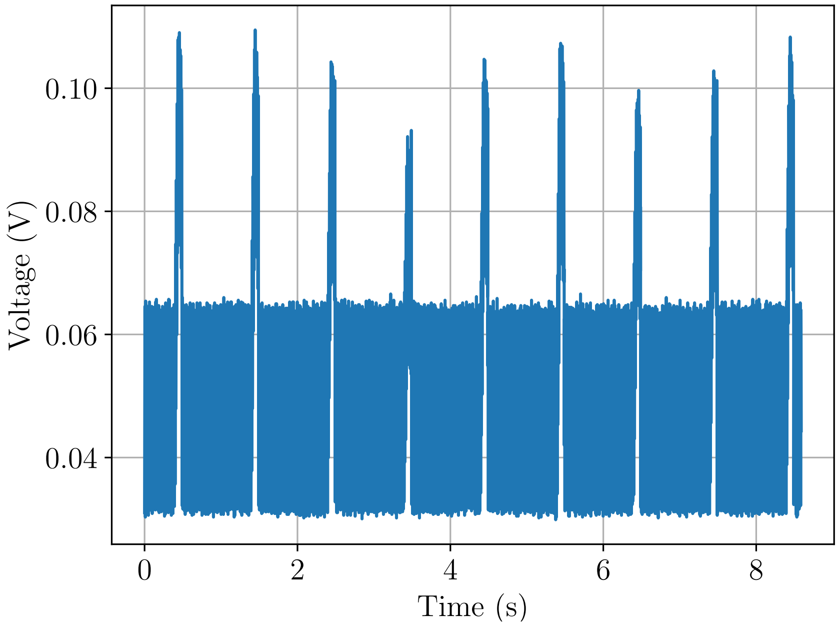

Figure 4.18: PMT signal measured with decimation of 65536 yielding an effective sampling rate of approximately 1.9 kHz.

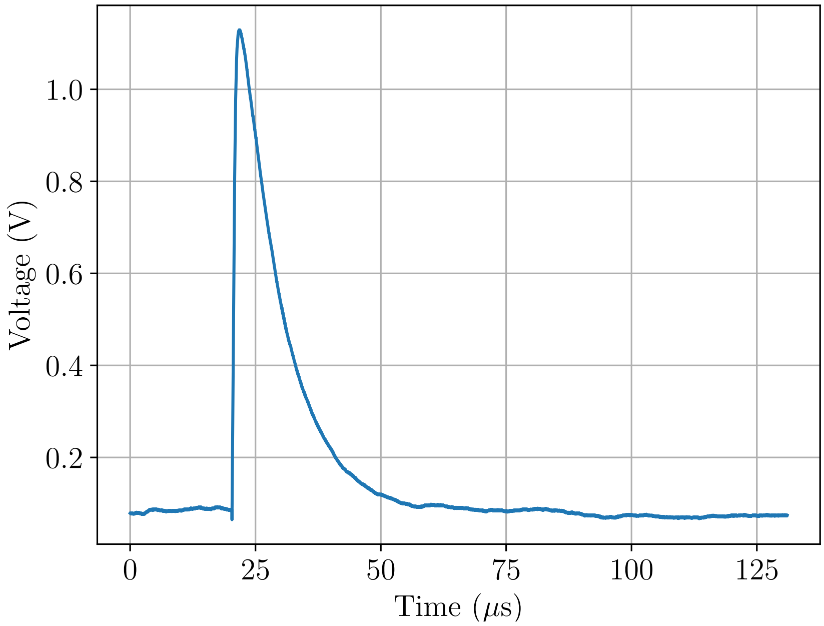

Figure 4.19: PMT signal measured with decimation of 1 yielding an effective sampling rate of 125 MHz.

induced and the mean is subtracted from the entire signal. An integration window can then be set around the signal to produce a single magnitude for the entire trace.

Figure 4.20 shows the same trace as in Fig. 4.19 with a −0.08 V noise offset applied and a 20 µs integration window visible. By measuring a number of different PMT signal traces and integrating them with the same window, the signals can be used under different beam parameters to build beam response scans such as impact parameter or wavelength.

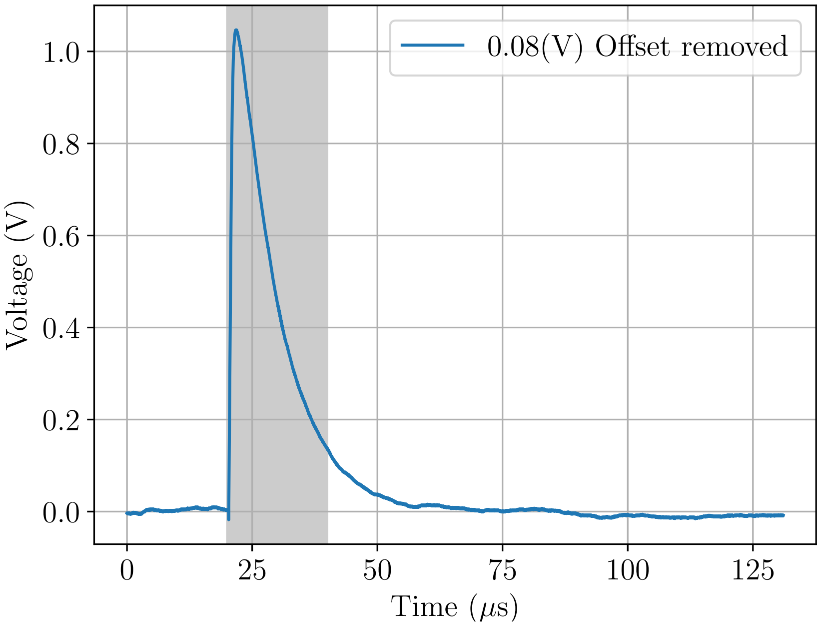

Figure 4.20: PMT signal measured with decimation of 1 with a −0.08 V offset applied and a 20 µs integration window visible as the shaded region.

CHAPTER 5

CHERENKOV DIFFRACTION RADIATION SIMULATIONS

To predict the emission of ChDR from a dielectric radiator a number of simulation codes have been developed. Currently under investigation are several experimental regimes including coherent, incoherent, and plasmonic. The coherent regime examines ChDR wavelengths that are longer than the bunch length of the charged particle beam. These experiments are primarily performed at CLEAR where the bunch lengths can reach $< 1\,\text{ps}$ [64]. The incoherent studies such as those being performed on the Diamond BTS are exploring the optical and IR regions of ChDR emission. For the Diamond bunch length there are no coherency effects at optical and IR wavelengths, therefore traditional photo detection systems that are well known at accelerator laboratories can be used [65]. Plasmonic experiments are also conducted at CLEAR, these explore how using metallic coatings on the radiators can induce surface plasmonic resonances increasing the ChDR yield [66].

As the regimes under examination are broad, several simulation methods are being used to cover different requirements. Three simulation methods are currently being explored: numerical PCA simulations, using ImpedanceWake2D (IW2D), and CST Studio Suite [67]. PCA consists of analytical equations present in [30], where Python codes have been developed for this thesis to simulate the PR emission. IW2D is an analytical code framework developed at CERN that can compute the electromagnetic fields, the resistive wall impedance, or the wake functions for multilayered flat, cylindrical or elliptical structures [67, 68]. CST Studio Suite is an off-the-shelf Finite Element Analysis (FEA) electromagnetic simulation package that can simulate full three dimensional geometries [69]. For this thesis only PCA is considered as this is the theory that has been developed with optical wavelengths in mind.

5.1 Polarisation Currents Approach Simulation Codes

5.1.1 Polarisation Currents Approach Simulation Framework

A software framework has been developed to simulate the expected ChDR response using the PCA model. The main calculations performed with this framework are single particle angular distributions for a given wavelength, impact parameter, beam energy, solid angle component, and ChDR radiator geometry. For the prismatic radiator, these distributions are given by Eq. 2.14 and 2.15.

A spectrum for each angular distribution is calculated by integrating over the solid angle component in Eq. 2.17. By varying a single parameter, scans can be obtained such as, wavelength dependence and impact parameter dependence.

Figure 5.1 shows a simplified Unified Modelling Language (UML) diagram for the PCA framework that has been developed in Python 3.7. In order to make the framework more scalable and modular a generic template class of `ChDR_Target` is defined with the methods necessary for calculating impact parameter scans, wavelength scans, and angular distributions. The exact angular distribution implementations for different geometries, such as `ChDR_Prism`, are implemented in child classes of `ChDR_Target`. This is done by overriding the private abstract methods `_angular_distribution_single_horizontal` and `_angular_distribution_single_vertical` in each child class. For the prismatic geometry class, `ChDR_Prism`, these methods are where Eq. 2.14 and 2.15 are implemented. Designing the framework this way makes it expandable, if an angular distribution is produced for a new type of geometry, a new child class for that geometry is created and the functionality of the `ChDR_Target` class will be inherited.

Methods are included in the PCA simulation framework to simplify the process of plotting the output scans and saving the datasets. Each scan creates an instance of one of the classes, `Angular_Distribution`, `Impact_Scan` or `Wavelength_Scan`, contained in the private data for these classes is the parameters used to create them. Each instance of the scan classes is then saved into the private data of the `ChDR_Target` child. The single class instance can be saved to a file, allowing for the grouping and plotting of large data sets using the methods contained in `ChDR_Target`.

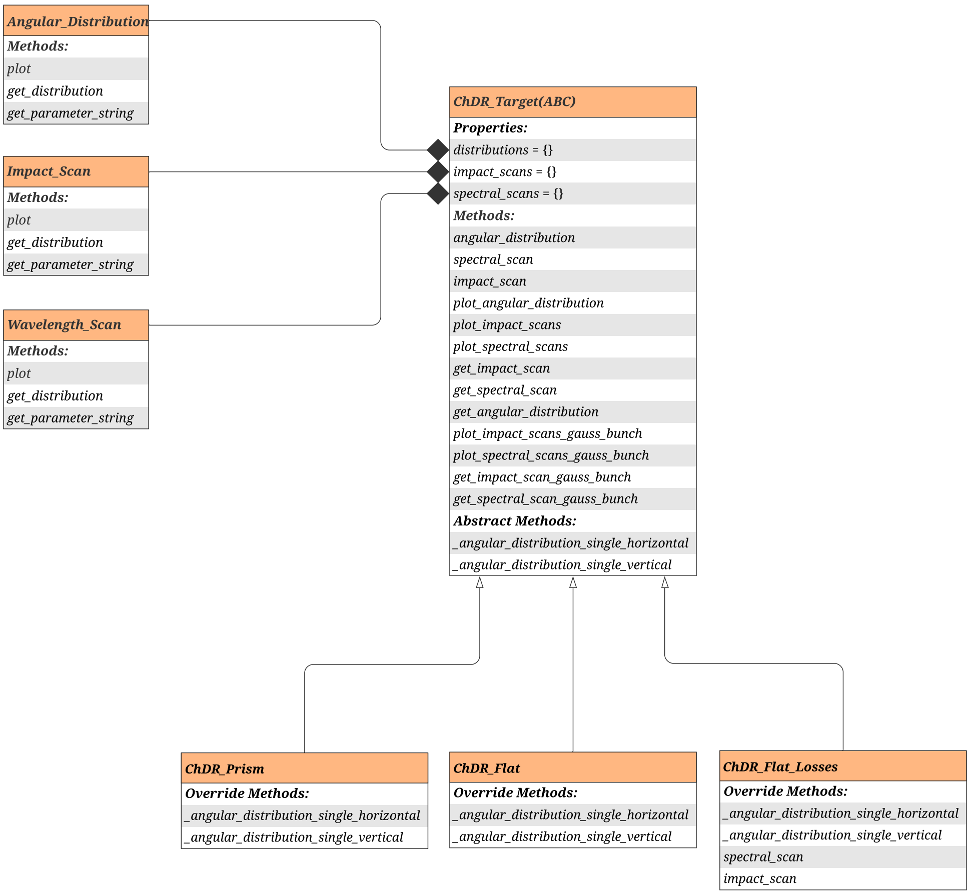

Figure 5.1: Reduced UML diagram for PCA simulation codes.

5.1.2 Base Functionality

The base functionality of the PCA simulation framework produces single particle responses of ChDR angular distributions, spectral dependences, and impact parameter dependences. Figure 5.2 shows the photon spectrum produced at different impact parameters for a 3 GeV electron travelling parallel to a 10 mm long prismatic fused silica radiator. The radiator simulated here has a vertex angle of 30°, a relative permittivity 2.1, and thus a of fixed index of refraction of approximately 1.45 as

$$\varepsilon = n^2, \tag{5.1}$$

where ε is the relative permittivity and n is the index of refraction. The solid angle has the component values of $\mathrm{d}\phi = 0.16°$, $\mathrm{d}\theta = 0.01°$ yielding a $\mathrm{d}\Omega$ of 3.13×10^{-11} sr. The different impact parameters on the graph are represented by b, where $b = h\cos(\delta)$, using the notation from Fig. 2.7.

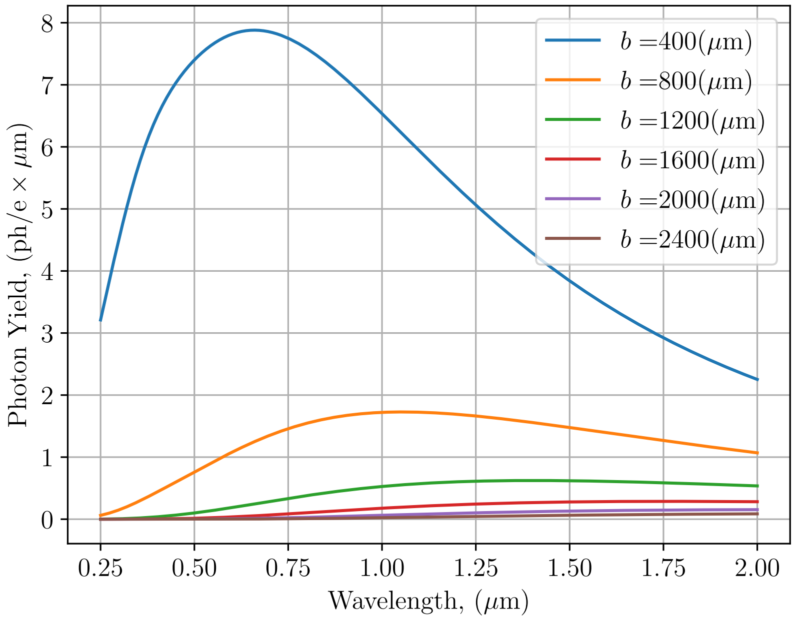

Figure 5.2: ChDR spectral dependence simulated for a 3 GeV electron moving parallel to a 10 mm long fused silica prismatic radiator.

The magnitude of the spectrum obtained in Fig. 5.2 is many orders of magnitude lower than those obtained in Eq. 2.6 using the dielectric pipe radiator. The reason for this is that although each radiator is the same length, the pipe radiator intercepts the full transverse field around the particle, whereas the ChDR radiator used in this experiments only intercepts a fraction of the transverse field.

Figure 5.3 shows the spectral dependence at an impact parameter of 0.8 mm for multiple radiator lengths keeping all other radiator parameters the same. This shows that increasing the radiator length produced a largely flat increase in the emission for all wavelengths presented in Fig. 5.3.

Fixing the wavelength and varying the impact parameter produces an impact parameter dependence. Figure 5.4 shows the photon yield produced at specific wavelengths and for different impact parameter from the same radiator and beam parameters used in Fig. 5.2. At very low impact parameters, the photon yield is larger at shorter wavelengths. At longer impact parameters the photon yield is larger at longer wavelengths. This is in agreement with the discussions in Sec. 2.3.

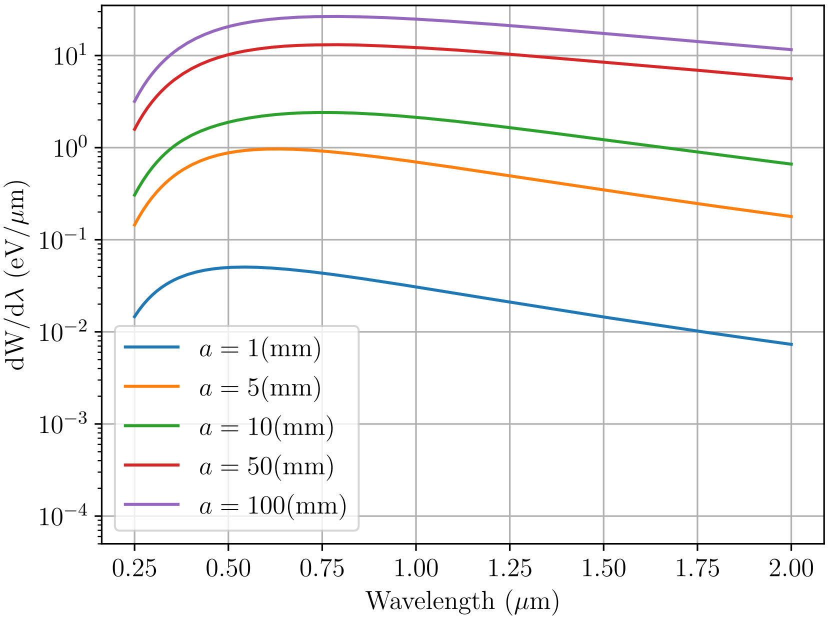

Figure 5.3: ChDR spectral dependence simulated for multiple lengths of fused silica prismatic radiators for a 3 GeV electron moving parallel the radiator with an impact parameter of 0.8 mm.

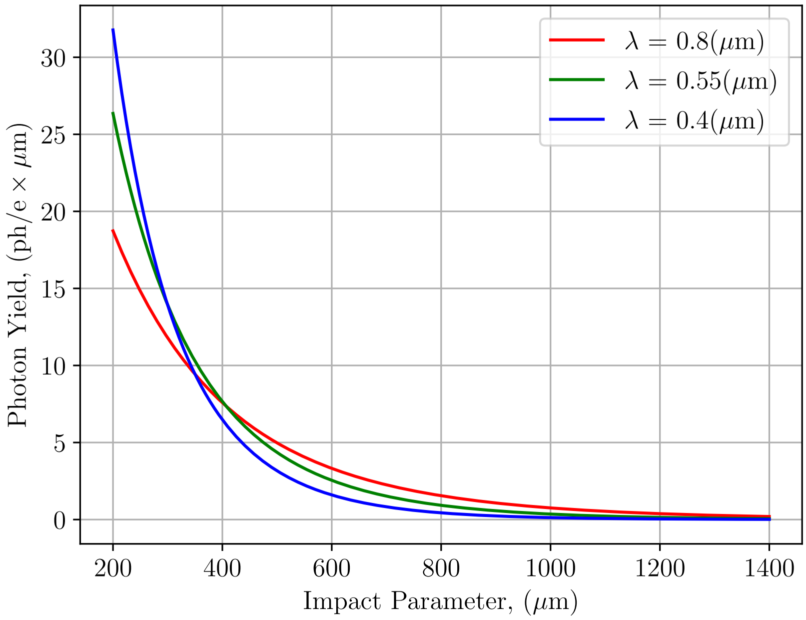

Figure 5.4: ChDR impact parameter dependence simulated for a 3 GeV electron moving parallel to a 10 mm long fused silica prismatic radiator.

5.1.3 Additional and Advanced Features

As a first approximation the single particle responses for radiators with a fixed permittivity are sufficient in order to understand the relative ChDR behaviour. In order to take into account more effects when performing an experiment additional and advanced features have been added to the framework.

Radiator materials have a wavelength dependent relative permittivity and refractive index. For these materials the Cherenkov angle and radiation emission angle are wavelength dependent (see Eq. 2.2). In order to account for this, the `ChDR_Target` class can be provided with a file that states relative permittivity and/or refractive index at different wavelengths in order to account for this in the simulations.

The impact parameter scans produced from the base framework use a fixed wavelength. This is only a valid representation for experiments that use a bandpass filter, where the simulation framework assumes a bandpass filter with a perfect quality factor. To more accurately simulate an experimental setup both the transverse beam size, and the detector quantum efficiency are taken into account. The `ChDR_Target` class can be provided with a file stating the detector quantum efficiency and a transverse beam charge distribution. These are used when producing an angular distribution, wavelength scan or impact parameter scan.

Figures 5.5, 5.6 and, 5.7 have been produced to demonstrate how the simulation codes can account for a wavelength dependent relative permittivity. Table 5.1 shows the parameters used for these simulations.

Simulation Parameter	Value
Electron energy	3 GeV
Electron energy γ	5871
Target length a	10 mm
Vertex angle of the prism φ	30°
Impact parameter b	1 mm
Dielectric permittivity $\varepsilon(\lambda)$	$\frac{\lambda[\mu\mathrm{m}]}{10} + 1.95 \; \left\{0.5[\mu\mathrm{m}] \leq \lambda \leq 0.6[\mu\mathrm{m}]\right\}$

Table 5.1: Simulation parameters used for Fig. 5.5, 5.6, and 5.7.

Figure 5.5 shows the vertical and horizontal polarisations of the single particle ChDR angular distributions generated at a wavelength of 0.5 µm. At the wavelength of 0.5 µm the prism simulated has a relative permittivity of 2.0, this yields an extracted polar Cherenkov angle of approximately 38.53° (see Eq. 2.2). When using the parameters from Table. 5.1 and a wavelength of 0.6 µm the relative permittivity is increased to 2.01. The result of increasing the relative permittivity is that the extraction angle from the prism changes from approximately 38.53° to 38.68°.

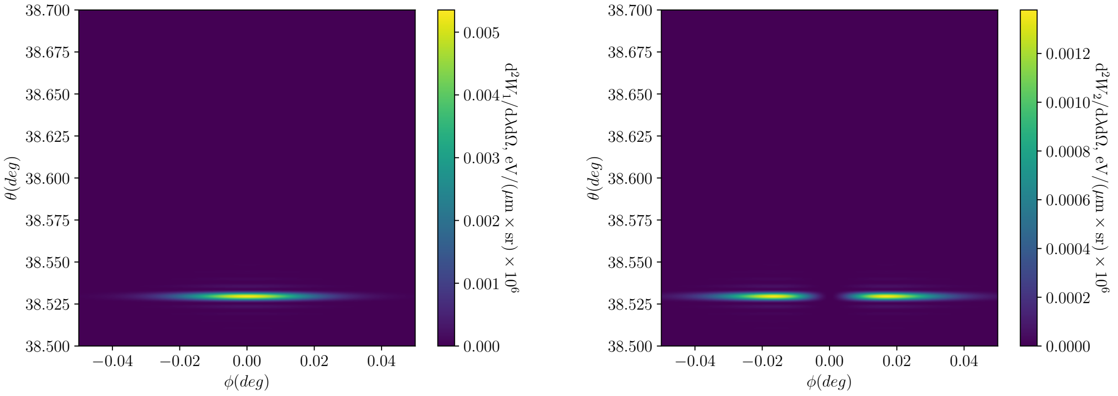

(a) Vertical polarisation. **(b)** Horizontal polarisation.

Figure 5.5: Simulated PCA angular distributions generated at a wavelength of 0.5 µm and parameters from Table. 5.1.

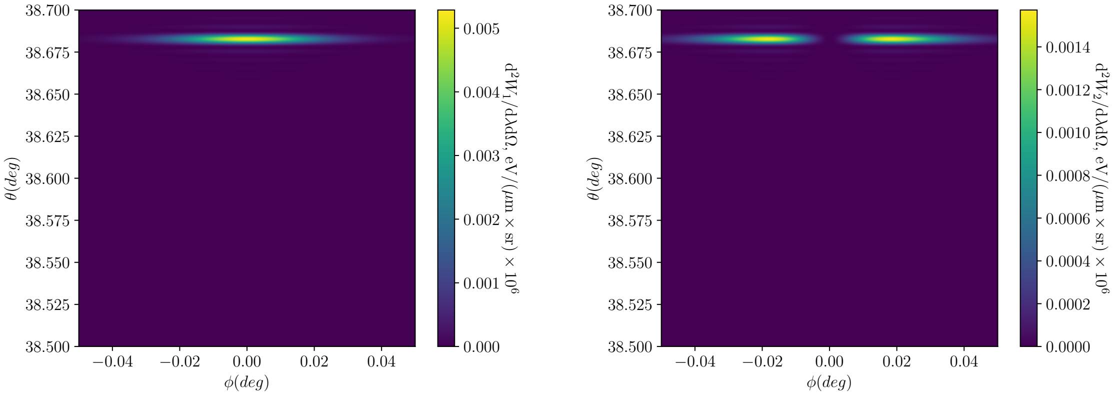

(a) Vertical polarisation. **(b)** Horizontal polarisation.

Figure 5.6: Simulated PCA angular distributions generated at a wavelength of 0.6 µm and parameters from Table. 5.1.

Figures 5.5 and 5.6 are displayed with the same axis limits to clearly show how the change in relative permittivity can affect the emission angle. The PCA simulation framework can integrate over multiple parameters such as wavelength or impact parameter. By varying dependent parameters such as relative permittivity, or by scaling the output depending on sensitivity, the simulations can more accurately replicate the experimental parameters where a series of wavelengths are captured at once or where a beam distribution is considered.

Figure 5.7 uses the simulation parameters listed in Table. 5.1 where the simulation has been integrated with respect to the wavelength using the limits 0.5 and 0.6 µm. The wavelength dependent relative permittivity creates a clear smearing effect from the angular distributions shown in Fig 5.5 and 5.6.

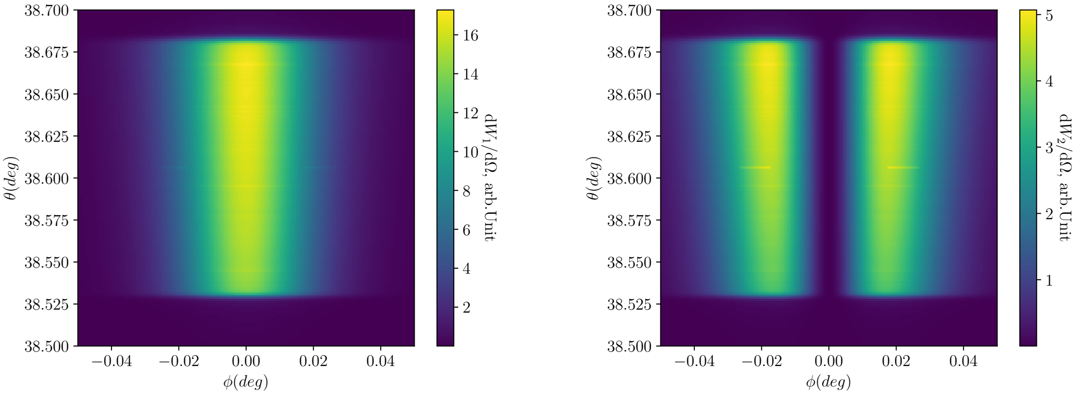

(a) Vertical polarisation. **(b)** Horizontal polarisation.

Figure 5.7: Simulated PCA Angular distributions integrated over the wavelengths 0.5 to 0.6 µm using parameters from Table. 5.1.

When performing experimental angular distribution measurements there are multiple smearing effects caused by a change in permittivity, the transverse beam profile, and the detector quantum efficiency.

5.2 Diamond Beam Test Stand Simulation Set

Using the PCA simulation framework, simulations have been performed for the Diamond BTS. The radiator installed on the Diamond BTS is an accumulation radiator described in Sec. 3.2 and shown in Fig. 3.7. There is no PCA model for the accumulator radiator so the prismatic radiator model is used where the simulations have the same permittivity, length, and vertex angle of the accumulator radiator. As the parameters are the same between the two radiators it is thought that qualitatively the simulations from one radiator should match the other. The prismatic simulation parameters used in this section have been summarised in Table. 5.2.

Simulation Parameter	Value
Electron energy	3 GeV
Electron energy γ	5871
Target Length a	15 mm
Vertex angle of the prism φ	12.5°
Dielectric permittivity $\varepsilon(\lambda) = \varepsilon$	5.76

Table 5.2: Diamond BTS simulation parameters.

The simulation codes can account for absorption in the material by using a complex number for the relative permittivity. Due to the stability of diamond in the visible and Near-Infrared (NIR) wavelengths, for these simulations the relative permittivity has been set fixed as 5.76.

The simulations produced here have limitations, for example, the vertical height of the radiator used in the BTS is 2 mm. As detailed in Sec. 3.2.1 the radiator should be much larger than this given the effective electron radius and the vertical beam height. Not taking this into account could result in vast differences between experiments and simulations. The relative permittivity does vary over the simulated range for CVD diamond but as these deviations of the relative permittivity are relatively minor they are not taken into account [70]. Finally given that the simulations are based on the PCA model, the simulations will inherit all of the limitations of the PCA model itself; these limitations are described in Sec. 2.1.

5.2.1 Visible Wavelength Simulations

The optical system in the BTS was initially fitted with a filter wheel loaded with bandpass filters with central wavelengths of 0.4 and 0.55 µm. Figures 5.8 and 5.9 show the vertical and horizontal polarisation of the ChDR angular distribution created from the BTS radiator by a 3 GeV electron at an impact parameter of 5 mm at the wavelengths of 0.4 and 0.55 µm respectively. The peak intensity is several orders of magnitude higher for the longer wavelength of 0.55 µm than for 0.4 µm. The overall shape of the distribution appears largely unchanged between the two wavelengths, but is slightly broader at 0.55 µm. The actual measured angular distribution will have a smearing effect from the beam of particles at a range of different impact parameters.

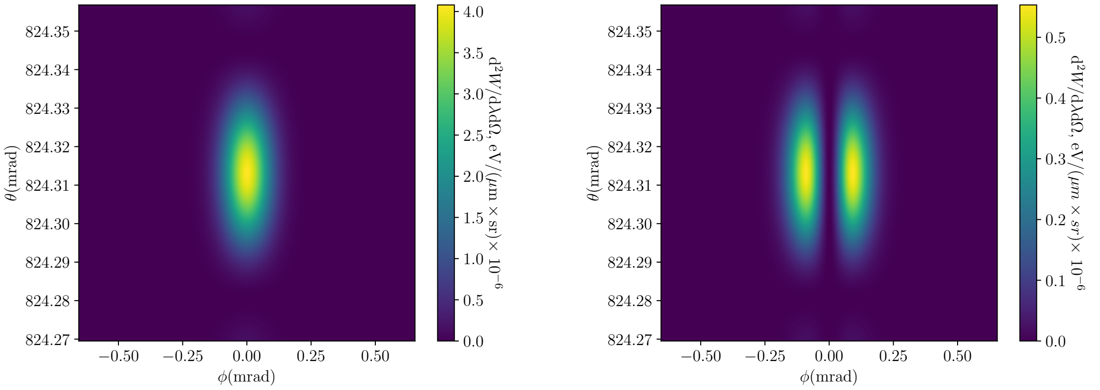

(a) Vertical polarisation. **(b)** Horizontal polarisation.

Figure 5.8: Single particle PCA angular distributions, simulated for the wavelength of 0.4 µm, impact parameter of 5 mm and parameters from Table. 5.2.

Projections are taken from simulated angular distributions so that the distribution shape and evolution can be more easily compared. Figure 5.10 shows the simulated PCA projections at an impact parameter of 1 mm for ChDR that is, unpolarised, vertically polarised, and horizontally polarised, at the wavelengths 0.4 and 0.55 µm. Examining Fig. 5.10a all of

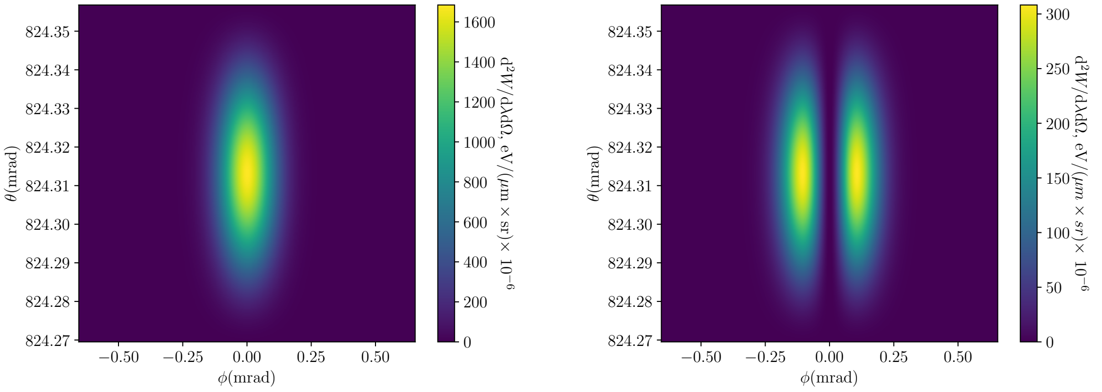

(a) Vertical polarisation **(b)** Horizontal polarisation

Figure 5.9: Single particle PCA angular distributions, simulated for the wavelength of 0.55 µm, impact parameter of 5 mm and parameters from Table. 5.2.

the projections have a similar shape, where the vertical projections for both wavelengths have a broader shape and higher amplitude than the corresponding horizontal projection. A key difference is that as the wavelength gets longer the difference between the vertical and horizontal projections become smaller: the results of each polarisation for a wavelength of 0.55 µm in Fig. 5.10a are hard to differentiate, whereas for the 0.4 µm results the difference between the two polarisations is clear.

Examining Fig. 5.10b the projections have higher amplitudes and broader distributions for the 0.55 µm results, similar to Fig. 5.10a. Conversely to Fig. 5.10a the shape of the projections between the two individual polarisations is different: the vertical display a Gaussian shape whereas the horizontal have a double bump shape. Additionally the difference between the two projections does not appear to change when moving to the longer wavelengths in the same way between the two wavelengths in Fig. 5.10.

Figure 5.11 is computed for the the same polarisations and wavelengths as Fig. 5.10 but for an impact parameter of 2 mm. Much of the analysis for Fig. 5.10 applies to these graphs with the main difference being the degree of the differences.

Figure 5.12 shows the single particle spectrum at a range of impact parameters for the Diamond BTS as predicted by the PCA model. At short impact parameters (1 and 100 µm) the spectrum follows the CR spectral dependence of $1/\lambda$, whereas for the longer impact parameters the intensity increases with longer wavelengths. In order to confirm that the signal is generated from the beam core, and not the beam halo the impact parameter must be large enough that the beam follows a ChDR spectral dependence where the intensity grows with wavelength and not the inverse that is similar to the CR dependence.

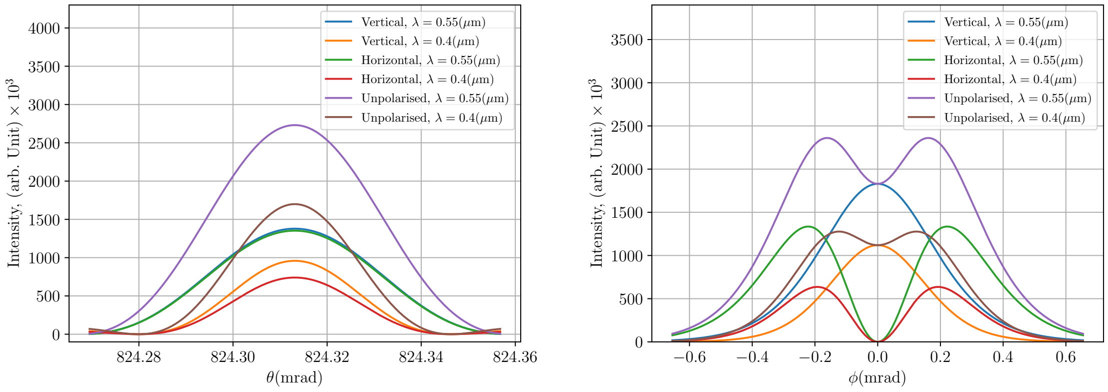

(a) Projection of ϕ onto θ axis.

(b) Projection of θ onto ϕ axis.

Figure 5.10: Single particle PCA angular distribution projections, simulated for an impact parameter of 1 mm and parameters from Table. 5.2.

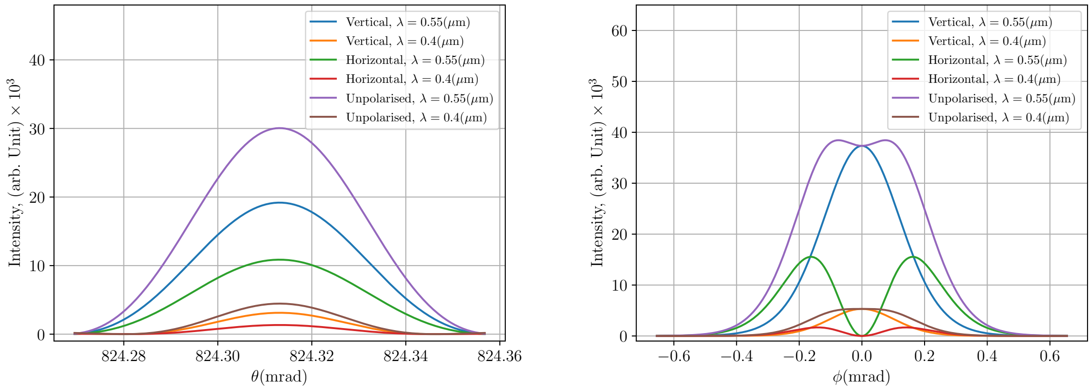

(a) Projection of ϕ onto θ axis.

(b) Projection of θ onto ϕ axis.

Figure 5.11: Single particle PCA angular distribution projections, simulated for an impact parameter of 2 mm and parameters from Table. 5.2.

As discussed in Chap. 2 increasing the radiator length will result in the generation of more ChDR. Figure 5.13 shows the single particle PCA spectrum generated at an impact parameter of 1 mm and using the parameters from Table. 5.2 apart from the target length. By increasing the target length the emission yield is increased almost uniformly across all wavelengths presented.

As the polarisations are calculated individually in the PCA framework, impact parameter or spectral scans can be produced for the individual polarisations. Figure 5.14 shows the impact parameter response for the individual polarisations at the wavelengths 0.4 and 0.55 µm and the parameters in Table. 5.2. Although the peak ChDR emission comes from the vertical polarisation, when integrating over the angular distribution at very low impact parameters the emission from horizontal polarisation appears larger. This is not believed to be a real effect

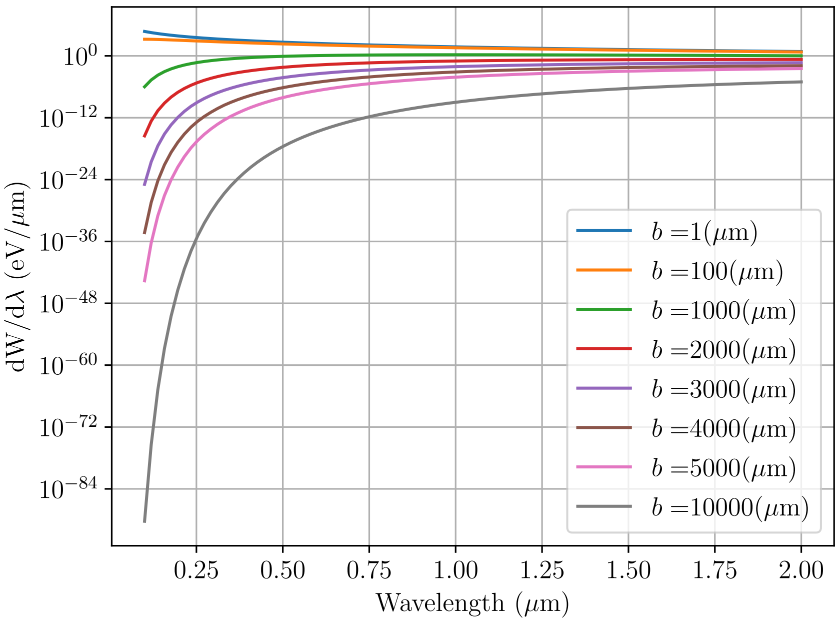

Figure 5.12: Single particle PCA spectrum calculated for different impact parameters using parameters from Table. 5.2 and polar solid angle component, dθ, of 0.175 mrad, and azimuthal, dϕ, of 2.793 mrad.

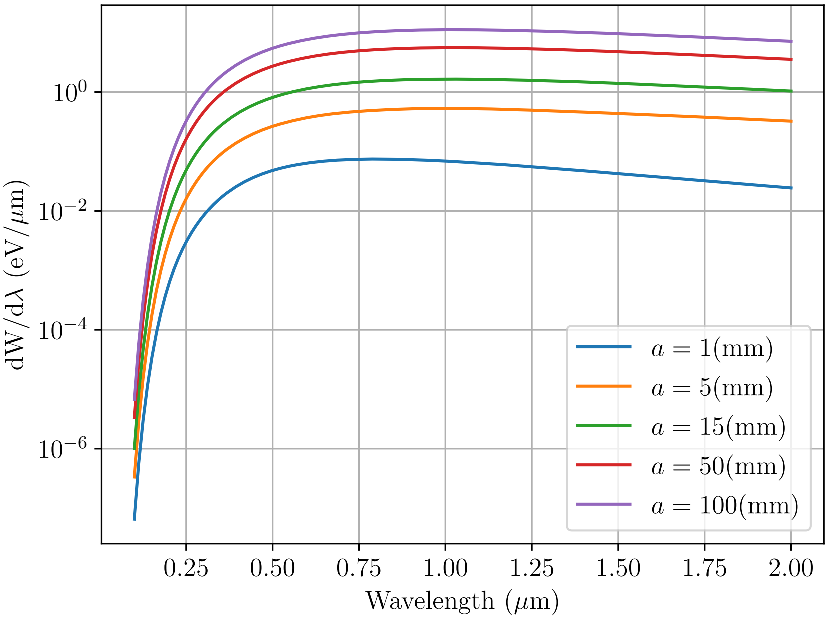

Figure 5.13: Single particle PCA spectrum calculated for different target lengths at an impact parameter of 1 mm using the parameters from Table. 5.2 and polar solid angle component, dθ, of 0.175 mrad, and azimuthal, dϕ, of 2.793 mrad.

but an error caused when integrating at such low impact parameters where the distribution shape is broad and not fully captured by the solid angle components.

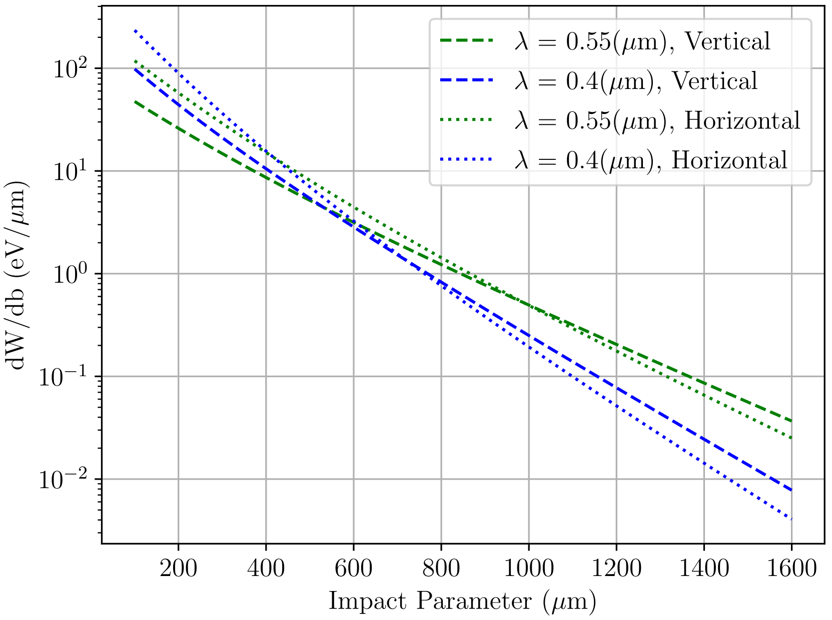

Figure 5.14: Single particle PCA impact parameter scan for individual polarisations for the wavelengths 0.4 and 0.55 µm using the parameters from Table. 5.2.

Figure 5.15 shows the unpolarised impact parameter scan, produced using the parameters found in Table. 5.2. The 0.4 µm wavelength response in Fig. 5.15 is higher at low impact parameters, whereas the 0.55 µm wavelength is higher at large impact parameters, with a transition between the two at the impact parameter of approximately 460 µm.

Figure 5.15 shows that the intensity of ChDR emission has a non-linear response when varied over the impact parameter. The non-linear response of the ChDR pickup means that the working region of the BPM must be strongly considered during the design. A BPM measuring incoherent ChDR with a detection system designed for the central region would be quickly saturated by particles close to the pickup, or conversely, if the detection system was designed for the region by the pickup it would not be sensitive to fluctuations in the centre.

The pickup response is high at low impact parameters and requires the beam size to be considered if it is not negligible when compared to the impact parameter. The Diamond BTS beam has a nominal horizontal beam size σ_x of 1.3 mm, where this can potentially be varied between 0.5 and 1.5 mm (see Sec. 4.3.2). Figure 5.16 shows three horizontal Gaussian bunch profiles each with a total charge of approximately 200 pC centred around the impact parameter of 5000 µm. The shaded region between 0 and 250 µm highlights the tails or halo of the beam distribution closest to the radiator, whereas the shaded region between 4000

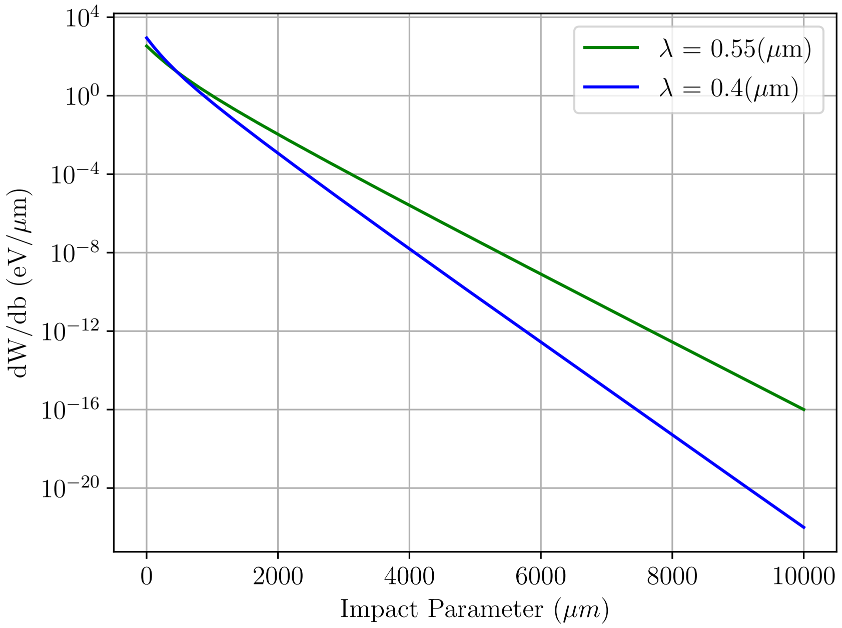

Figure 5.15: Single particle PCA impact parameter scan for the wavelengths 0.4 and 0.55 µm using the parameters from Table. 5.2.

and 6000 µm highlights the beam core. For these simulations a wide beam distribution is considered to account for beam halo in the same calculation, and no separate calculation of directly colliding particles that generate CR are taken into account. These are not considered as they do not form part of the desired measurement. It is also thought that these particles may slow down significantly when they enter the radiator, limiting the amount of direct CR generated.

Given the non-linear response of the detector it is important to know what parts of the beam produce the most signal on the detector. An ideal BPM will be sensitive to the core of the beam, and not the beam halo. The beam contribution can be simulated by multiplying the components of a beam profile distribution and impact parameter dependence. i.e. Fig. 5.16 and 5.15 respectively. Multiplying both of these graphs together gives the contribution signal at each respective position for each beam size and wavelength in the source graphs, this can be seen in Fig. 5.17.

Figure 5.17 shows emission intensity at each impact parameter. The dotted and dashed plots show the contribution for the the beam sizes of 1500 and 1000 µm respectively for the wavelengths of 0.4 and 0.55 µm. All four of these curves have the same generic shape where the highest value on the plot is at the lowest impact parameter. This shows that for the examined wavelengths the overall signal contribution for a beam with this distribution will come from the beam halo and not from the bulk of the beam. Conversely the two curves for

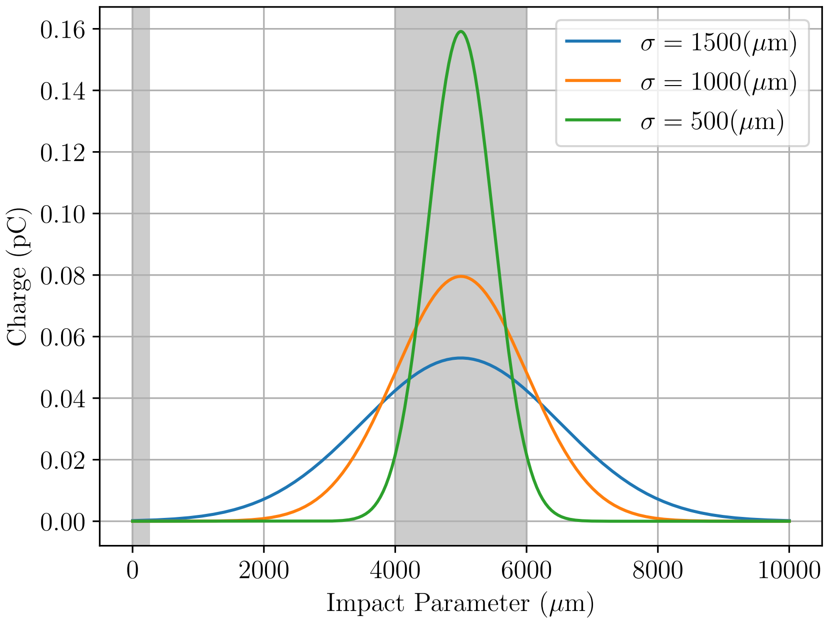

Figure 5.16: Transverse Gaussian bunch charge distribution over the impact parameter, centred at 5 mm. The shaded region between 0 and 250 µm highlights the halo of the distribution closest to the radiator, whereas the shaded region between 4000 and 6000 µm highlights the beam core.

the beam size of 500 µm have a peak value closer to the centre of the graph where the beam core is located.

As with Fig. 5.12 impact parameter and spectral response are heavily coupled for ChDR, the exact impact parameters that contribute to the signal is a very important consideration. The key conclusions from the simulations in Fig. 5.17 are that for a detector sensitive to wavelengths 0.4 or 0.5 mm, a nominal impact parameter of 5 mm, and horizontal beam size σ_x greater than 1 mm, the ChDR detector installed on the BTS would act as a beam halo monitor and not a beam position monitor.

When designing a ChDR BPM the measured wavelengths need to be specifically chosen for the beam size and impact parameter ranges used. This is to ensure that the system is sensitive to the bulk of the beam and not the beam halo. For the conditions on the Diamond BTS the sensitive wavelength ranges at larger impact parameters are in the IR region.

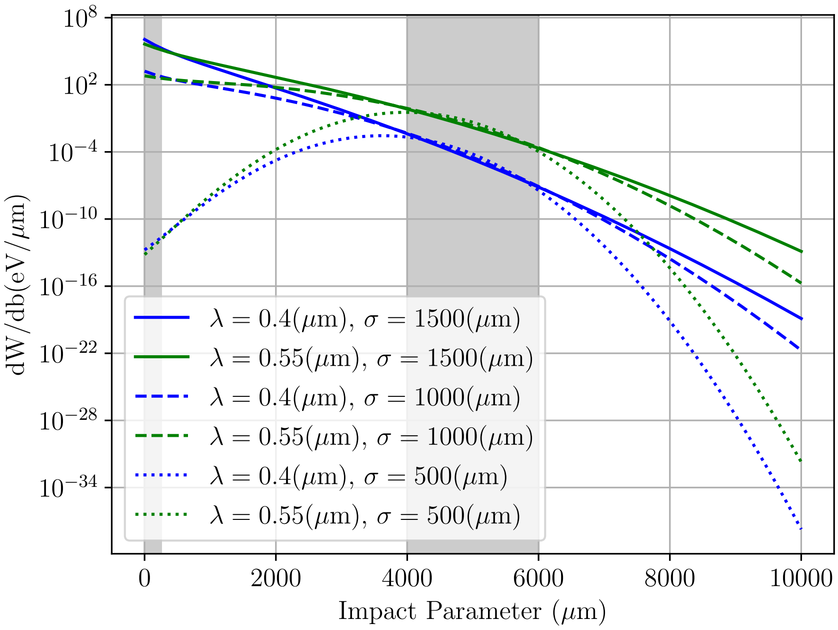

Figure 5.17: ChDR emission of 0.4 and 0.55 µm wavelengths at each impact parameter generated from the beam distributions shown in Fig. 5.16 and the parameters from Table. 5.2. The shaded region between 0 and 250 µm highlights the halo of the distribution closest to the radiator, whereas the shaded region between 4000 and 6000 µm highlights the beam core.

5.2.2 Infrared Wavelength Simulations

Figures 5.18 and 5.19 show the angular distributions that have been simulated for the Diamond BTS using the parameters found in Table. 5.2, the impact parameter of 5 mm, and the wavelengths of 1 and 5 µm respectively. All of the angular distributions in Fig. 5.8, 5.9, 5.18 and 5.19 have been displayed with same axis limits to show that the distribution is widening as the wavelength gets longer. In Fig. 5.19 the distribution is so large it shows if the angular acceptance of the optical system is too small, some of the signal will be missed from the measurement. It is worth noting that while the angular distribution appears large on these axes the overall distribution size is still considered narrow.

Figure 5.20 shows the single particle impact parameter response fixed at the visible wavelengths from the BTS bandpass filters and several IR wavelengths. As the impact parameter increases the signal is favoured by the longer wavelengths by several orders of magnitude. This explicitly shows why the measured wavelength is of great importance for a BPM system. It shows that if the objective was to design a beam halo monitor it could be done by measuring only very short wavelengths. The signal for all wavelengths on Fig. 5.20 is lower at a larger impact parameter. This does not take into account beam size that will increase the signal at the impact parameters where there are more particles.

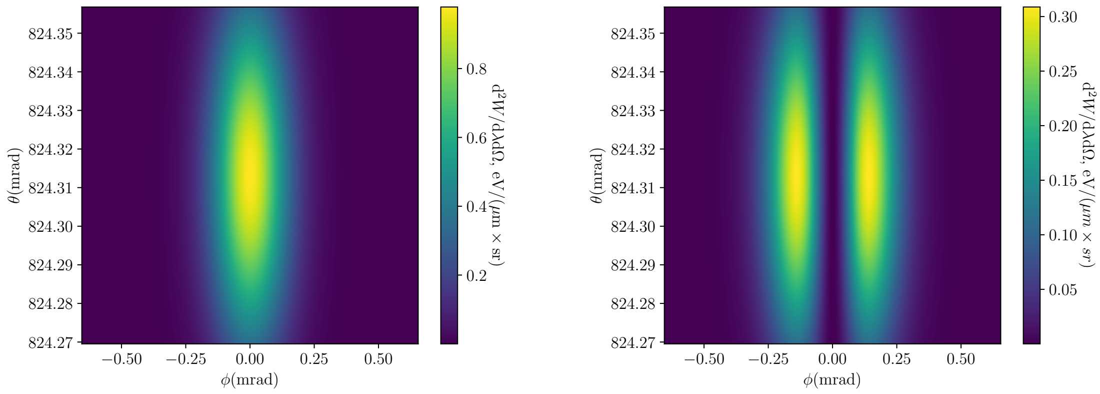

(a) Vertical polarisation.

(b) Horizontal polarisation.

Figure 5.18: Single particle PCA angular distributions, simulated for the wavelength of 1 µm, impact parameter of 5 mm and parameters from Table. 5.2

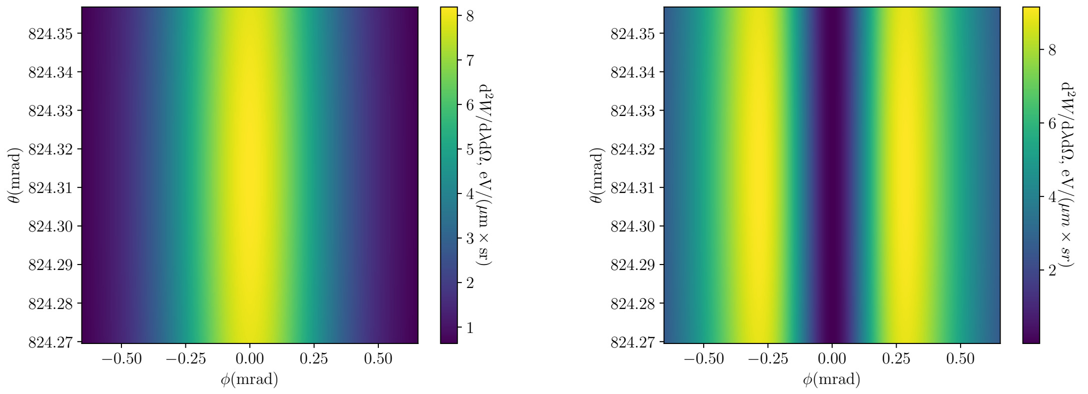

(a) Vertical polarisation.

(b) Horizontal polarisation.

Figure 5.19: Single particle PCA angular distributions, simulated for the wavelength of 5 µm, impact parameter of 5 mm and parameters from Table. 5.2.

To analyse how the beam distribution will affect the photon yield for each wavelength in Fig. 5.20 the three beam profiles from Fig. 5.16 are used. To obtain the signal contribution at each impact parameter for the different beam profiles and wavelengths the bunch profiles in Fig. 5.16 are multiplied across the impact parameter axis of each wavelength shown in Fig. 5.20. The results are displayed in Fig. 5.21, 5.22, and 5.23.

Figure 5.21 shows the beam signal contribution at each impact parameter for each wavelength, a beam centred at an impact parameter of 5 mm and a beam size σ_x of 1500 µm. The distributions are a combination of the Gaussian bunch profile and the exponential decay of the single particle impact parameter response. The results that resemble the exponential decay such as 0.4, 0.55, and 1 µm would act more as a beam halo monitor than a BPM for a beam of this size. Ideally for a BPM the primary signal contribution will come from the

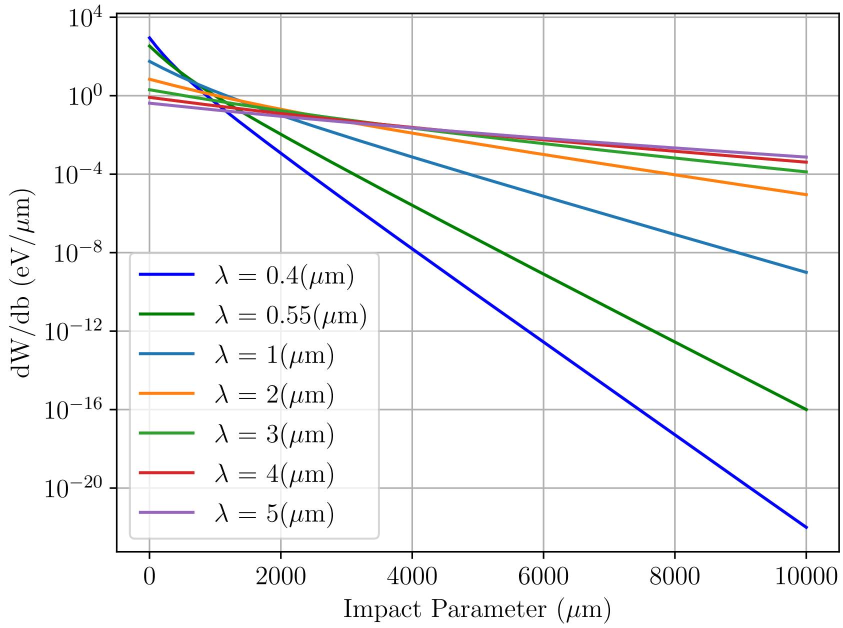

Figure 5.20: Single particle PCA impact parameter scan for visible and IR wavelengths using the parameters from Table. 5.2

same impact parameter location as the beam core, 5 mm. Even for the longest wavelengths examined the peak is at approximately 3 mm with a strong contribution from the beam halo.

Figure 5.22 shows the same analysis as Fig. 5.21 where the beam has a σ_x size of 1000 µm. Even with a smaller beam size the short wavelengths of 0.4 and 0.55 µm still peak at the very short impact parameters and are halo dominated. The longer wavelengths $>$ 3 mm peak at the impact parameter of approximately 4 mm, this is closer to the desired central beam location of 5 mm but there is still considerable signal contribution from the low impact parameter ranges.

Figure 5.23 displays the same process as Fig. 5.21 and 5.22 where the 500 µm beam size from Fig. 5.16 has been used. In comparison to the other bunch profiles the signal contribution for all plots in Fig. 5.23 are dominated by the core of the beam, so measuring the wavelengths examined for this beam would act primarily as a beam position monitor and not a beam halo monitor. The peak of the plots progressively moves closer towards 5 mm with longer wavelengths, where even a wavelength of 1 mm has a peak of approximately 4.2 mm with greatly reduced signal contribution from the beam halo.

While Fig. 5.23 shows that all wavelengths examined for that simulation are dominated by the beam core, it is important to remember that this is only for that specific beam size at that specific impact parameter. Moving the beam closer to the radiator increases the signal

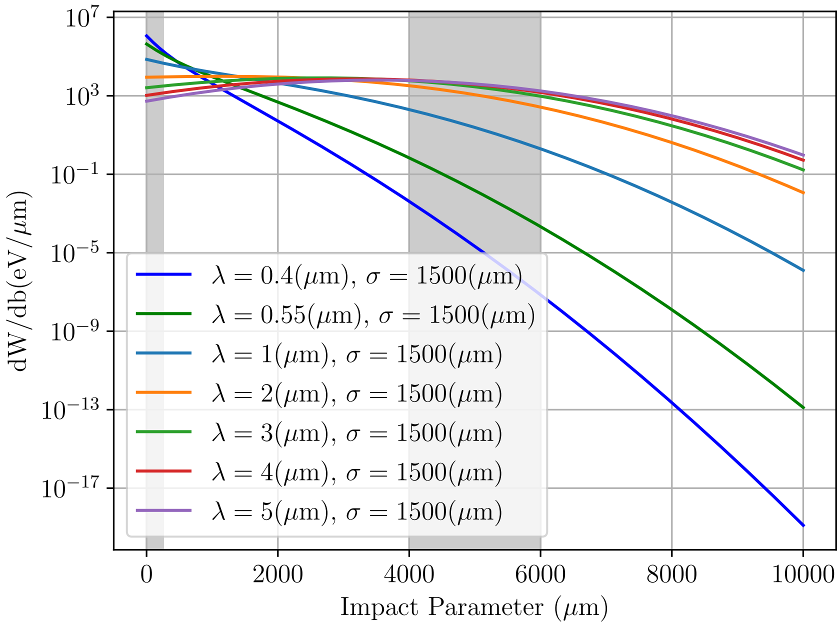

Figure 5.21: ChDR emission of visible and IR wavelengths at each impact parameter generated by the $\sigma = 1500\,\mu m$ beam distribution shown in Fig. 5.16 and the parameters from Table 5.2. The shaded region between 0 and 250 µm highlights the halo of the distribution closest to the radiator, whereas the shaded region between 4000 and 6000 µm highlights the beam core.

contribution of short wavelengths and short impact parameters.

Integrating any plot in Fig. 5.21, 5.22, or 5.23 produces a scalar value for a specific wavelength, and beam size at the impact parameter of 5 mm. Figure 5.24 shows the ChDR beam size dependence for different wavelengths. This is created by repeating the beam integration process for different wavelengths and beam sizes that are all centred at the impact parameter of 5 mm. At small beam sizes the longer wavelengths produce more emission whereas at larger beam sizes the shorter wavelengths do. In order to confirm that the measured signal is from the beam core and not the beam halo the wavelengths experimentally examined will need to be in the region where the emission from longer wavelengths are higher, meaning where the σ_x beam size is $\leq 800\,\mu m$.

5.2.3 Summary of Simulations

An interesting measurement on the BTS would have the beam fixed at a specific impact parameter and measurements taken at different wavelengths. The purpose of this measurement would be to show a beam core dependency that is different to the beam halo dependency. To

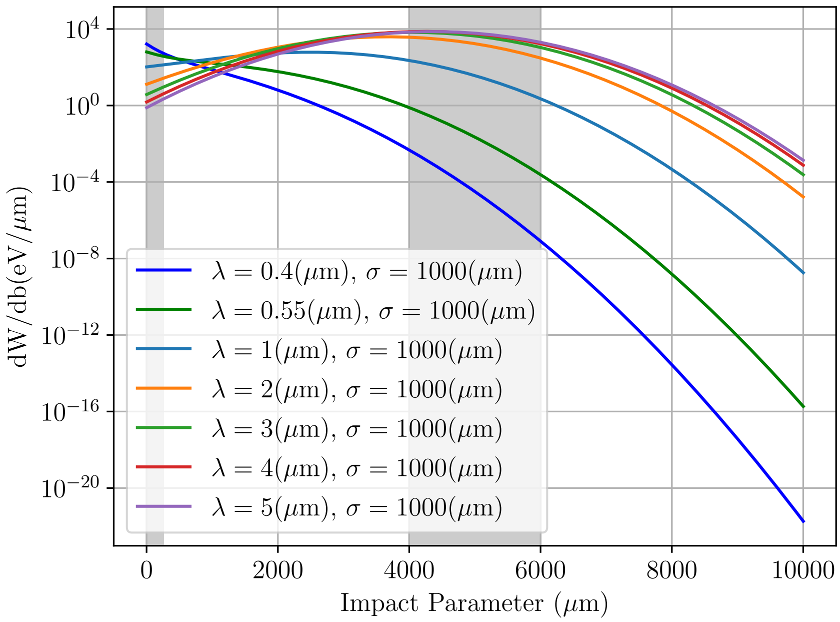

Figure 5.22: ChDR emission of visible and IR wavelengths at each impact parameter generated by the $\sigma = 1000\,\mu\text{m}$ beam distribution shown in Fig. 5.16 and the parameters from Table. 5.2. The shaded region between 0 and 250 µm highlights the halo of the distribution closest to the radiator, whereas the shaded region between 4000 and 6000 µm highlights the beam core.

obtain such a measurement the system needs to be in a regime where the longer wavelengths have a higher emission for a given impact parameter and beam size. For the simulations in Fig. 5.24 this is the when the σ_x horizontal beam size is approximately 800 µm or less. Using the PMT measurement system the longest measurable wavelength is approximately 0.8 µm. Examining this point of the graph the longer wavelengths that are measurable with the PMT should have a higher emission than at shorter wavelengths. If signal cannot be measured at this position the only available action would be to reduce the impact parameter, while this would increase the signal, it disproportionately increases the signal at shorter wavelengths.

The conclusion of these simulations is that while a working regime that favours the ChDR is technically possible it will be quite difficult to measure the different ChDR wavelengths in this regime. If this is not possible then the options are to change the radiator to one that will produce a higher photon yield and rerun these simulations, or to change the detector to one that will measure much longer wavelengths.

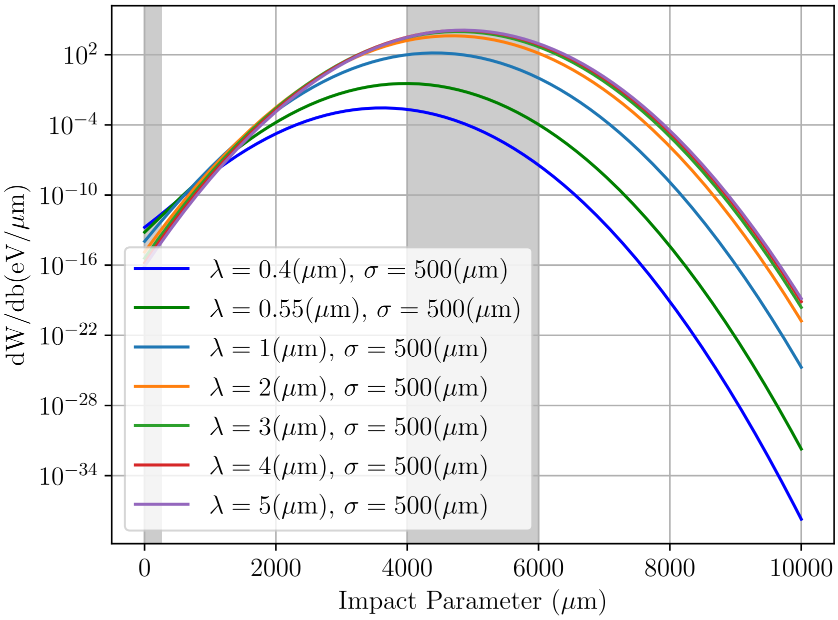

Figure 5.23: ChDR emission of visible and IR wavelengths at each impact parameter generated by the $\sigma = 500\,\mu\text{m}$ beam distribution shown in Fig. 5.16 and the parameters from Table. 5.2. The shaded region between 0 and 250 µm highlights the halo of the distribution closest to the radiator, whereas the shaded region between 4000 and 6000 µm highlights the beam core.

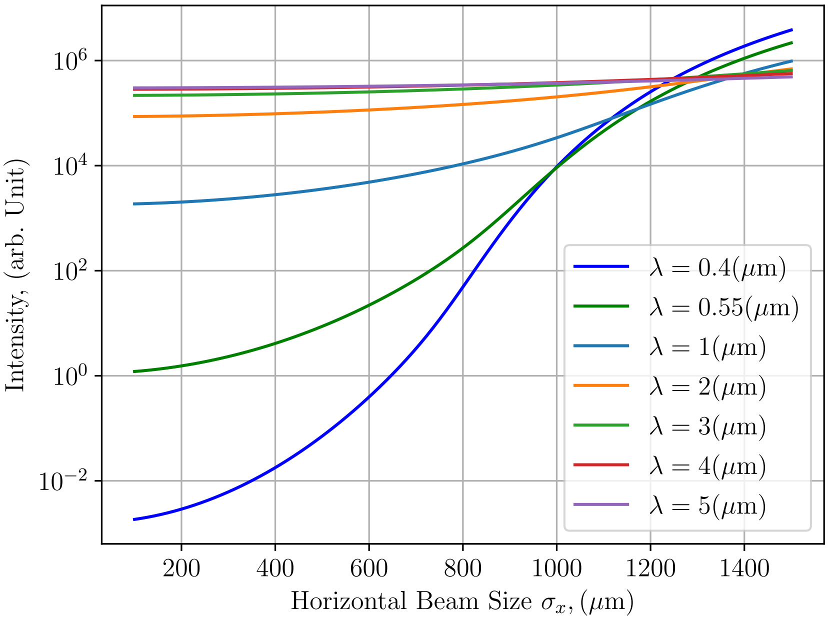

Figure 5.24: Gaussian beam size dependence on ChDR emission of visible and IR wavelengths from a beam centred at an impact parameter of 5 mm and the parameters from Table. 5.2.

CHAPTER 6

IMAGE PROCESSING

Experiments from this thesis have shown that when working at large impact parameters the ChDR photon yield is difficult to measure. To improve the Signal-to-Noise Ratio (SNR) in the images taken a study in image processing has been performed. The images used in this study of processing techniques were taken when the accelerator was set to extract single bunches with charge values of approximately 0.2 nC per bunch. The optical system was set up in the imaging configuration from Table. 4.3 and datasets of 100 images were taken at a number of different horizontal beam positions. The beam bump settings used for this study were, 1000, 1500, 1600, 1700, 1800, 1900, 2000, 2250, and 2500 BU. This corresponds to beam position shift between approximately 2 and 4.5 mm from nominal where the relationship between BU and relative beam position is discussed in Sec. 4.3. For these different datasets the beam position may vary slightly from shot to shot, however for this study the impact parameter was not calculated as the goal of the study is to improve the SNR of the images using processing techniques. The ChDR datasets are used here purely because the data was readily available. Detailed analysis and discussion using these image processing techniques are in Chap. 7.

This chapter considers images as a function, $f(m,n)$, where m and n are the integer column and row coordinates respectively. Each of the coordinates, m and n, are valid from $[1,2,3\ldots M]$ and $[1,2,3\ldots N]$, where M and N are the horizontal and vertical extents of the image in pixels.

To compare between the different image processing techniques discussed in this chapter, projections are taken from the Region Of Interest (ROI) of the images. A projection is a sum of all of the rows or columns in the ROI such that

$$X(m) = \sum_{n=1}^{N} f(m,n), \tag{6.1}$$

$$Y(n) = \sum_{m=1}^{M} f(m,n), \tag{6.2}$$

where $f(m,n)$ is the image function for the ROI, $X(m)$ is the projection across the horizontal axis, and $Y(n)$ is the projection across the vertical.

6.1 Image Stacking

An image stack is represented similar to an image, with the modified function $f(s,m,n)$ where s is the integer index of the stack from $[1,2,3\ldots S]$, where S is the number of images in the stack and m,n have the same notation as a singular image. A mean image can then be produced from the stack using,

$$F(m,n) = \frac{1}{S}\sum_{s=1}^{S} f(s,m,n), \tag{6.3}$$

where $F(m,n)$ represents the image function for the mean value of a specific pixel in the stack.

Figure 6.1 shows four images produced from stacks taken from the Diamond BTS ChDR experiment. The images are produced from the $1800, 1900, 2000$, and 2250 BU stacks, and a ROI has been set around each image to focus onto the ChDR target. These stacks have been chosen as they show the greatest transition in pixel intensity between them.

For the images in Fig. 6.1 the ChDR emission cannot be seen in the 1800 BU image and can clearly be seen in the 2250 BU image. The two images for 1900 BU and 2000 BU the emission can be seen but only faintly. Using an image stack will reduce the effect of random errors but keeps the effects of systematic errors. The vertical lines in Fig. 6.1 can be seen across all of the images, these are defects in the Charge-Coupled Device (CCD) detector used in the ProxiVision camera [71].

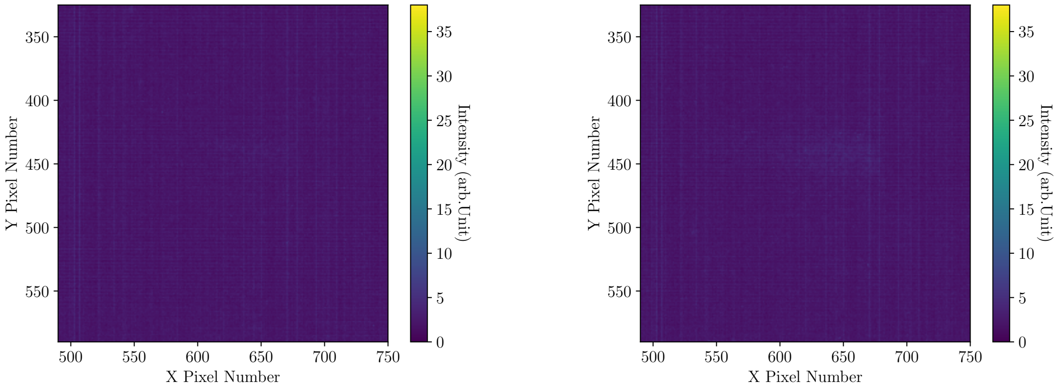

(a) 1800 BU.

(b) 1900 BU.

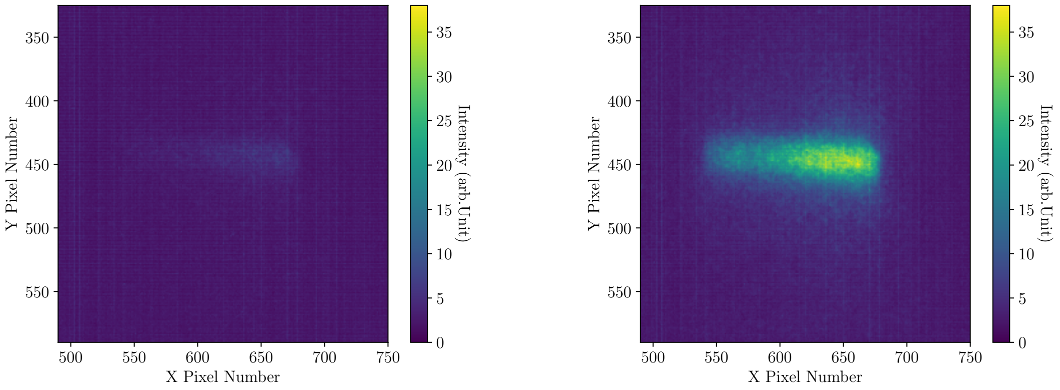

(c) 2000 BU.

(d) 2250 BU.

Figure 6.1: Images showing a ROI around ChDR mean value image stacks produced at different BU settings.

6.2 Background Subtraction

In order to remove systematic errors a background subtraction operation is performed. Figure 6.2 shows the stack of images produced from the 1000 BU dataset and Eq. 6.3, as no signal is visible in this dataset it is used as a background image. The background is subtracted using

$$H(m,n) = \begin{cases} f(m,n) - B(m,n) & \text{if } f(m,n) > B(m,n), \\ 0 & \text{otherwise}, \end{cases} \tag{6.4}$$

where $H(m,n)$ represents the final image, $B(m,n)$ is the mean background image created from the 1000 BU stack, and $f(m,n)$ is the source image. It is possible for a pixel value to be higher in the background image so to avoid negative values in the final image negative values are replaced with zeros.

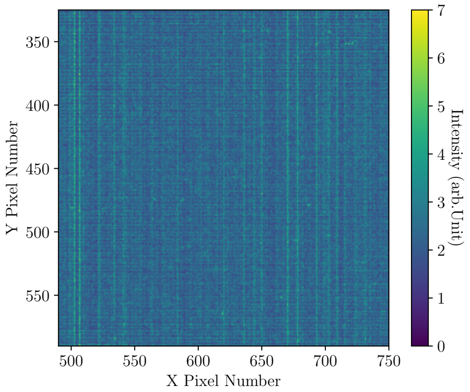

Figure 6.2: Background ROI mean image stack produced using the dataset taken at 1000 BU.

To clearly show the defects of the CCD detector, mean projections have been taken from the horizontal and vertical axis on Fig. 6.2. These projections are shown as a bar graph in Fig. 6.3; the vertical has sporadic peaks showing the defects from the CCD camera, whereas the horizontal is relatively flat in comparison. A bar graph is used so that the individual rows or columns of pixels can be clearly seen.

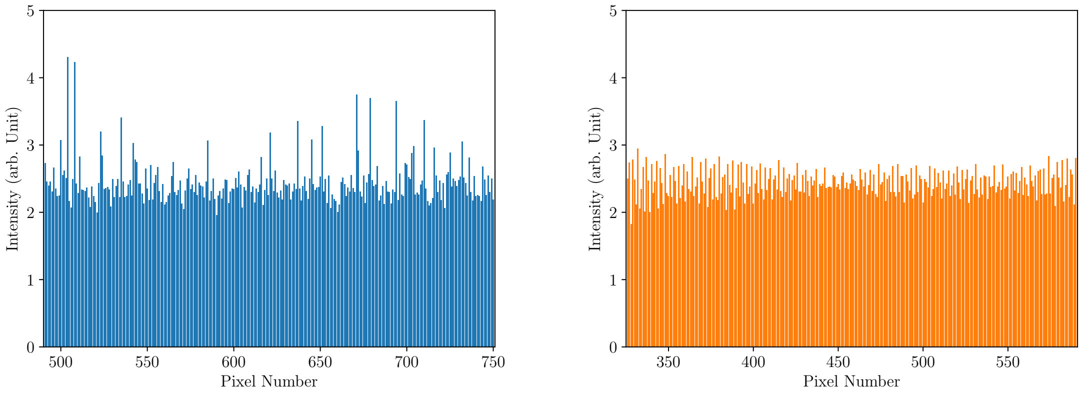

(a) Horizontal.

(b) Vertical.

Figure 6.3: Mean projections for the background image stack in Fig. 6.2.

Figure 6.4 shows the result of a background subtraction process where the images from Fig. 6.1 are the source images and Fig. 6.2 is the background image. The vertical lines from the CCD noise in Fig. 6.1 have been removed using the background subtraction process. To clearly show this Fig. 6.5 has been produced. This shows the projections of the 2000 BU datasets from Fig. 6.1 and 6.4. The subscript μ represents the datasets from Fig. 6.1 whereas the BG subscript is for the datasets from Fig. 6.4. When examining these results the horizontal projection is noticeably cleaner due to the CCD spikes being removed by the background subtraction process.

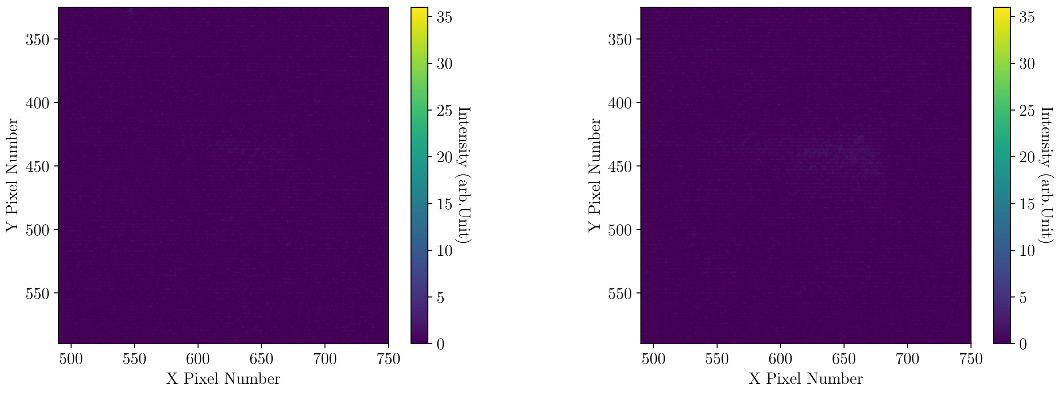

(a) 1800 BU.

(b) 1900 BU.

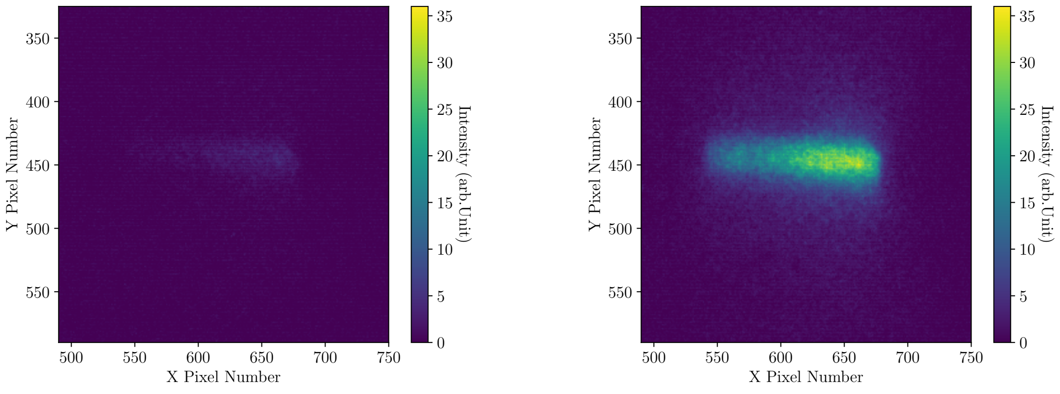

(c) 2000 BU.

(d) 2250 BU.

Figure 6.4: Images from Fig. 6.1 with Fig. 6.2 subtracted as a background using Eq. 6.4.

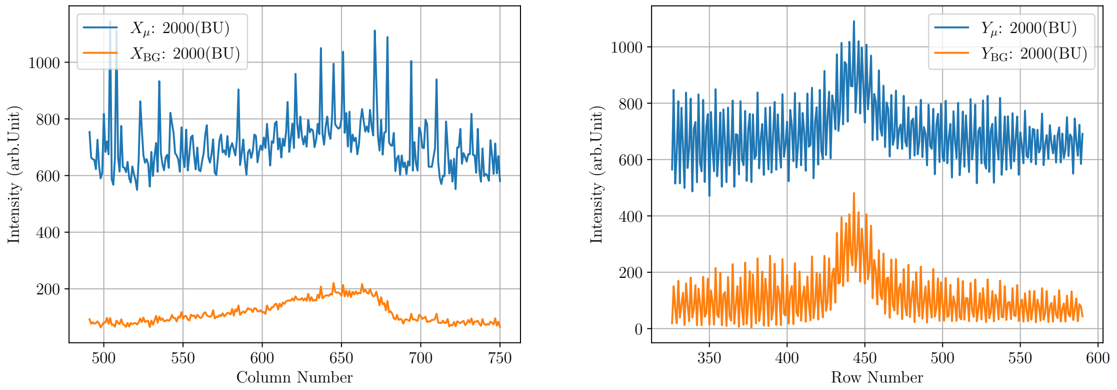

(a) Horizontal.

(b) Vertical.

Figure 6.5: Horizontal and vertical projections from the 2000 BU datasets from Fig. 6.1 and 6.2, labelled with the subscripts μ and BG respectively.

6.3 Sigma-Clipping Image Stacks

Figure 6.4 uses background subtraction to remove systematic errors from a source image. A potential issue with background subtraction is that the signal produced in the background image will be a mixture of systematic errors and random errors. By taking a larger stack of background images the random errors in the background image can be reduced but not entirely removed as they are still present in the mean calculation (see Eq. 6.3).

To remove outlier data a sigma-clipping operation is performed on an image stack. A sigma-clipping operation removes all values from a sequence that are more than a specified standard deviation from the mean, described by

$$\hat{X}(n) = \begin{cases} X(n) & \text{if } (\mu_X - c\sigma_X) < X(n) < (\mu_X + c\sigma_X), \\ \text{Removed} & \text{otherwise}, \end{cases} \tag{6.5}$$

where X is the input sequence, n is integer index of the sequence, μ_X is the mean value the sequence, σ_X is the standard deviation of the sequence, c is a user specified multiple, and $\hat{X}$ is the clipped sequence [72]. A further sigma-clipping operation can then be performed on the new dataset, or a mean can be taken to obtain a single value for the clipped sequence.

Outlier errors are removed from the background image by setting each pixel coordinate as as a sequence for the background image stack then performing a sigma-clipping operation for each pixel coordinate. Figure 6.6a shows the image from Fig. 6.2 and Fig. 6.6b the same image after a single sigma-clipping operation of 2.5σ has been performed. The value of 2.5σ is selected as it will keep the bulk of the signal but remove outliers from the dataset. Figure 6.6 shows that vertical lines from the detector are still present in the filtered background image but other parts of the signal are lower in amplitude.

Figure 6.7 shows the images from Fig. 6.1 with the sigma-clipped background image from Fig. 6.6 subtracted from them using Eq. 6.4. As with the previous background subtraction images from Fig. 6.4, the vertical lines created from the systematic errors have been removed, however now as the amplitude of the subtraction is lower, the emission ROI now has a higher intensity value.

To clearly show the sigma clipping results Fig. 6.8 has been produced. This shows the projections of the 2000 BU datasets from Fig. 6.1 and 6.7. For the subscripts in Fig. 6.8 μ represents the datasets from Fig. 6.1 whereas σ represents the datasets from Fig. 6.7. Like the original background subtraction the vertical lines from the CCD are removed though

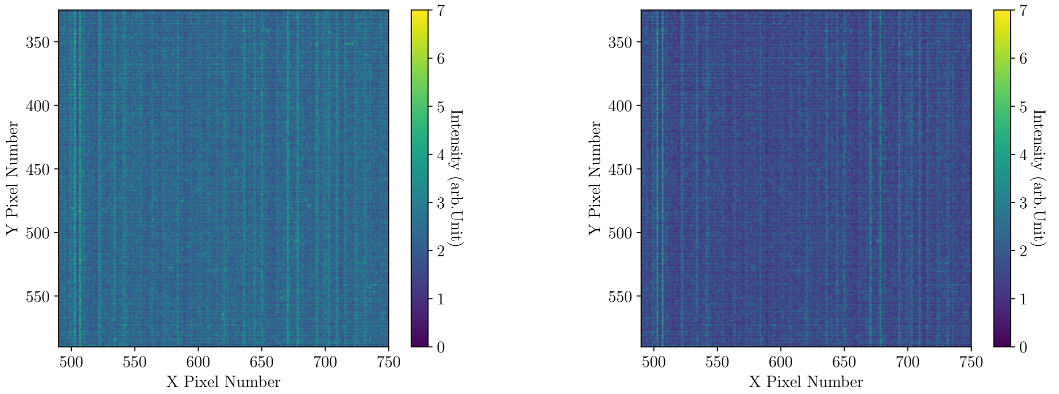

(a) 1000 BU mean image stack.

(b) 1000 BU single iteration 2.5σ sigma-clipped mean image stack.

Figure 6.6: Comparisons between a mean image stack and a sigma-clipped mean image stack to be used for background subtraction.

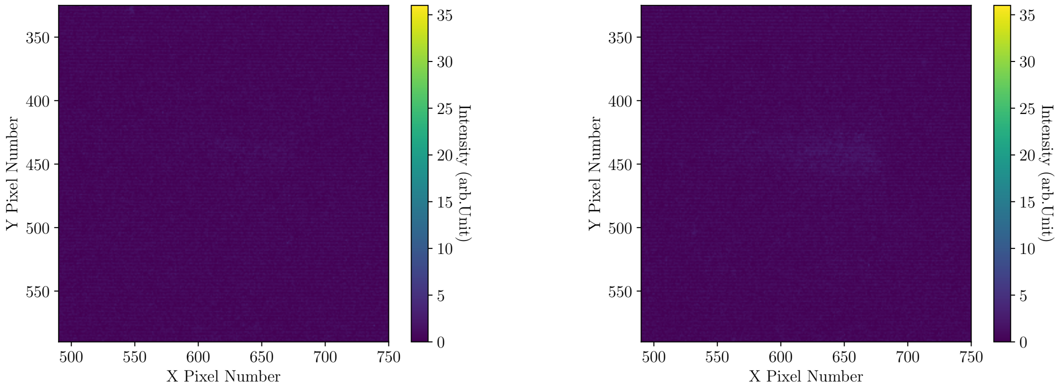

(a) 1800 BU.

(b) 1900 BU.

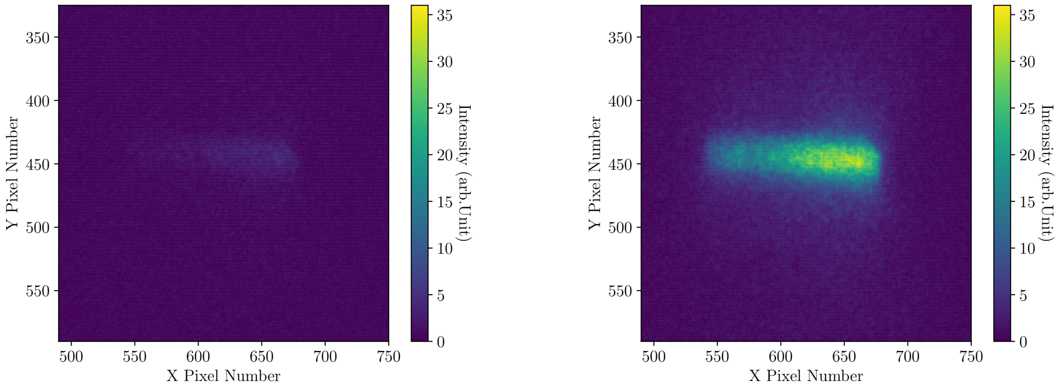

(c) 2000 BU.

(d) 2250 BU.

Figure 6.7: Images from Fig. 6.1 with image (b) from Fig. 6.6 subtracted as a background using Eq. 6.4.

now the overall signal intensity is higher.

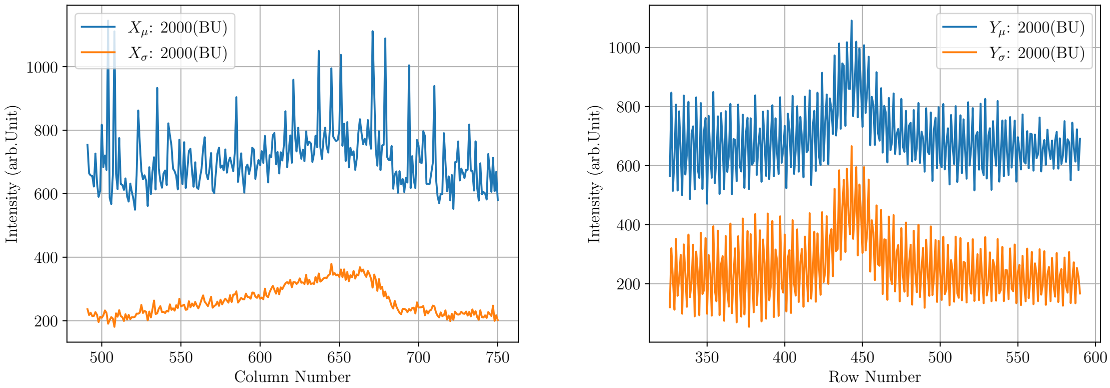

(a) Horizontal. **(b)** Vertical.

Figure 6.8: Horizontal and vertical projections from the 2000 BU datasets from Fig. 6.1 and 6.7, labelled with the subscripts μ and σ respectively.

6.4 Frequency Domain Filtering

A slight graininess can be observed in the ChDR signal of the images discussed in this chapter. Graininess is a result of digital noise from the camera system [71]. When taking projections and ROI sums the graininess affects the results produced. In order to remove the graininess the higher frequency components of an image are removed. An image function $f(m, n)$ can be converted from the spatial domain to the frequency using Fast Fourier Transform (FFT) such that

$$F(r, c) = \mathcal{F}\{f(m, n)\}, \tag{6.6}$$

where $F(r, c)$ is the frequency domain image with real and complex indexes. The higher frequency components can then be removed from the image such that $F(r, c) = \hat{F}(r, c)$, where $\hat{F}$ is the image with the removed frequency components.

When processing an image in the frequency domain there are many operations that can be performed, not just removal of higher order frequencies [73]. Once frequency domain processing is complete the image is converted back to the spatial domain using an inverse Fourier transform such that

$$\hat{f}(m, n) = \mathcal{F}^{-1}\{\hat{F}(r, c)\}, \tag{6.7}$$

where $\hat{f}(m, n)$ is the filtered image.

Figure 6.9 uses the sigma-clipped images from Fig. 6.7 as source images, then removes the highest 90% of frequency components present in the images by converting to and from the frequency domain using Eq. 6.6 and 6.7. Removing different frequency component values were tested but removing the highest 90% greatly reduces the noise on the projections of the images while still allowing for the overall image and projection to be seen.

By visually comparing the images from Fig. 6.7 and 6.9, it can be seen that the latter appears blurry. While this may result in an image that is harder to interpret visually, taking projections or sums of the filtered ROI will provide data that has been smoothed allowing for easier comparisons between the datasets. Such projections are displayed in Fig. 6.10. The μ subscript represents projections from the 2000 BU dataset from Fig. 6.1 whereas the FT subscript represents the equivalent dataset from Fig. 6.9. By removing the higher frequency components as well as removing the CCD spikes the vertical and horizontal projections are significantly smoothed.

6.5 Comparisons

A comparison is made by calculating vertical and horizontal projections for the 2000 BU ROI images. Each processing method has its own subscript where: μ denotes the mean image stacks from Fig. 6.1; BG the background subtracted mean image stacks from Fig. 6.4; σ the mean image stack with the sigma-clipped background subtraction from Fig. 6.7; and FT for the Fourier transformed images with the higher frequency components removed from Fig. 6.9. The horizontal and vertical projections are then displayed in Fig. 6.11 and Fig. 6.12 respectively.

The projection X_μ in Fig. 6.11 shows spikes in the data that line up with vertical lines caused by systematic errors of the CCD detector. All of the results in Fig. 6.11 that feature a background subtraction operation have the vertical CCD spikes removed. The two projections X_{BG} and X_σ have a very similar distribution. It appears that the sigma-clipping operation has uniformly scaled the entire image, though if the random errors present in the background image stack are of a uniform nature this is the expected result. The plot X_{FT} shows the projection that had 90% of the higher order frequency components removed, this

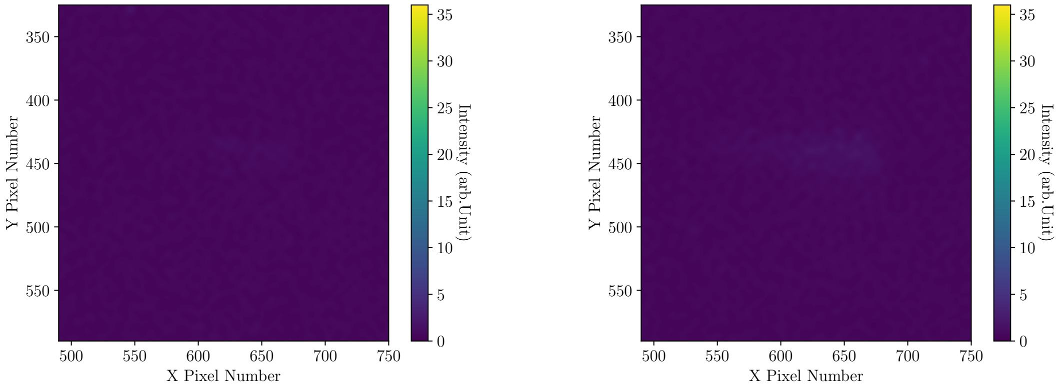

(a) 1800 BU.

(b) 1900 BU.

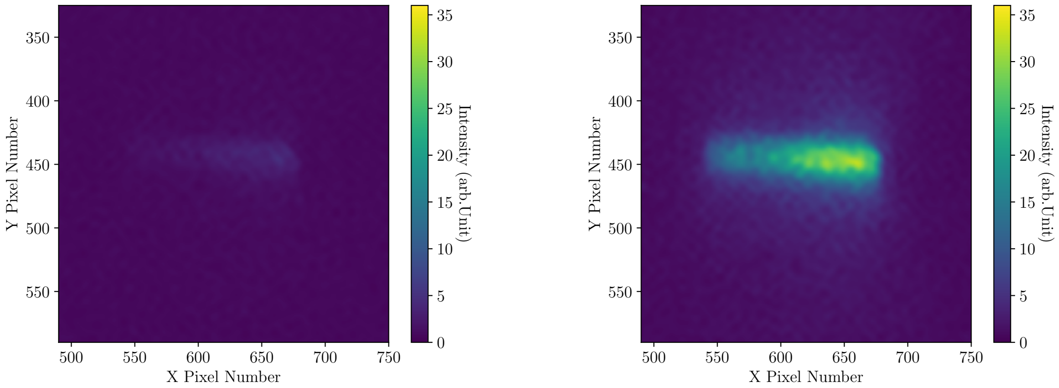

(c) 2000 BU.

(d) 2250 BU.

Figure 6.9: Images from Fig. 6.7 with the highest 90% of frequency components removed.

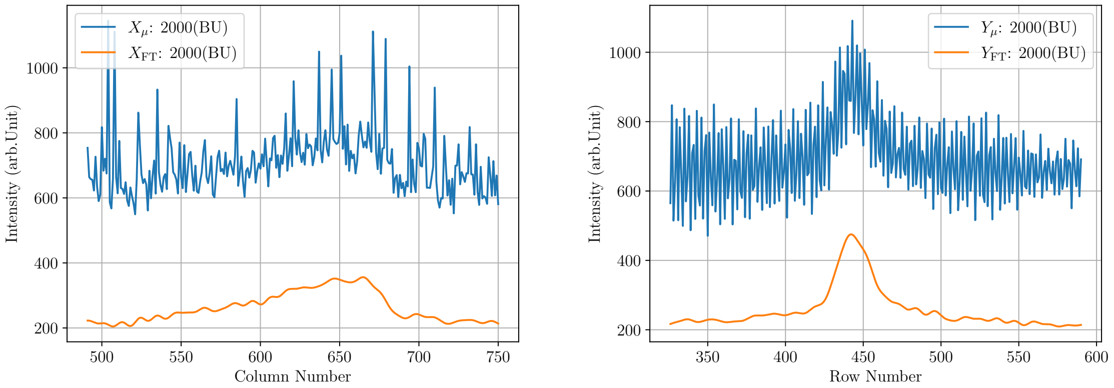

(a) Horizontal.

(b) Vertical.

Figure 6.10: Horizontal and vertical projections from the 2000 BU datasets from Fig. 6.1 and 6.9, labelled with the subscripts μ and FT respectively.

plot is far smoother than the projection of the image that produced it X_σ.

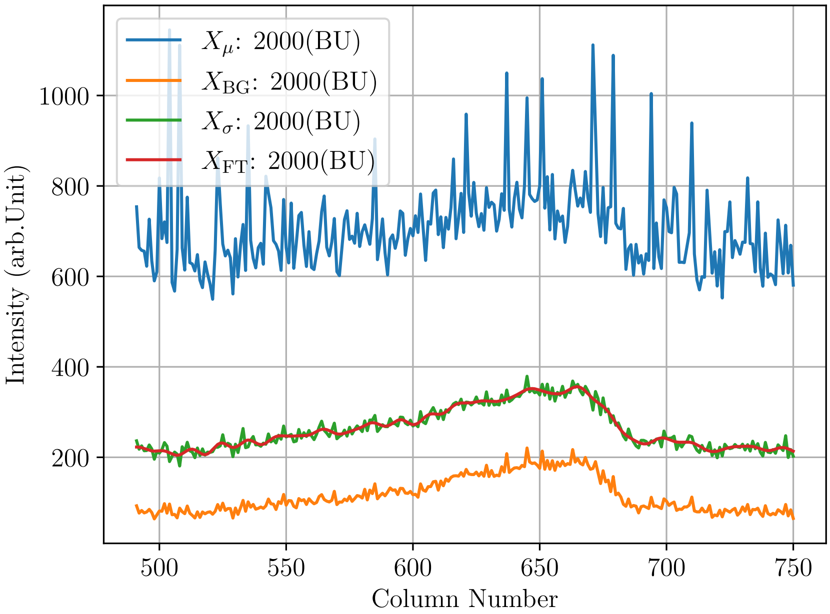

Figure 6.11: Horizontal projections taken from the 2000 BU images seen in Fig. 6.1, 6.4, 6.7, and 6.9 using Eq. 6.1.

Observing the projections in Fig. 6.12 there appears little difference in the projections Y_μ, Y_{BG} and Y_σ apart from a linear scaling. High frequency noise can be seen in Fig. 6.12 caused by the graininess of the images. The projection of the plot Y_{FT} is significantly smoother than the others due to the removal of the higher frequency components.

Combining the observations from Fig. 6.11 and 6.12 it has been decided that the best processing techniques are obtained when combining a sigma-clipped background subtraction and removing the higher order frequency components. This process removes intensity outliers and the high spatial frequencies from the image. A similar result would be obtained without sigma-clipping the background image, though this allows for an extra degree of control by selecting the user specified multiple parameter (see Eq. 6.5).

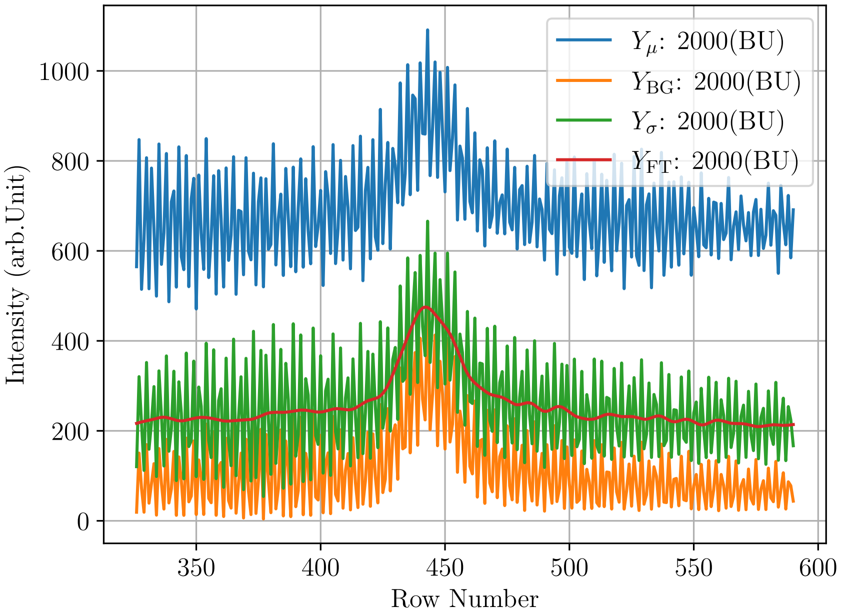

Figure 6.12: Vertical projections taken from the 2000 BU images seen in Fig. 6.1, 6.4, 6.7, and 6.9 using Eq. 6.2.

CHAPTER 7

EXPERIMENTAL RESULTS

7.1 Imaging

The results in this section are the imaging measurements taken from the Diamond BTS ChDR experiment using the optical system described in Sec. 3.2.2. In order to take an impact parameter scan the horizontal transverse beam position is changed using beam adjustment codes (see Sec. 4.3), and then the process described in Sec. 4.4 is used with OTR1 and OTR2 to obtain the impact parameter. The different scans detailed here either measure the unfiltered ChDR emission, or the filtered ChDR emission with either a 400 or 550 nm bandpass filter. The direct images taken from this optical system show the location and extents of the ChDR radiator. Figure 7.1 shows an example image taken of the ChDR emission when no filters are present in the optical system. The radiation emission is imaged using the optical system, and can be seen near the centre of the image.

Examining Fig. 7.1 there is only one area of signal in the image, meaning no background signal sources such as scattered SR are clearly evident. The ChDR emission seen only fills a small fraction of the image where the emission is not uniform, this is due to the optical path of the ChDR through the radiator. Examining the ChDR emission a ROI is set in three locations and applied to the image: the Chamfer, Reflector, and Bulk. The Chamfer shows direct ChDR from the tip of the radiator with a minor fraction of the accumulated radiation. The Reflector emits the majority of ChDR that has been accumulated along the entire radiator. Finally the Bulk emits radiation that leaks throughout. The difference between the Chamfer and Radiator is due to the optical path that the ChDR takes through the radiator. Given these descriptions the ChDR emission from the Radiator is expected to

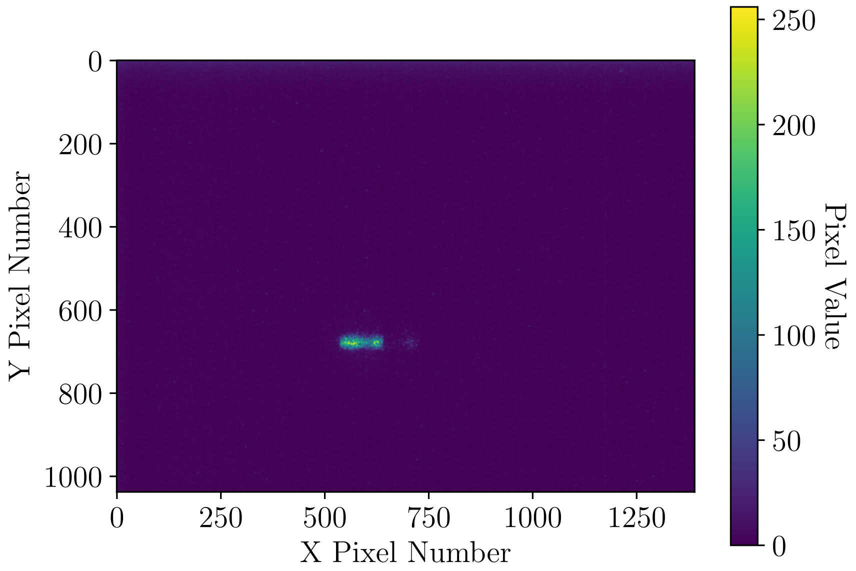

Figure 7.1: Unfiltered ChDR Image taken from setup described in Sec. 3.2.2.

be the highest. The expectation for the Chamfer is that is will be lower but still comparable to the Radiator, whereas the Bulk is expected to produce very little signal.

Figure 7.2 shows the ChDR emission image from Fig. 7.1 with the three different ROIs applied and annotated to the image. The relative intensity and size of each ROI in Fig. 7.2 suggests to support the descriptions of each ROI. In order to fully understand these relationships more in-depth intensity analysis has been performed.

7.1.1 Imaging Results

The imaging measurements were taken by fixing the beam settings and taking ten images from the ChDR system while simultaneously taking images with OTR1 and OTR2. When taking an image if too many of the pixels are saturated then the signal is clipped and information is lost. For this reason any ChDR images that had saturated pixels in more than 1% of a ROI were discarded from this analysis.

Figure 7.3 shows the mean intensity per pixel in each ROI for a range of impact parameters, each point is produced by summing the ROI of the non-discarded images taken with the same beam settings. A source of error between the different ROIs is potentially caused when selecting the extents of each ROI. The mean value is reported for each ROI so any pixels

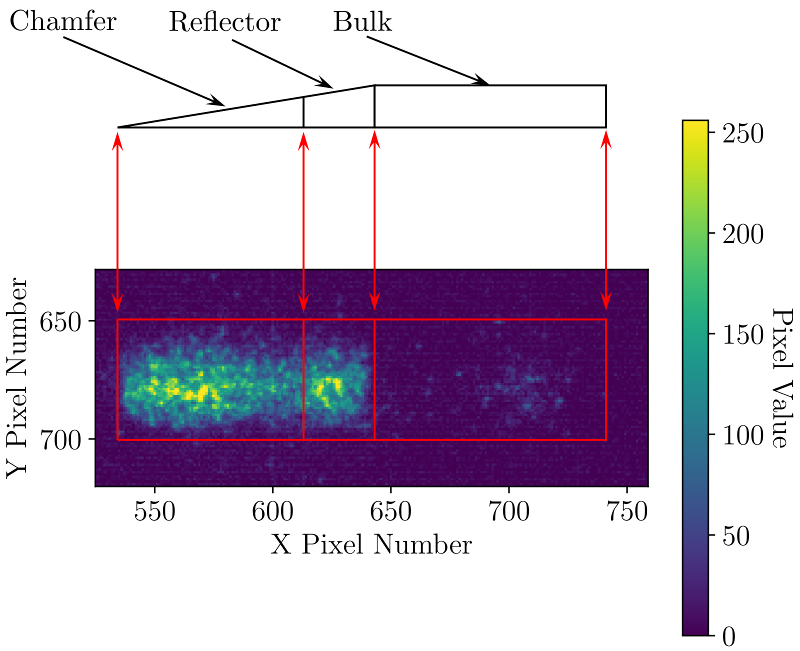

Figure 7.2: Imaged ChDR emission from Fig. 7.1 with the different regions of interest highlighted.

that cover the background and not the radiator will disproportionately effect the results from each ROI. For each point a value of 42.5 arb. Unit has been removed in order to perform the background subtraction. This value was calculated by examining the dead space in several images and taking a mean. The bunch charge was not recorded on a shot-by-shot basis for these experiments as the IBPM had not been commissioned when they took place. For these results the bunch charge was set between 0.1 and 0.2 nC, this was monitored using an upstream ICT but the data was not recorded.

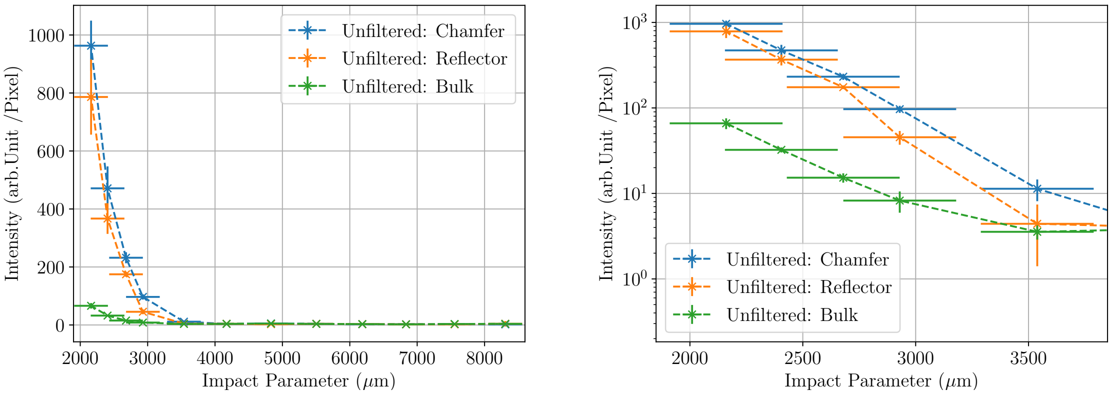

(a) Linear axis.

(b) Cropped logarithmic axis.

Figure 7.3: Unfiltered impact parameter scan from imaging datasets.

Figure 7.3a shows the full unfiltered dataset on a linear axis, whereas Fig. 7.3b has been cropped around the part of the data that shows that growth of the intensity plot on a logarithmic axis. Examining Fig. 7.3b the gradient of all three datasets appears to be similar, this shows that the relative growth of each area is similar. Figure 7.3 shows the Chamfer as having the highest mean intensity for the closest impact parameters. This implies there is radiation leaking throughout the radiator. Given that some signal is measured in the bulk, this also implies there is signal leaking throughout the radiator. For both of the Chamfer and the Reflector, emission is not measured from either of these until the impact parameter reaches a value of $\leq 3000\,\mu\text{m}$. As the horizontal transverse beam size σ_x in these experiments is approximately 1500 µm some of the outer edges of the distribution will be scraping on the radiator potentially producing direct CR.

Figures 7.4 and 7.5 respectively show impact parameter scan results when the 400 and 550 nm bandpass filters are used. The intensity in Fig. 7.5 has been scaled by a factor of 0.87 as this accounts for the differences in QE and the transmission of the bandpass filters at the central passband wavelength. Examining Fig. 7.4b and 7.5b the relative growth of each ROI can be examined. The intensity in all three ROIs in Fig. 7.4b increase at similar rates, whereas the Bulk plot in Fig. 7.5b is noticeably shallower. This may be from the TIR angle that changes at different wavelengths.

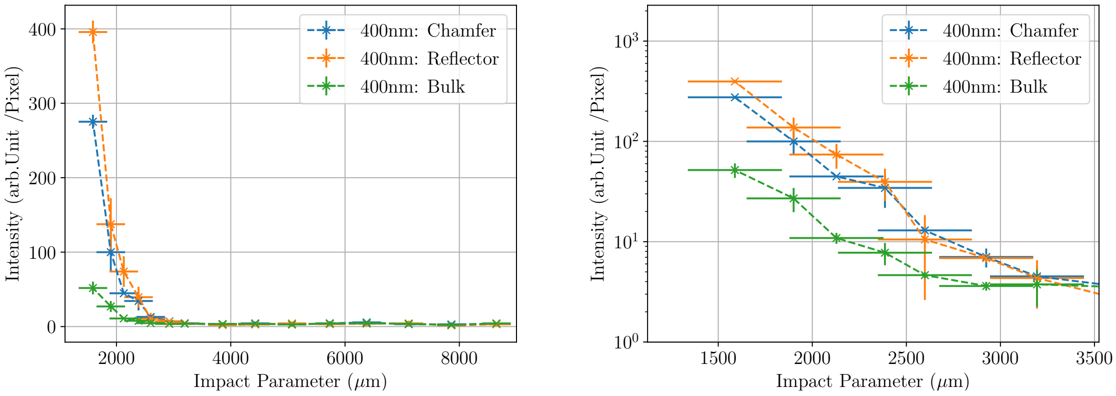

(a) Linear axis.

(b) Cropped logarithmic axis.

Figure 7.4: Processed and scaled impact parameter scan taken using the 400 nm bandpass filter.

7.1.2 Imaging Interpretation

In order to compare the results taken with the bandpass filters an exponential function is fit to the datasets, the fit takes the form

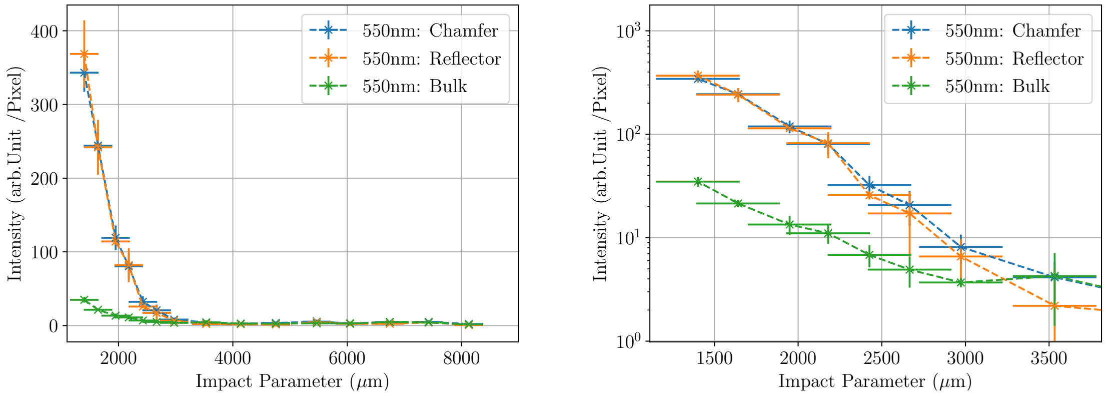

(a) Linear axis. **(b)** Cropped logarithmic axis.

Figure 7.5: Processed and scaled impact parameter scan taken using the 550 nm bandpass filter.

$$I = Ae^{Bb}, \tag{7.1}$$

where I is the intensity, b is the impact parameter, and A, B are the fit parameters. Figure 7.6 shows the exponential fits for the ChDR bandpass filters, displayed on both a linear and logarithmic axis. At low impact parameters 400 nm is the dominant wavelength in all ROIs. At the larger impact parameters the dominant wavelength is 550 nm where there is a transition between the two at approximately 2 mm for the Chamfer and Radiator, and 2.5 mm for the Bulk.

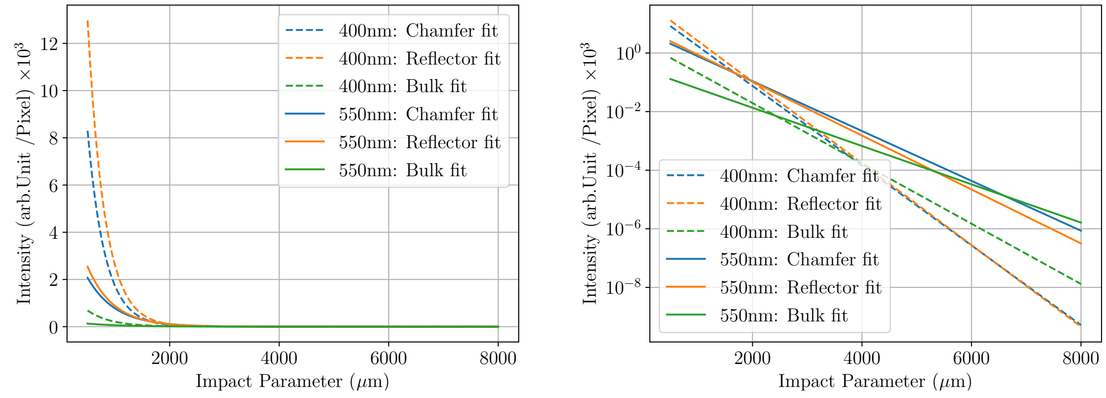

(a) Linear axis. **(b)** Logarithmic axis.

Figure 7.6: Exponential fit of impact parameter scans displayed in Fig. 7.4 and 7.5.

The longer wavelength dominates at the larger impact parameter of the fits shown in Fig. 7.6. Unfortunately the signal is so low at these impact parameters that a reliable beam position measurement cannot be made using this detector.

The σ_x beam size for the unpolarised data taken in Fig. 7.3 was approximately 1.4 mm. At the impact parameters where signal could be measured, the beam was close enough to induce CR and DR. Given these signals are heavily coupled together it is difficult to prove if CR and DR are generated, and at what signal proportions.

A reminder that the effective electron radius from Eq. 2.8 shows

$$r_E = \frac{\gamma\lambda}{2\pi}. \tag{7.2}$$

It is thought that the vertical height of the radiator will need to be several times larger than the effective electron radius in order to replicate the decay behaviour seen in Chap. 5. The height of the radiator used in these experiments is 2 mm where the effective electron field radius is between 0.4 and 0.6 mm for optical wavelengths and even larger for longer wavelengths. While the radiator height is larger the PCA simulations assume an infinite radiator height, having a limitation here introduces an additional decay factor. Additionally this decay factor could be increased due to the multiple reflections the ChDR undergoes inside an accumulation radiator.

In conclusion the imaging results have shown that photon yield can be measured from the ChDR radiator though the photon yields with the current setup are only visible at very low impact parameters and thus the signal is likely from the beam halo and not the beam core. In order to increase the beam core sensitivity more experiments are performed with smaller beam sizes and at longer wavelengths.

7.2 Angular Distributions

The optical system from Fig. 3.17 was used to make angular distribution measurements on the Diamond BTS. For the experimental results listed in this section, the Diamond accelerator was set to extract a single bunch at a rate of 1 Hz. The bunch charge was set between 0.15 and 0.2 nC. Apart from this, the default parameters from Table. 3.1 have been used. To measure at the largest impact parameters the gain of the camera and intensifier have been set at their maximum values for all of the experiments in this section.

The angular distributions have been measured unfiltered or using the 400 and 550 nm band-pass filters. Polarised angular distribution measurements have also been taken using a LPVISA100-MP2 polariser in both the horizontal and vertical position [59]. All of the image stacks shown in this section have been transposed so that the polar and azimuthal axes match the simulations from Chap. 5.

The angular distribution data is composite, it is built from signal acquired from the three different target areas (Chamfer, Reflector and Bulk) and background signal from background sources such as SR. Due the different signal sources and the different target used in the PCA simulations the angular distributions cannot be compared directly. As described in Sec. 3.2.3 the optical system was carefully designed to maximise the angular acceptance. When examining the angular distributions in this chapter it appears that the ChDR distributions are clipping on the angular acceptance of the optical system.

7.2.1 Unfiltered Angular Results

The unfiltered angular distributions do not use any filters or polarisers. In this mode the camera will be sensitive to both polarisations and the broadband spectrum according to the quantum efficiency of the camera (see Fig. 3.14 and 3.15).

Figure 7.7 shows an image stack of angular distributions and the background that has been subtracted from the source image stack. The background in Fig. 7.7b was produced by creating an image stack of angular distributions measured at the impact parameter of approximately $6890 \pm 570\,\mu\text{m}$ and performing a single sigma clipping operation where $c = 2.5$ (see Eq. 6.5). The subtracted background features some beam induced signal that can be seen in the bottom right hand corner. By adjusting the motor stages and beam height it has been shown that this is not produced by the ChDR radiator. This signal is believed to be a reflection of SR that is generated in the upstream dipole magnet and propagates with the beam. As the beam position is changed by altering dipole corrector magnets, the SR background should be a function of the beam position. The background subtraction performed on each dataset is done by using a dataset at a large impact parameter. Large impact parameter datasets are chosen as there should be minimal desired ChDR signal present while attempting to measure the background. For completeness the subtracted background is also displayed with each image set.

The angular distributions in Fig. 7.7a have been taken at a mean impact parameter of approximately $2310 \pm 360\,\mu\text{m}$. As the size of the distribution is larger than the PCA simulations predict projections are taken from a number of angular distributions. The projections shown in Fig. 7.8 are taken from unfiltered angular distributions stacks that have the background from Fig. 7.7 removed as well as the top 90% of higher order frequency components (see Sec. 6.4). PCA simulations show that the angular distribution is expected to increase in size

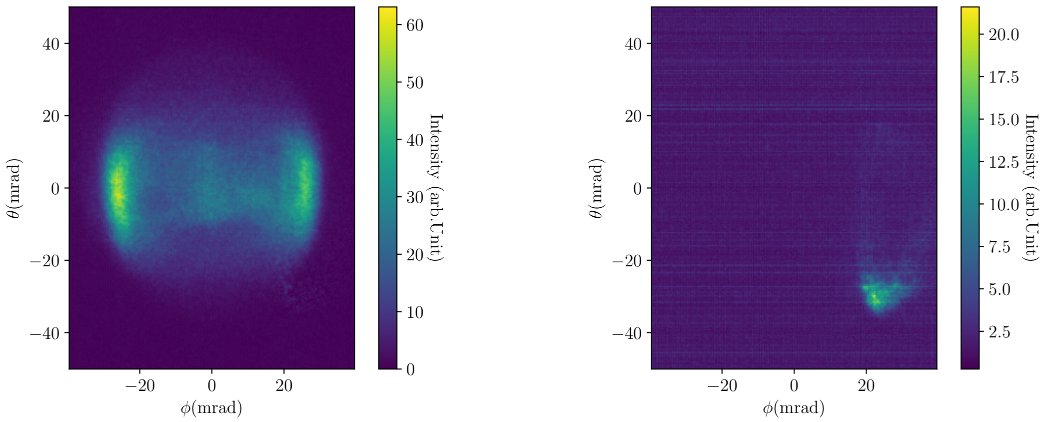

(a) Angular distribution.

(b) Subtracted background.

Figure 7.7: Unfiltered angular distribution image stack, measured at a mean impact parameter of approximately 2310 ± 360 µm. Subtracted Background image stack measured at an impact parameter of approximately 6890 ± 570 µm.

as the impact parameter reduces, while the intensity increases.

The simulations produced in Chap. 5 calculate the vertical and horizontal polarisation independently to produce projections like those seen in Fig. 5.10 and 5.11. Unless a polariser is used to filter out a specific polarisation both of these will be measured together. The projections seen in Fig. 7.7 are broadly the shape you would expect to see from the from the simulations. In the simulations both the horizontal and vertical polarisations are centred around the same polar angle so a single peak for the polar projection in Fig. 7.7a matches this. The projections onto the azimuthal axis in Fig. 7.7b feature three peaks, here the simulations predict that there should only be two but it should be a combination of a central peak is from the vertical polarisation component, and the two side lobes from the horizontal. As the side lobes are much higher than the central one this is broadly the shape that is predicted.

The shape of the distribution (where it can be measured) is largely independent of impact parameter. One potential implication of this is that the signal measured is dominated by halo particles (see Chap. 5). Another theory is that the target height is too small resulting in a large diffraction effect broadening the distribution. Given that there are multiple reflections inside the radiator it may also be that the distribution broadens with each reflection before it is extracted. Another theory is that the angular distribution is too large for the angular acceptance of the optical system given the relatively low impact parameter when signal is measured.

Impact parameter scans are produced by using OTR2 and the IBPM in conjunction with the

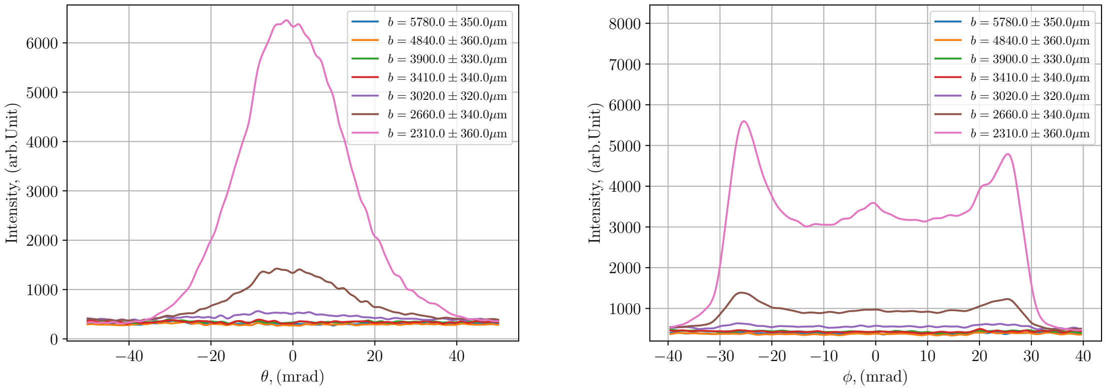

(a) Projection of ϕ onto the θ axis.

(b) Projection of θ onto the ϕ axis.

Figure 7.8: Projections of the unfiltered angular distributions.

angular distribution images. Together OTR2 and the IBPM report the impact parameter, where the IBPM is also used to measure the bunch charge. Taking a sum of the pixels contained in an angular distribution yields an intensity that is then linearly normalised to a bunch charge of 0.2 nC. Figure 7.9 shows the impact parameter dependence. There is no signal measured until the impact parameter is below approximately 3 mm, given the horizontal beam size from these points is $\sigma_x = 1310 \pm 120\,\mu\text{m}$ a significant portion of the signal measured will likely be from particles being very close to the radiator.

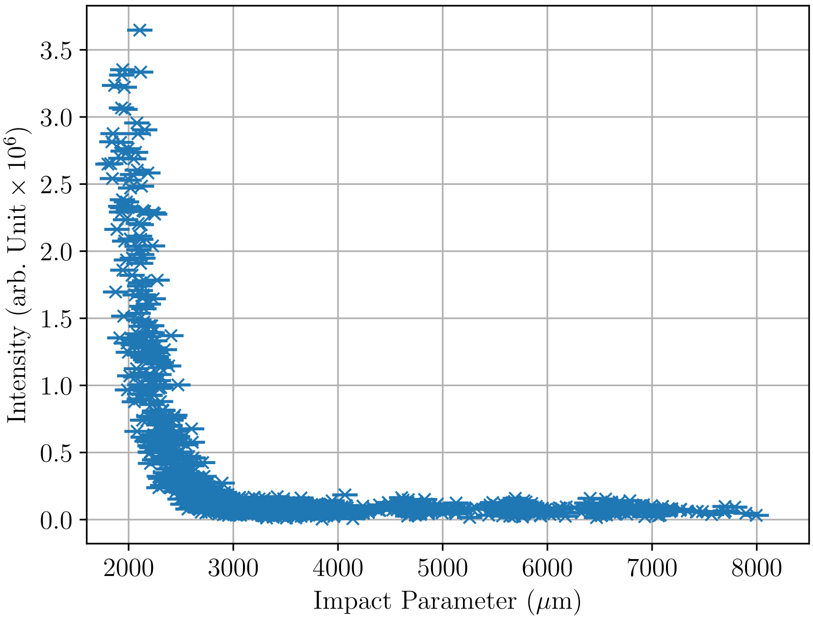

Figure 7.9: Unfiltered impact parameter response, with a mean beam size of $\sigma_x = 1310 \pm 120\,\mu\text{m}$, and normalised to a bunch charge of 0.2 nC.

7.2.2 Polarised Angular Results

The angular distributions and projections simulated in Chap. 5 predict that there should be a difference between the two different polarisations of ChDR. The simulations show that the polarisation that is θ aligned is predicted to display a higher function that has a zero in the centre, whereas the polarisation φ aligned is predicted to display a function that has a peak in the centre. Figure 7.10 shows an angular distribution stack measured for the vertical polarisation.

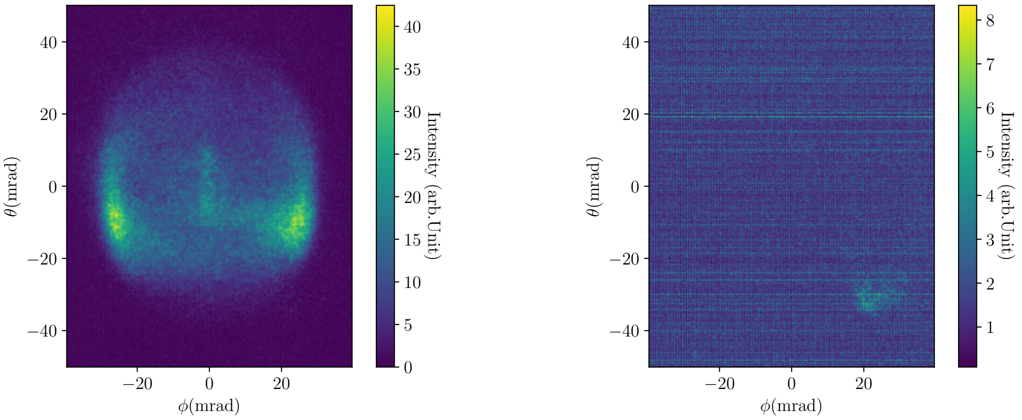

(a) Angular distribution. **(b)** Subtracted background.

Figure 7.10: Vertical (azimuthally, ϕ, aligned) polarisation angular distribution image stack, measured at a mean impact parameter of approximately $1830 \pm 120\,\mu$m. Subtracted background image stack measured at an impact parameter of approximately $4240 \pm 360\,\mu$m.

Projections taken from the vertical polarisation datasets are shown in Fig. 7.11. The experimental projection onto the polar axis reveals a function with a single peak that appears to be offset to the side. The optical system alignment was not changed from a dataset that was central for unpolarised unfiltered data. The projection onto the azimuthal axis shows a similar function to the unpolarised projection (see Fig. 7.8), but the ratio of side lobes to the centre of the distribution has shifted in favour of the centre.

Figure 7.12 shows an angular distribution stack created from a horizontally polarised dataset. The polariser was installed and aligned with the polar axis. Examining the projections in Fig. 7.13 the projection onto the polar axis has a Gaussian like shape, whereas the azimuthal projection has a more complex three lobed shape. Comparing the ratio between the centre of the distribution and the side lobes for the different azimuthal projections the centre is favoured in the vertical polarisation, and the side lobes favoured in the horizontal.

Comparing the projections in Fig. 7.11b and 7.13b with the simulations in Fig. 5.10 and 5.11

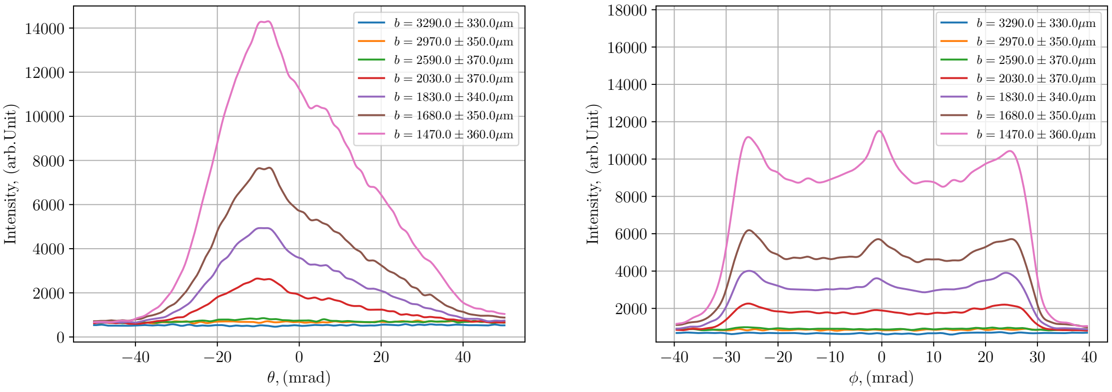

(a) Projection of ϕ onto the θ axis **(b)** Projection of θ onto the ϕ axis

Figure 7.11: Vertical (azimuthally, ϕ, aligned), polariser position projections of the angular distributions.

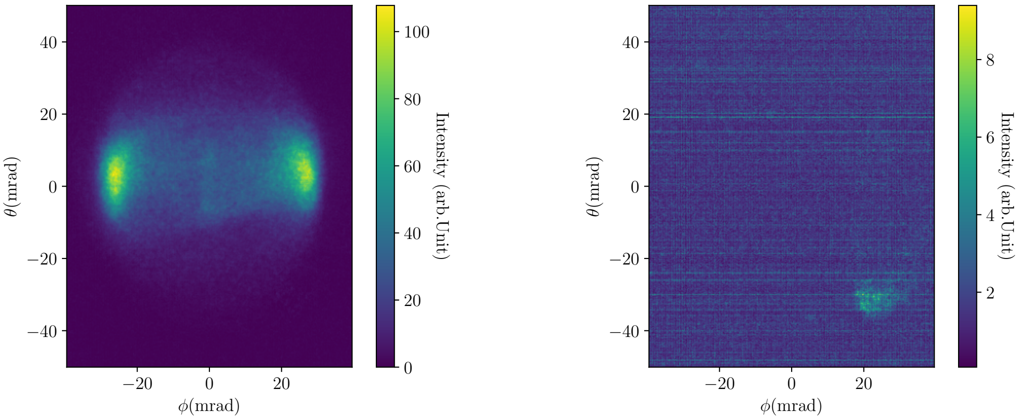

(a) Angular distribution. **(b)** Subtracted background.

Figure 7.12: Horizontal (polar, θ, aligned) polarisation angular distribution image stack, measured at a mean impact parameter of approximately 1880 ± 120 µm.

a much more drastic change is expected. It is believed that due to the multiple reflections of the ChDR through the radiator there is a blending of the two polarisations explaining the side lobes and central lobe in both polarisations.

Figure 7.14 displays the impact parameter scans produced for the two polarisations. The PCA simulations in Chap. 5 have shown that the θ aligned vertical polarisation produces results that are higher in intensity than the ϕ aligned horizontal data, matching the behaviour is seen in Fig. 7.14.

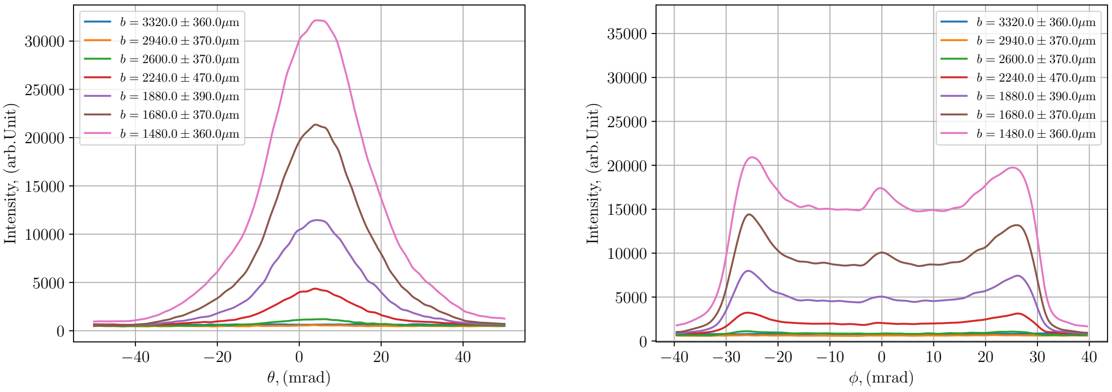

(a) Projection of ϕ onto the θ axis. **(b)** Projection of θ onto the ϕ axis.

Figure 7.13: Horizontal (polar, θ, aligned) polarisation projections of the angular distributions.

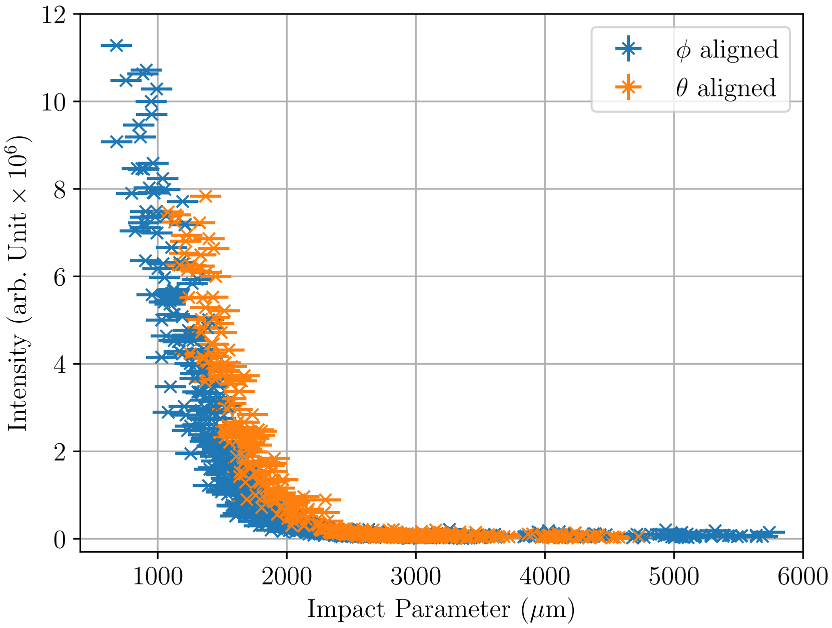

Figure 7.14: Polarised impact parameter responses, with a mean beam size of $\sigma_x = 1280 \pm 120\,\mu m$, and normalised to a bunch charge of 0.2 nC.

7.2.3 Bandpass Filtered Angular Results

The 550 and 400 nm bandpass filters are used to take wavelength specific measurements. Figure 7.15 shows the angular distribution and subtracted background for the 400 nm filter whereas Fig. 7.16 shows the the angular distribution and subtracted background for the 550 nm filter. Both bandpass filters shift the angular distribution emission angle in opposite directions on the polar axis.

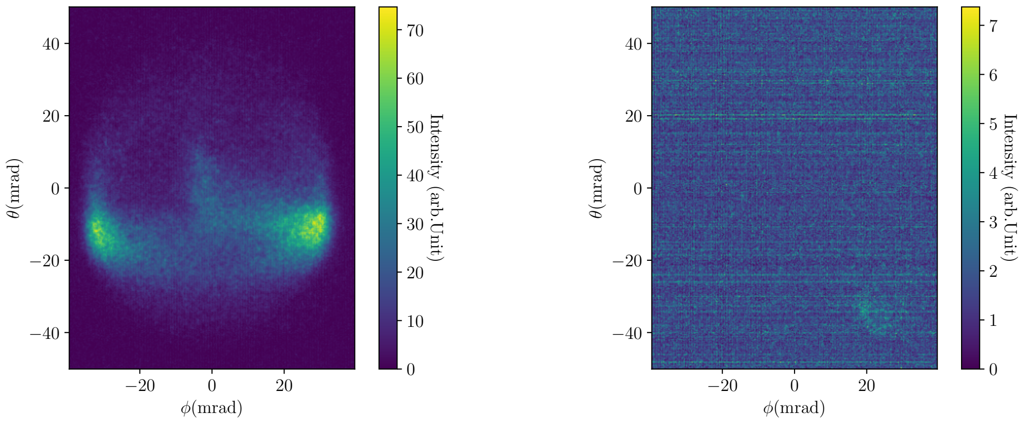

(a) Angular distribution.

(b) Subtracted background.

Figure 7.15: 400 nm bandpass filter angular distribution image stack, measured at a mean impact parameter of approximately 1840 ± 120 µm. Subtracted Background image stack measured at an impact parameter of approximately 7200 ± 350 µm

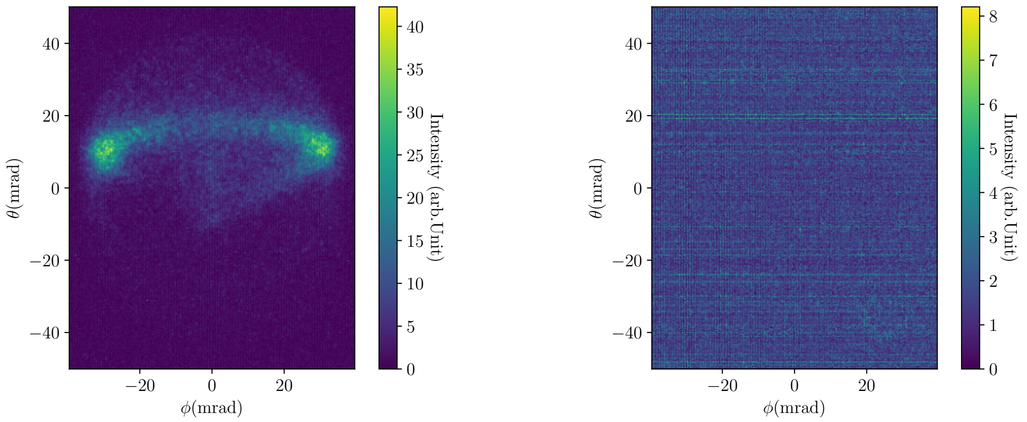

(a) Angular distribution.

(b) Subtracted background.

Figure 7.16: 550 nm bandpass filter angular distribution image stack, measured at a mean impact parameter of approximately 1840 ± 120 µm. Subtracted Background image stack measured at an impact parameter of approximately 7170 ± 330 µm.

Projections are produced for the bandpass filtered angular distributions at different impact parameters using the same process as Fig. 7.8. The projections of θ onto the ϕ axis appear quite similar between the two different wavelengths, whereas for the projection of ϕ onto the θ axis there is a shift of approximately 25 mrad between the peaks on the two datasets. For the projections in Fig. 7.17 and 7.18 signal can only clearly be seen in a few of the results. Where the results can be seen the distribution increases in intensity as the impact parameter decreases, but the overall shape stays the same.

The refractive index of the material diamond is wavelength dependent, additionally there are multiple reflections inside the accumulation radiator these angular shifts become exaggerated with each reflection causing a change in extraction angle at different wavelengths [70]. The rotation and alignment for these datasets was set for the unfiltered system before inserting the bandpass filters. When combining the intensifier and camera peak sensitivities the overall detector has a peak sensitivity between 400 and 500 nm. As the extraction angle is wavelength dependent, it makes sense that the unfiltered results produces a peak in-between the two bandpass filters.

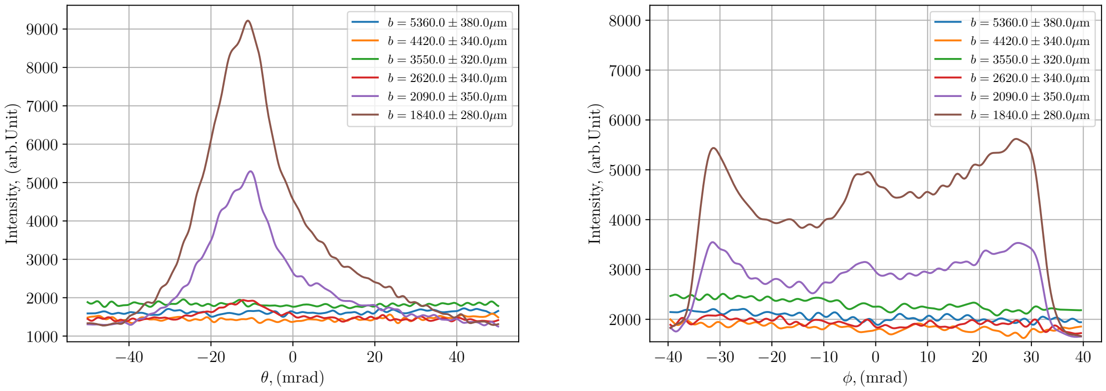

(a) Projection of ϕ onto the θ axis.

(b) Projection of θ onto the ϕ axis.

Figure 7.17: Projections of angular distributions that have been filtered by a 400 nm bandpass filter.

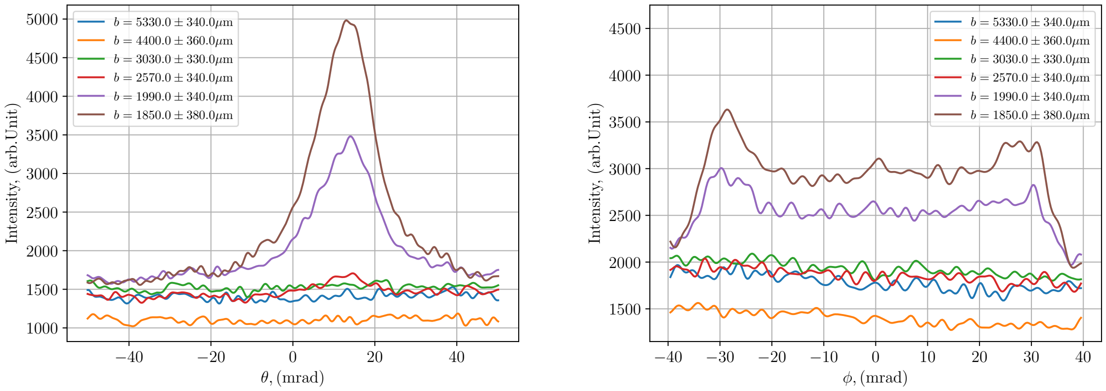

(a) Projection of ϕ onto the θ axis.

(b) Projection of θ onto the ϕ axis.

Figure 7.18: Projections of angular distributions that have been filtered by a 550 nm bandpass filter.

Figure 7.19 shows an impact parameter scan for the two bandpass filters produced using the same process as Fig. 7.9 but where each wavelength has been normalised to account for the sensitivity of the camera, the detector, and the bandpass filters.

The dominant wavelength in Fig. 7.19 is 400 nm, given the beam size and the impact parameters where signal is measured this is in agreement with simulations from Fig. 5.24. As the signal is not measured until the impact parameters are < 3 mm, there will be some signal contribution from direct CR that will favour the 400 nm wavelength.

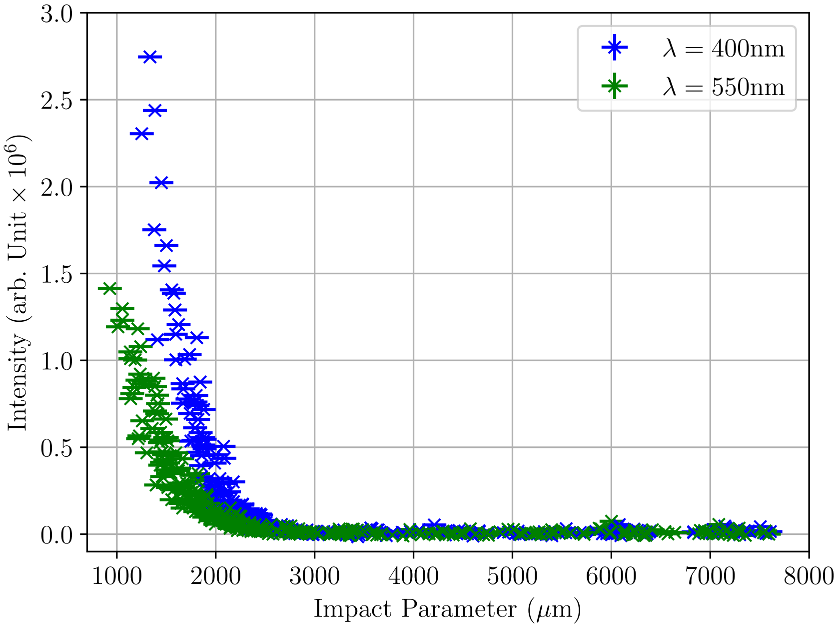

Figure 7.19: Bandpass filtered impact parameter responses, with a mean beam size of $\sigma_x = 1330 \pm 130\,\mu\text{m}$, and normalised to detector sensitivity and a bunch charge of 0.2 nC.

7.2.4 Angular Interpretation

There is strong evidence in these results to suggest that the signal measured is dominated by ChDR from halo particles. The impact parameter scans for the bandpass filters (see Fig. 7.19) are dominated by the plots that are simulated to be dominant at low impact parameter values, this suggests that the bulk of the beam is not contributing as much to the signal. All of the angular distribution projections produce a shape that appears to be impact parameter independent. The intensity of the projections increase as the impact parameter gets smaller, but when the signal is measured the shape does not get wider as the impact parameter gets smaller.

Figure 7.20 and 7.21 show the simulated single particle angular distributions for an impact parameter of 50 µm, and the wavelengths 400 and 550 nm respectively. The experimentally measured angular distributions and projections (see Fig. 7.15 and 7.17) are much wider and different in shape than those displayed in Fig. 7.20 and 7.21. This adds to the evidence that for the bandpass filter results, the signal is dominated by particles that are at very small impact parameters.

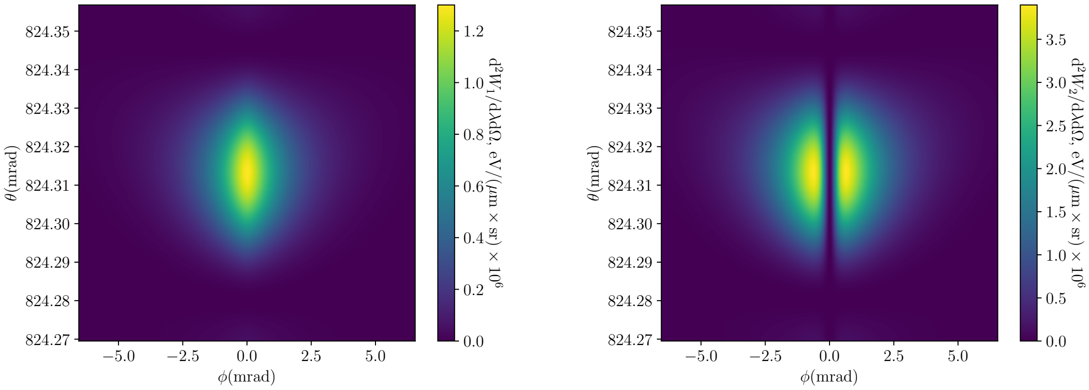

(a) Vertical polarisation. **(b)** Horizontal polarisation.

Figure 7.20: Single particle PCA angular distributions, simulated for the wavelength of 0.4 µm, impact parameter of 50 µm and parameters from Table. 5.2.

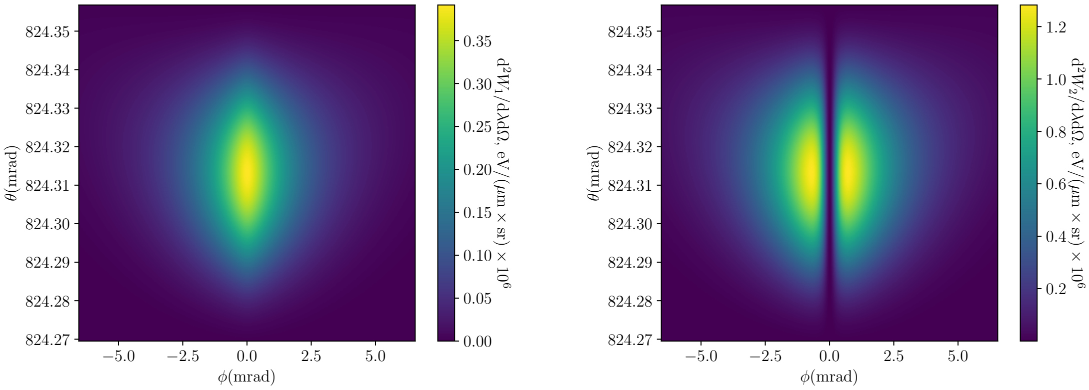

(a) Vertical polarisation. **(b)** Horizontal polarisation.

Figure 7.21: Single particle PCA angular distributions, simulated for the wavelength of 0.55 µm, impact parameter of 50 µm and parameters from Table. 5.2.

Part of the increase in the angular distribution size in the polar plane is thought to be due to the wavelength dependent extraction angle. This shift is caused by the wavelength dependent refractive index of the radiator combined with the multiple reflections inside the radiator, and potential destructive interference that could occur inside the radiator.

The polarised projections do not show the distinct different shapes predicted by the PCA model, but there is a change in the peak to sideband ratio for each polarisation that shows the two polarisations are different. As the change of shape is not as great as assumed from the simulations the interpretation is that the multiple reflections inside the accumulation radiator has produced a strong coupling between the two polarisations but not an entire melding.

Overall the angular distribution shapes are far different than expected and the signal favours the shorter wavelength contribution. The wavelength contribution can be explained by a signal that is dominated by the halo particles and not the beam core (see Fig. 5.24). For the angular distribution size this will be due to the radiator geometry. The assumption is that the key different geometric factor is the radiator height, and not that the shape is an accumulation radiator instead of prismatic. By having this limiting size the signal is reduced, and a potential decay factor is introduced, by increasing the radiator height these factors can be reduced or removed.

7.3 Photomultiplier

The PMT data has been taken with the detector and optical system described in Sec. 3.2.5. The datasets taken with the PMT were limited, the majority of the experimental shifts were used to commission the Diamond BTS and characterise the radiator with the ProxiVision camera. The remaining supplementary shifts were used for the PMT experiments. The PMT is sensitive to longer wavelengths than the camera in an attempt to measure ChDR at larger impact parameters.

7.3.1 Unfiltered Photomultiplier Tube Results

An impact parameter scan was taken using the standard BTS beam parameters from Table. 3.1 and a single bunch extraction charge set at approximately 0.15 nC. The PMT data acquisition system was set with a decimation of 1 and the PMT gain voltage set at 0.65 V.

Using no filters or polarisers the beam was bumped towards the target and 25 measurements were taken at each magnet bump setting. For each dataset the first extraction was discarded as the first extraction is needed as a warm-up extraction for the beam position to settle. Figure 7.22 shows the impact parameter scan. Each extraction is shown as a separate point on the graph where the intensity has been linearly normalised to a bunch charge of 0.15 nC.

The gap in impact parameter data between 4 and 5 mm is there because a large bump setting was used between these points. At impact parameters ≤ 3 mm the signal can be measured. Comparing the fit for the unpolarised dataset with that in Fig. 7.9 similar results is shown where signal also cannot be seen until the impact parameter is ≤ 3 mm.

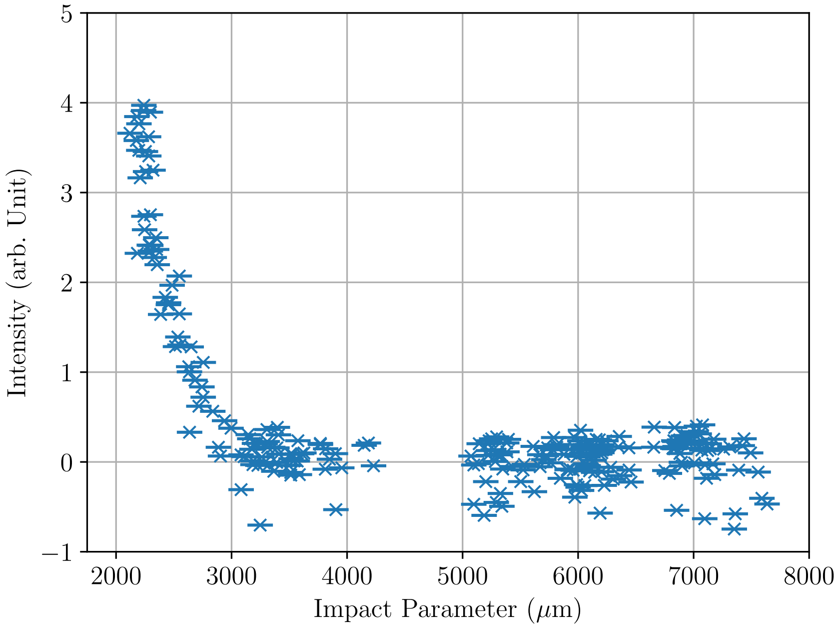

Figure 7.22: Unpolarised impact parameter scan taken with the PMT and a beam size of approximately 1300 ± 115 µm, linearly normalised to a bunch charge of 0.15 nC.

7.3.2 Bandpass Filtered Photomultiplier Tube Results

Examining simulations taken in Fig. 5.24 the ideal parameters for measuring the beam core with ChDR are a beam of small size and with detector sensitive to long wavelengths. The ideal working region is similar to that found in Fig. 5.24 when the σ_x beam size is ≤ 800 µm where the wavelength dependence moves in the opposite direction to CR. To obtain a small beam size the beam profile adjustment codes described in Sec. 4.3.2 were used. Figure 7.23 shows an a example beam profile taken from OTR2 for the bandpass datasets. The beam profile settings were not altered from these positions giving a horizontal beam size, σ_x, of approximately 350 ± 95 µm.

Impact parameter datasets were taken for five bandpass filters between impact parameters of 4 and 7 mm. The gain of the PMT was increased to 0.7 V for these scans (see Fig. 3.20). The impact parameter was calculated using the data from OTR2 and the IBPM. The raw PMT data for each impact parameter and wavelength can be seen in Fig. 7.24. Examining the data there are higher results from the 550 nm data, and lower results from the 800 nm datasets.

To fairly compare the different wavelengths the transmission quality of the bandpass filters and the sensitivity of the PMT need to be accounted for. Figure 7.25 shows the different

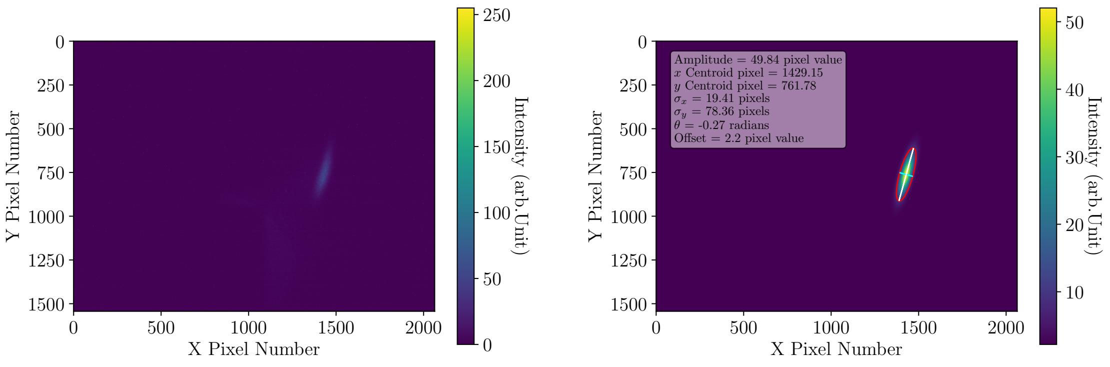

(a) Raw image. **(b)** 2D Gaussian fit.

Figure 7.23: Example OTR2 image from PMT bandpass datasets with 2D Gaussian fit.

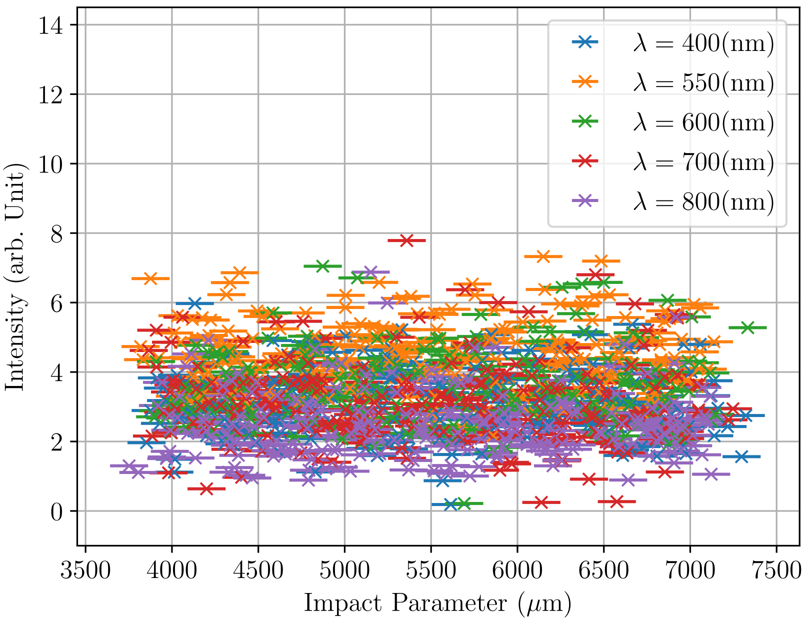

Figure 7.24: Unprocessed PMT data sets taken with the PMT with impact parameters calculated using OTR2 and IBPM.

bandpass filters and the sensitivity of the PMT displayed together.

By convolving the sensitivity with the different filters a normalisation scaling is obtained for the different filters and displayed in Table. 7.1. The different wavelengths have been normalised to 700 nm as this provides the highest sensitivity of the filters. The scaling factor is much larger for the 400 nm dataset, as the SNR is poor at these large impact parameters this dataset is excluded after processing. The amplification of the remaining noise on the signal makes the entire dataset significantly larger than all of the others where it is not

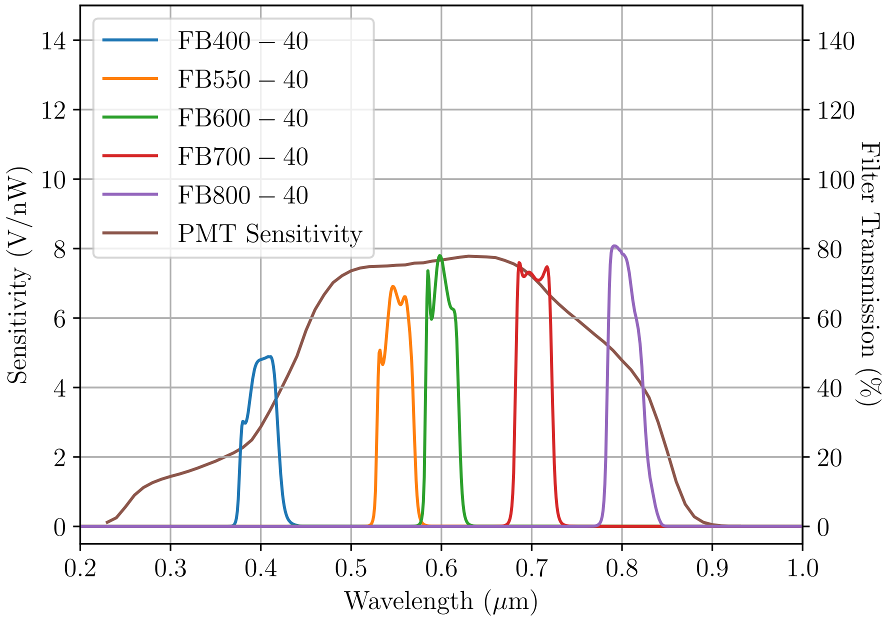

Figure 7.25: Spectral response of the Hamamatsu H10722-20 PMT and transmission for a range of Thorlabs bandpass filters [59, 61].

believed this is the actual case.

Central filter wavelength (nm)	Normalisation Factor
400	3.94
550	1.14
600	1.09
700	1.0
800	1.49

Table 7.1: Normalisation factors to scale PMT sensitivity and bandpass transmission to that of the 700 nm filter [61].

Figure 7.26 shows the same data as Fig. 7.24 with the data linearly normalised for bunch charge and detector sensitivity from Table. 7.1. Additionally data taken at the furthest bump setting (the data at approximately 7 mm) was averaged to perform a background subtraction for each wavelength before scaling. The datasets that dropped to zero or below when the background subtraction was applied were removed as negative numbers have no meaning in this context.

The data in Fig. 7.26 has shifted but does not clearly show what wavelengths are favoured. To better represent this data each dataset has been put into a histogram and displayed in Fig. 7.27 to 7.30. Examining the histograms the dataset that has the least number of measurements in the lowest bin is that for 700 nm from Fig. 7.29. The next dataset that has the least number of measurements in the lowest bin is that for 550 nm from Fig. 7.27. Given

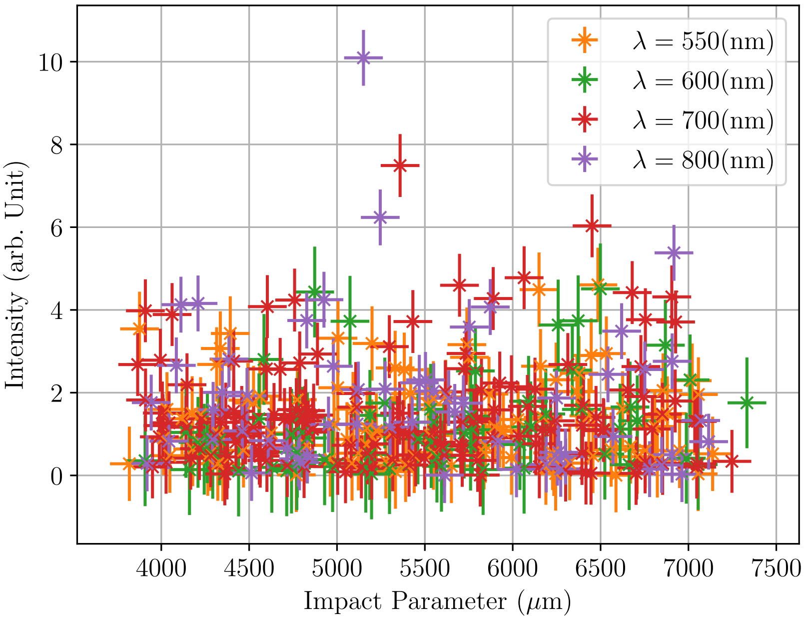

Figure 7.26: Processed PMT data sets taken with the PMT with impact parameters calculated using OTR2 and the IBPM.

that these datasets are not next to each other it is hard to draw any certain conclusions from these measurements. It is highly likely that the SNR in these measurements is too low, especially given that the simulation in Fig. 5.24 predicts that the signals should be different by orders of magnitude.

7.3.3 Photomultiplier Tube Interpretation

Interpreting the results taken with the PMT it is clear that the impact parameter data when taken with the unpolarised data does not allow for signal to be detected at larger impact parameters than the ProxiVision camera. As the PMT detector is more sensitive than the ProxiVision camera this adds to the theory that there maybe something with the setup that is limiting generation or extraction of ChDR.

Interesting results come from the PMT bandpass results. Given that without any scaling there are differences between the different wavelengths it is showing that a wavelength dependent signal is being measured. when accounting for the scaling of the detector sensitivity and bandpass filter transmission the data does shift, but given the results in Fig. 7.27 to 7.30 a clear trend cannot be deduced from these datasets.

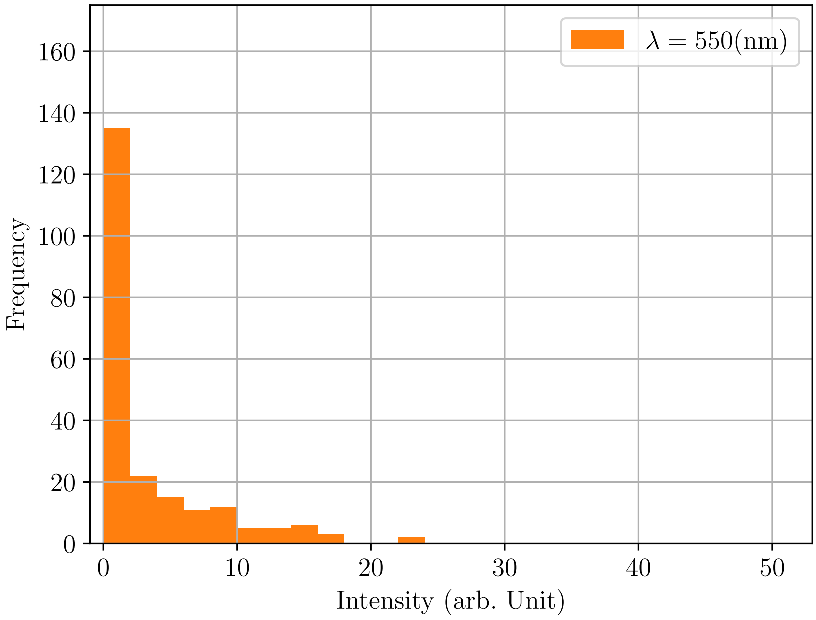

Figure 7.27: Histogram showing the intensity distribution generated from the 550 nm dataset in Fig. 7.26.

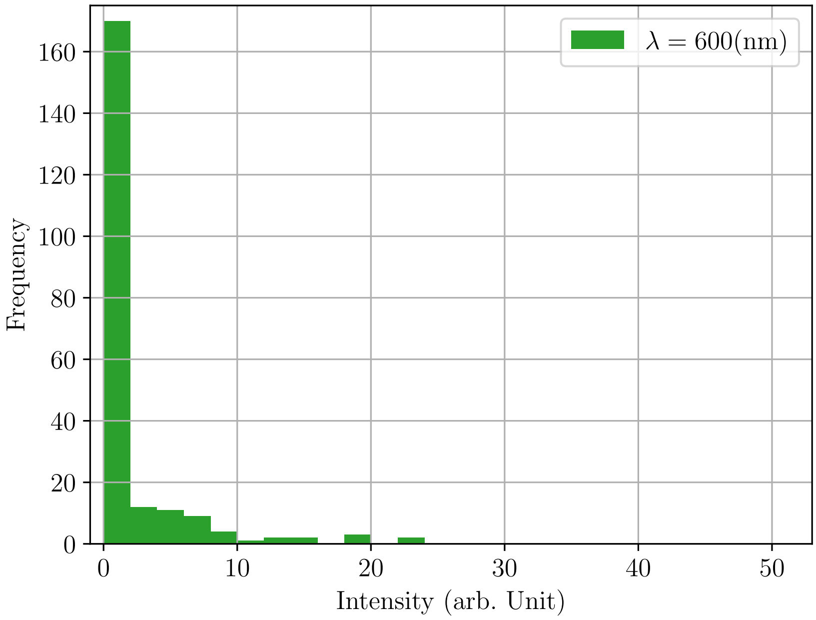

Figure 7.28: Histogram showing the intensity distribution generated from the 600 nm dataset in Fig. 7.26.

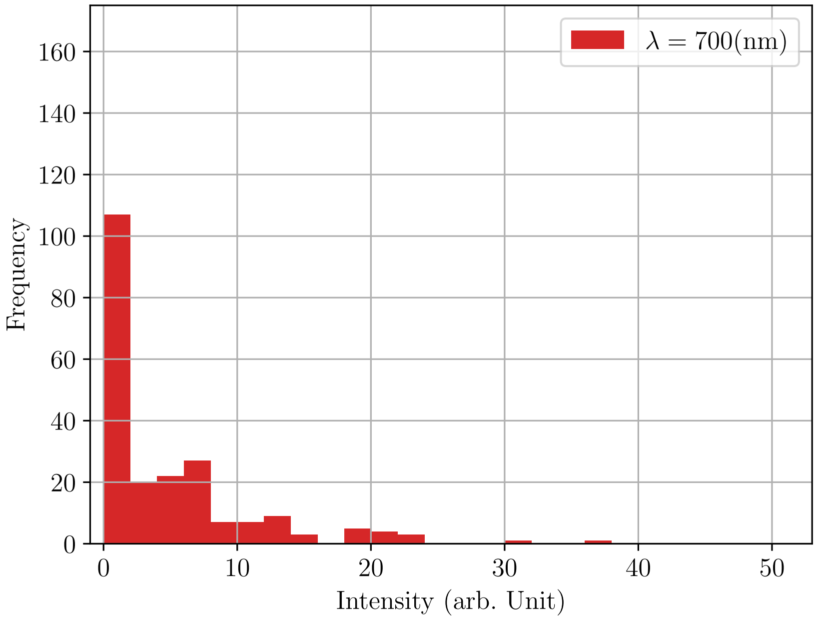

Figure 7.29: Histogram showing the intensity distribution generated from the 700 nm dataset in Fig. 7.26.

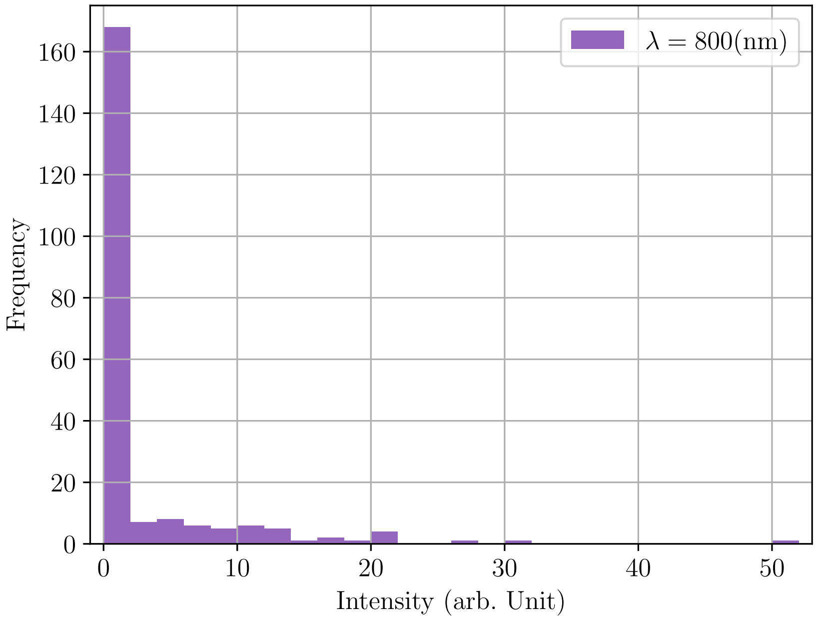

Figure 7.30: Histogram showing the intensity distribution generated from the 800 nm dataset in Fig. 7.26.

7.4 Comparison

Comparing the different measurement systems and techniques a lot can be learned. Looking at the unpolarised impact parameter scans from the imaging, angular, and PMT detection systems (see Fig. 7.3, 7.9, and 7.22) signal cannot be detected until the impact parameter drops below 3 mm. This is a common trait between the imaging, angular, and PMT detection systems. As the signal appears at the same location for all datasets this lends to the theory that the signal is dominated by signal from the beam halo at very low impact parameters. This is also a region where some particles will directly contact the radiator and could produce CR. If the signal had a strong ChDR contribution from the beam core in this location the PMT should detect the signal at higher impact parameters than the other two systems but it does not.

Given that the target height is 2 mm and not more there will be some signal degradation as the target will not intercept more of the beam field (see Sec. 3.2.1). This could be one parameter that if changed could greatly increase the signal amplitude. If as suspected this is the case then increasing the detected wavelength would not increase the signal as desired. Given that the radiator height must be several times larger than the effective electron radii (see Eq. 2.8) the desired radiator height would scale with the wavelength implying that the potential decay factor will scale inversely. This may explain why a conclusive signal difference is not seen in Fig. 7.26.

CHAPTER 8

CONCLUSION

8.1 Discussion

This chapter evaluates the results and simulations developed and discusses the progress made towards the development of an incoherent ChDR BPM. It also examines the future work that is planned for ChDR experiments at Diamond and some of the circumstances that prevented this work occurring for this thesis.

8.1.1 Critical Analysis

A critical hypothesis of the experimental data in this thesis would be to question that a BPM experiment that measured signal from the beam core was not achieved. Simulations produced in Chap. 5 show that halo particles produce ChDR that behave spectrally similar to CR, this adds evidence to prove that ChDR will make up the measured signal, even if the spectral dependence initially goes against this. The results in Sec. 7.3.2 are inconclusive, while they do not definitively measure higher signal at longer wavelengths they do not measure the opposite either suggesting there are issues with the experimental setup and the SNR.

The default beam conditions in the BTS are not favourable for ChDR research for the detector that is installed. The goal of this research was to produce data and results to be used for the design and development of a non-invasive BPM. What has been shown here, is that even with a sensitive PMT measuring ChDR at large impact parameters is difficult when performing bunch-by-bunch measurements. The largest impact parameter measured reliably is approximately 3 mm. A more sensitive radiator or detection system could improve on this. Section 7.3.2 demonstrates that some signal is potentially measured at larger impact parameters as the data is not flat for all samples.

In order to use ChDR as a BPM, signal detection needs to be made at larger impact parameters with small beam sizes. This was not achieved for this research project, but the data taken and analysis performed constructively contributes towards this goal.

8.1.2 Experimental Limitations

During this thesis experiments have taken place on the Diamond Light Source BTS. These experiments have happened when the accelerator is being run-up just after a shutdown period, or during a user-run on Machine Development (MD) days. Unfortunately these experimental shifts have not been available during the entire research period.

During the second year of this research the extraction septum magnet of the Booster synchrotron suffered a failure, this caused a six month delay to experimental work on the BTS for this thesis. Once the experiments could be carried out again the running procedure had to be changed, setting a fixed number of 3000 extractions per experimental shift to limit the use of the septum magnet. This research project also took place during the emergence of Covid-19 pandemic [74]. The pandemic initially limited access to the Diamond site causing an additional six month delay to experiments on the BTS.

Due to the experimental delays caused by the broken septum magnet and the Covid-19 pandemic, more experimental shifts were made available during the later part of this research project. While these shifts allowed for data to be taken it did not allow for the same number of improvement iterations of the experimental station that would have been possible otherwise.

8.1.3 Future Work

There are many other ChDR BPM experiments that can take place on the Diamond BTS. The simplest would be keeping the same experimental setup and taking more results with the Hamamatsu PMT. More in depth impact parameter scans could be performed under different beam conditions such as different beam profiles. The Red Pitaya DAQ system has an analogue output used to control the PMT gain. A simple but potentially large improvement to the system would be to reduce the noise on the gain voltage set from the Red Pitaya. As the Red Pitaya is located outside the accelerator tunnel in the CIA it is approximately 20 m from the PMT. Having the two systems so far apart increases the noise generated on the analogue output channel and will force the PMT gain to fluctuate. Given that the PMT gain is very sensitive (see Fig. 3.20b) moving the Red Pitaya system to the electronics rack in the BTS such that the cable length is < 5 m could reduce this.

A way to improve the current system would be to change the PMT. The current Hamamatsu-H10722 has a bandwidth of 20 kHz, which given the short bunch length will struggle with the rapid signal change of the bunch. This may occur as an elongation of the signal or potentially as a clipping. Elongating would not change much for the way this system is run and analysed, but signal clipping would. An example PMT that could be used is a Hamamatsu-H15460-40, which has a similar spectral response range to the Hamamatsu-H10722 but with a larger sensor area and a bandwidth of 30 MHz [75]. This PMT was considered for this research project initially, but the cost was considered prohibitive without any initial PMT data.

As detailed in this research project the dimensions of the radiator used (see Fig. 3.7) are not ideal for the BTS beam parameters. One proposed upgrade that was not undertaken due to experimental delays was an upgrading of the target. A fused silica accumulation radiator shown in Fig. 8.1 has been manufactured and used at the CLEAR facility [76].

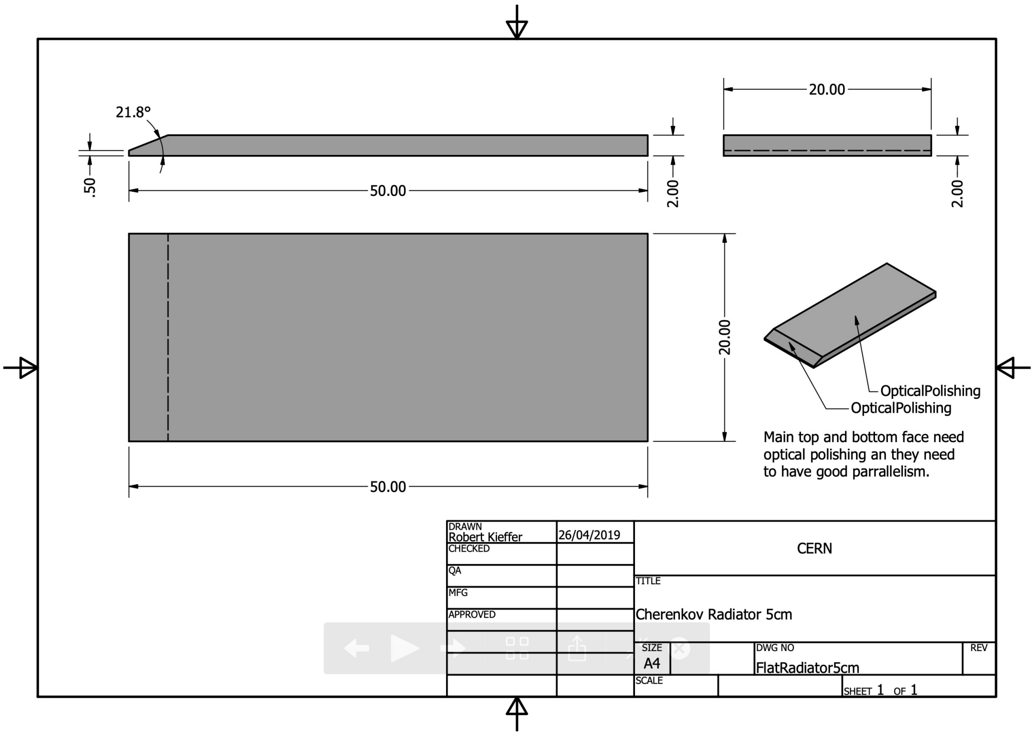

Main top and bottom face need optical polishing an they need to have good parralelism.

DRAWN Robert Kieffer 26/04/2019
CHECKED
QA
MFG
APPROVED
CERN
TITLE Cherenkov Radiator 5cm
SIZE A4
DWG NO FlatRadiator5cm
REV
SCALE
SHEET 1 OF 1

Figure 8.1: Updated ChDR radiator design [57].

One of these radiators could be installed on the BTS to theoretically improve the photon yield. Discussions in Sec. 3.2 have stated that due to the effective electron radius size (see Eq. 2.8) and the vertical beam size, the radiator height will have had a negative effect on the results taken for this thesis. Increasing the radiator height would allow the experiment to more closely match the simulation parameters and to increase the beam coverage. Increasing length also means the electrons will travel parallel to the radiator for a greater distance. Figure 8.2 shows a single particle spectral response at an impact parameter of 1 mm from the radiator installed on the BTS and the new proposed radiator in Fig. 8.1. The new radiator design produces signal that is approximately 4 times greater. Given that this simulation only accounts for the increase in length and not the height experimentally the increase should be even greater than this.

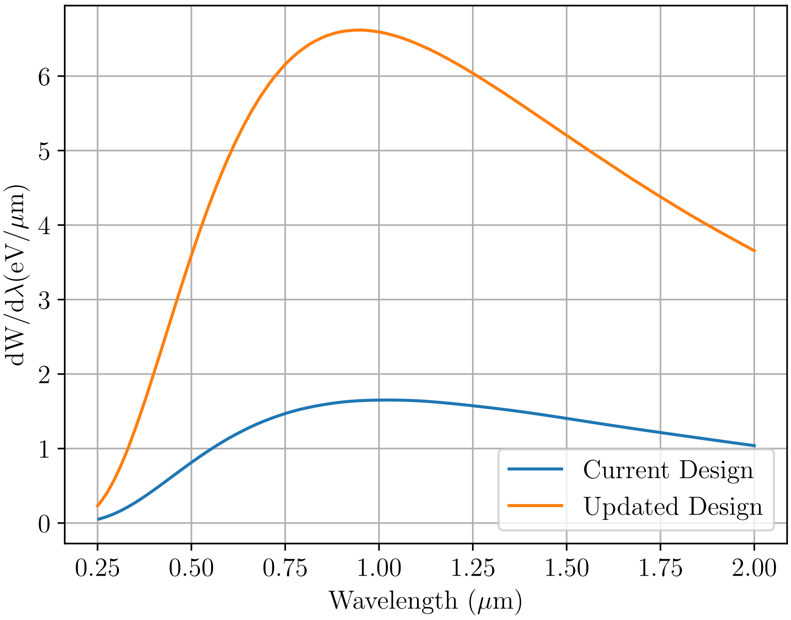

Figure 8.2: Single particle spectral response from a 3 GeV electron at an impact parameter of 1 mm for the ChDR radiator design used installed on the Diamond BTS and the updated design from Fig. 8.1.

When using an accumulation radiator with the PCA theory there are a large number of unknowns potentially caused by multiple reflections inside the radiator such as destructive interference effects. An alternative next step would be to return to a prismatic target like the experiments performed in [31]. The PCA theory has been developed for prismatic radiators, and not accumulation radiators. Using a prismatic radiator allows for a more direct comparison with experiment and simulation.

Finally additional studies into coherent ChDR or plasmonic ChDR could also be carried out on the Diamond BTS, like those that have taken place at CLEAR [76]. While the bunch length of Diamond does not lend itself to these studies there is the potential to use these as a way of increasing the signal from a ChDR BPM pickup. However given that the radiator height is a potential limiting factor that scales with the effective electron radius, it would be recommended to examine a target with a larger height in the incoherent range first.

8.1.4 Conclusion

The motivation for this thesis was to perform research that would contribute to the development of a ChDR BPM. As part of the ChDR collaboration the results taken on the Diamond BTS can be used to better understand ChDR and how it can be used for beam diagnostics.

The data taken for this research project has been done to a high standard, simulations have been performed and used to compare against experimental data. While the experimental data has not demonstrated a method of adequately measuring the beam position using ChDR, this research has informed the direction that future ChDR experiments could take. It has also highlighted beam parameters and conditions that are of vital importance to ChDR BPM development.

BIBLIOGRAPHY

[1] G. Golluccio, P. Arpaia, and M. Buzio, “Measurement of eddy current transients in fast-cycled linac quadrupole magnets at CERN”, in *Proc. 19th Fundamental and Applied Metrology Conf. (XIX IMEKO’09)*, Lisbon, Portugal, Sep. 2009, pp. 652–656.

[2] E. Wilson, “An Introduction to Particle Accelerators”, Oxford, U.K. Oxford University Press, 2001, pp. 87-88, 111-113.

[3] T. Shaftan, “Joint CFN and NSLS-II Synchrotron Lecture Series: Synchrotron Radiation”, Nov 2015, Accessed on: Jan 6, 2020. [Online]. `https://www.bnl.gov/ps/userguide/lectures/Lecture-2-Shaftan.pdf`.

[4] Diamond Light Source Ltd, “Diamond-II — Conceptual Design Report”Oxford, U.K. May, 2019, Accessed on: Jan 6 2020 [Online]. Available: `https://www.diamond.ac.uk/Home/About/Vision/Diamond-II.html` pp. 3–4, 32, 70–71.

[5] European XFEL, “Overview of European XFEL data, Trains and pulses”, Accessed on: Aug 15, 2022. [Online]. Available: `https://rtd.xfel.eu/docs/data-analysis-user-documentation/en/latest/overview.html`.

[6] Diamond Light Source Ltd, “Bird’s eye view of the synchrotron”, Accessed on: Jan 6, 2020. [Online]. Available: `https://www.diamond.ac.uk/Science/Machine/Components.html`.

[7] F. Fiuza, L. O. Silva, and C. Joshi, “High-brilliance synchrotron radiation induced by the plasma magnetostatic mode,” *Phys. Rev. Special Topics - Accelerators and Beams*, vol. 13, p. 080701, Aug 2010.

[8] CERN, “LHC report: Full house for the LHC”, Jul 4, 2017. Accessed on: Jan 6, 2020. [Online]. Available: `https://home.cern/news/news/accelerators/lhc-report-full-house-lhc`.

[9] K. B. Scheidt, “Complete Test Results of New BPM Electronics for the ESRF New LE-Ring”, in *Proc. 7th Int. Beam Instrumentation Conf. (IBIC’18)*, Shanghai, China, Sep. 2018, pp. 257–260.

[10] D. Bulfone, “Overview of Fast Beam Position Feedback Systems”, in *Proc. 11th European Particle Accelerator Conf. (EPAC’08)*, Genoa, Italy, Jun. 2008, paper TUZM02, pp. 1021–1025.

[11] D.A. Fleisch, “A Student’s Guide to Maxwell’s Equations”, Cambridge University Press, Cambridge, UK; New York 2008 p. 5.

[12] R. Feynman, “The Feynman Lectures on Physics Vol. II Ch. 26: Lorentz Transformations of the Fields”, 2013, Accessed on: Jan 6, 2020. [Online] Available at: `https://www.feynmanlectures.caltech.edu/II_26.html`.

[13] K. M. Hock and A. Wolski, “Transient jitter from injection in storage rings,” *Phys. Rev. ST Accel. Beams*, vol. 12, pp. 1036–1041, Sep 2009.

[14] Y. Kurimoto, *et al*, “Real-time betatron tune correction with the precise measurement of magnet current,” *IEEE Transactions on Nuclear Science*, vol. 66, p. 1036–1041, Jul 2019.

[15] K. Li, Proceedings of the 2021 CERN–Accelerator School Introductory Course 2021, Chavannes de Bogis (Switzerland), pp. 1, 9, 25–28, arXiv:2107.06109 [physics.acc-ph].

[16] H. Schmickler, “Beam Position Measurement System Design”, in *Proc. 4th Int. Beam Instrumentation Conf. (IBIC’15)*, Melbourne, Australia, Sep. 2015, pp. 618–624.

[17] P. Forck, “Joint University Accelerator School, Lecture Notes on Beam Instrumentation and Diagnostics”, Darmstadt, Germany, Jan–Mar, 2017, pp. 10–18, 88–90.

[18] M. Wendt, Proceedings of the 2018 CERN–Accelerator–School course on Beam Instrumentation, Tuusula, (Finland), pp. 1–30, arXiv:2005.14081 [physics.acc-ph].

[19] S. Varnasseri, *et al.*, “Design and fabrication of stripline BPM for the ESS MEBT,” *Nuclear Instruments and Methods in Physics Research A*, vol. 987, p. 164835, Jan. 2021.

[20] M. Wendt, *et al.* “A High Resolution Cavity BPM for the CLIC Test Facility”, Contribution to *14th Beam Instrumentation Workshop (BIW10)*, Santa Fe, New Mexico, May 2010, `https://doi.org/10.48550/arXiv.1207.4768`.

[21] J.J. Garcıa-Garrigos, “Development of the Beam Position Monitors for the Diagnostics of the Test Beam Line in the CTF3 at CERN”, Ph.D thesis, Polytechnic University of Valencia, Department of Electronic Engineering, May, 2013, pp. 14, 39–48.

[22] L. Byoungho, “Review of the present status of optical fiber sensors. optical fiber technology 9,” *Optical Fiber Technology*, vol. 9, pp. 57–79, 04 2003.

[23] S. Schulz, *et al.* “Femtosecond all-optical synchronization of an X-ray free-electron laser”. *Nat Commun 6*, 5938 (2015).

[24] A. Bravin, Proceedings of the 2018 CERN–Accelerator–School course on Beam Instrumentation, Tuusula, (Finland), pp. 11–16, arXiv:2005.07400 [physics.acc-ph].

[25] L. Bobb, “Feasibility of Diffraction Radiation for Non-invasive Micron-scale Transverse Beam Size Measurement in Circular Machines ”, Ph.D thesis, Royal Holloway, University of London, Department of Physics, Aug, 2016, pp. 70, 80–83.

[26] T. Lefevre, *et al.*, “Cherenkov Diffraction Radiation as a tool for beam diagnostics”, presented at the 8th Int. Beam Instrumentation Conf. (IBIC’19), Malmö, Sweden, Sep. 2019, paper THAO01.

[27] U. Iriso, G. Benedetti, and F. Peréz, “Experience with YAG and OTR Screens at ALBA”, in *Proc. 9th European Workshop on Beam Diagnostics and Instrumentation for Particle Accelerators (DIPAC’09)*, Basel, Switzerland, May 2009, paper TUPB15, pp. 200–202.

[28] A. H. Lumpkin, W. Berg, D. W. Rule, N. Sereno, B. X. Yang, and C. Yao, “Non-intercepting Beam Size and Position Monitor Using ODR for X-Ray FELs”, in *Proc. 28th Int. Free Electron Laser Conf. (FEL’06)*, Berlin, Germany, Aug.-Sep. 2006, paper THPPH055, pp. 710–713.

[29] A. P. Potylitsyn, M. I. Ryazanov, M. N. Strikhanov, A. A. Tishchenko, *Diffraction Radiation from Relativistic Particles.* Springer Tracts in Modern Physics 239, Springer-Verlag Berlin Heidelberg, 1 ed., 2011.

[30] A.S. Konkov, *et al.* “Theoretical model for incoherent Cherenkov diffraction radiation Report II”, Tomsk Polytechnic University Internal Report, Apr. 2018.

[31] R. Kieffer, *et al.*, “Direct Observation of Incoherent Cherenkov Diffraction Radiation in the Visible Range,” *Phys. Rev. Lett.*, vol. 121, p. 054802, Aug 2018.

[32] V.L. Ginzburg, and I.M. Frank, “Radiation of a uniformly moving electron due to its transition from one medium into another,” *J. Phys. (USSR)*, vol. 9, pp. 353–362, 1945.

[33] P. A. Cerenkov, “Visible radiation produced by electrons moving in a medium with velocities exceeding that of light,” *Phys. Rev.*, vol. 52, pp. 378–379, Aug 1937.

[34] S. J. Smith, and E. M. Purcell, “Visible light from localized surface charges moving across a grating,” *Phys. Rev.*, vol. 92, pp. 1069–1069, Nov 1953.

[35] D. V. Karlovets, and A. P. Potylitsyn, “Diffraction radiation from a finite-conductivity screen,” *JETP Letters*, vol. 90, pp. 326–331, Nov 2009.

[36] K. O. Kruchinin, and D. V. Karlovets, “Development of the theory of diffraction radiation from surfaces with finite conductivity,” *Russian Physics Journal*, vol. 55, pp. 9–16, June 2012.

[37] M. V. Shevelev, and A. S. Konkov, “Peculiarities of the generation of Vavilov-Cherenkov radiation induced by a charged particle moving past a dielectric target,” *JETP*, vol. 118, pp. 501–511, Apr. 2014.

[38] M. Shevelev, A. Konkov, and A. Aryshev, “Soft-x-ray Cherenkov radiation generated by a charged particle moving near a finite-size screen,” *Phys. Rev. A*, vol. 92, p. 053851, Nov 2015.

[39] V. Bleko, *et al.*, “Coherent Cherenkov radiation as an intense THz source,” *Journal of Physics: Conference Series*, vol. 732, Aug. 2015. 11th International Symposium on Radiation from Relativistic Electrons in Periodic Structures, RREPS 2015.

[40] A. S. Konkov, A. P. Potylitsyn, M. V. Shevelev, and A. S. Aryshev, “On the polarization characteristics of Cherenkov radiation from a dielectric screen,” *JETP Letters*, vol. 105, pp. 227–231, Feb 2017.

[41] I. Tamm, “Radiation emitted by uniformly moving electrons,” *Journal of Physics (USSR)*, vol. 1, pp. 439–454, 1937.

[42] Y. Hu, Z. Li, B. Wetzel, R. Morandotti, Z. Chen, and J. Xu, “Cherenkov Radiation Control via Self-accelerating Wave-packets,” *Scientific Reports*, vol. 7, p. 8695, Aug. 2017.

[43] C. Bartels, J. Ebert, A. Hartin, C. Helebrant, D. Käfer, J. List, “Design and construction of a Cherenkov detector for Compton polarimetry at the ILC,” *Journal of Instrumentation*, vol. 7, pp. P01019–P01019, Jan 2012.

[44] P. V. Karataev, “Pre-wave zone effect in transition and diffraction radiation: Problems and solutions,” *Phys. Lett. A*, vol. 345, no. 4, pp. 428 – 438, 2005.

[45] T. Lefevre *et al.*, “Non-invasive Beam Diagnostics with Cherenkov Diffraction Radiation”, in *Proc. 9th Int. Particle Accelerator Conf. (IPAC’18)*, Vancouver, Canada, Apr.-May 2018, pp. 2005–2008.

[46] T. Lefevre *et al.*, "Cherenkov Diffraction Radiation From Long Dielectric Material: An Intense Source of Photons in the NIR-THz Range", in *Proc. 8th Int. Particle Accelerator Conf. (IPAC'17)*, Copenhagen, Denmark, May 2017, pp. 400–403.

[47] S. Ninomiya *et al.*, "Measurement of Cherenkov Diffraction Radiation from a Short Electron Bunches at t-ACTS", in *Proc. 10th Int. Particle Accelerator Conf. (IPAC'19)*, Melbourne, Australia, May 2019, pp. 2536–2538.

[48] C.Z. Tan, "Determination of refractive index of silica glass for infrared wavelengths by ir spectroscopy," *Journal of Non-Crystalline Solids*, vol. 223, no. 1, pp. 158 – 163, 1998.

[49] E. Hecht, "Optics, Global Edition", Pearson Education Limited, 2016, pp. 109, 170–173.

[50] S. Mazzoni, *et al.*, "Recent Results on Non-invasive Beam Size Measurement Methods Based on Polarization Currents", in *Proc. IBIC'18*, Shanghai, China, Sep. 2018, pp. 464–467. `doi:10.18429/JACoW-IBIC2018-WEPB14`.

[51] Argonne National Laboratory, "Experimental Physics and Industrial Control System", Accessed on: Aug 5, 2020. [Online]. Available: `https://epics.anl.gov/`.

[52] L. Bobb, "Parameters for Experimental Proposals in Booster-to-Storage Ring (BTS) Test Stand at Diamond Light Source", Diamond Light Source, May 2017, Unpublished.

[53] I. Martin, private communication, Oct, 2022.

[54] Keysight, "Keysight Technologies Infiniium 90000 Series Oscilloscope", datasheet, pp. 19.

[55] C. Wiebers, M. Holz, G. Kube, D. Noelle, G. Priebe, and H.-Ch. Schroeder, "Scintillating Screen Monitors for Transverse Electron Beam Profile Diagnostics at the European XFEL", in *Proc. IBIC'13*, Oxford, UK, Sep. 2013, paper WEPF03, pp. 807–810.

[56] Astropy, "Gaussian2D", Accessed on: Aug 5, 2020. [Online]. Available: `https://docs.astropy.org/en/stable/api/astropy.modeling.functional_models.Gaussian2D.html`.

[57] R. Kieffer, private communication, Apr. 2019.

[58] ProxiVision, "ProxiKit Package", ProxiVision SN 8806003 Manual, Version 1.0, Oct. 2012.

[59] Thorlabs, "Optics Manufacturing", Product Catalogue, Version 21.3, pp. 809–810, 911.

[60] Allied Vision, "GigE Vision camera with Sony ICX285 CCD sensor"Manta G-145B-30fps datasheet, Version 4.9.3.

[61] Hamamatsu, "Photosensor Modules H10722 Series", datasheet, TPMO1063E02, pp. 1–4, 911.

[62] RedPitaya, "Red Pitaya 125-10 Documentation", datasheet, Release 0.97, Jan. 2022.

[63] M. Bergamaschi, "Development of a combined transition and diffraction radiation station for non-invasive beam size monitoring on linear accelerators ", Ph.D thesis, Royal Holloway, University of London, Department of Physics, Oct, 2018, pp. 32-33.

[64] L. Garolfi *et al.*, "Beam Dynamics Studies and Instrumentation Tests for Bunch Length Measurements at CLEAR", in *Proc. 29th Linear Accelerator Conf. (LINAC'18)*, Beijing, China, Sep. 2018, pp. 74–77.

[65] B. Walasek-Hoehne, K. Hoehne and R. Singh, Proceedings of the 2018 CERN–Accelerator–School course on Beam Instrumentation, Tuusula, (Finland), pp. 11–16, arXiv:2005.04977 [physics.acc-ph].

[66] L. Shenggang, *et al.*, "Surface polariton Cherenkov light radiation source," *Phys. Rev. Lett.*, vol. 109, p. 153902, Oct 2012.

[67] N. Mounet, "IW2D User Manual", CERN Manual, Apr. 2016. `https://gitlab.cern.ch/IRIS/IW2D`,.

[68] K. Lasocha, D. M. Harryman, T. Lefèvre, N. Mounet, and A. Schloegelhofer, "Simulation of Cherenkov Diffraction Radiation for Various Radiator Designs", in *Proc. IBIC'20*, Santos, Brazil, Sep. 2020, pp. 73–77. `doi:10.18429/JACoW-IBIC2020-TUPP28`.

[69] Dassault Systèmes, "CST Studio Suite Electromagnetic field simulation software", Accessed on Aug, 6, 2020. [Online]. Available: `https://www.3ds.com/products-services/simulia/products/cst-studio-suite/`.

[70] H. R. Phillip, and E. A. Taft, "Kramers-kronig analysis of reflectance data for diamond," *Phys. Rev.*, vol. 136, pp. A1445–A1448, Nov 1964.

[71] B. Walasek-Höhne, Proceedings of the 2018 CERN–Accelerator–School course on Beam Instrumentation, Tuusula, (Finland), pp. 3–7, arXiv:2005.04977 [physics.acc-ph].

[72] G. Lehmann, "Kappa Sigma Clipping," *The Insight Journal*, 11 2006.

[73] S. Dewangan, and A. K. Sharma, "Image smoothening and sharpening using frequency domain filtering technique," *International Journal of Emerging Technologies in Engineering Research*, vol. 5, pp. 169–174, 04 2017.

[74] T. Carvalho, F. Krammer, and A. Iwasaki, "The first 12 months of COVID-19: a timeline of immunological insights". Nat Rev Immunol 21, 245–256, (2021). `https://doi.org/10.1038/s41577-021-00522-1`.

[75] Hamamatsu, “Photosensor Modules H15460-40 Series”, datasheet, TPMO1096E02, pp. 1–4, 911.

[76] E. Senes, *et al.*, “Beam Position Detection of a Short Electron Bunch in Presence of a Longer and More Intense Proton Bunch for the AWAKE Experiment”, presented at the IBIC’21, Pohang, Korea, Sep. 2021, paper MOPP17, unpublished.